High-Performance Wireless Interface for Implant-to-Air Communications

Thèse

Hadi Bahramiabrghouei

Doctorat en génie électrique
Philosophiæ doctor (Ph.D.)

Québec, Canada

Résumé

Nous élaborons une interface cerveau-machine (ICM) entièrement sans fil afin de fournir un système de liaison directe entre le cerveau et les périphériques externes, permettant l'enregistrement et la stimulation du cerveau pour une utilisation permanente. Au cours de cette thèse, nous explorons la modélisation de canal, les antennes implantées et portables en tant que propagateurs appropriés pour cette application, la conception du nouveau système d'un émetteur-récepteur UWB implantable, la conception niveau système du circuit et sa mise en œuvre par un procédé CMOS TSMC 0.18 μm. En plus, en collaboration avec Université McGill, nous avons conçu un réseau de seize antennes pour une détection du cancer du sein à l'aide d'hyperfréquences.

Notre première contribution calcule la caractérisation de canal de liaison sans fil UWB d'implant à l'air, l'absorption spécifique moyennée (ASAR), et les lignes directrices de la FCC sur la densité spectrale de puissance UWB transmis. La connaissance du comportement du canal est nécessaire pour déterminer la puissance maximale permise à 1) respecter les lignes directrices ANSI pour éviter des dommages aux tissus et 2) respecter les lignes directrices de la FCC sur les transmissions non autorisées. Nous avons recours à un modèle réaliste du canal biologique afin de concevoir les antennes pour l'émetteur implanté et le récepteur externe. Le placement des antennes est examiné avec deux scénarios contrastés ayant des contraintés de puissance. La performance du système au sein des tissus biologiques est examinée par l'intermédiaire des simulations et des expériences.

Notre deuxième contribution est dédiée à la conception des antennes simples et à double polarisation pour les systèmes d'enregistrement neural sans fil à bande ultra-large en utilisant un modèle multicouches inhomogène de la tête humaine. Les antennes fabriquées à partir de matériaux flexibles sont plus facilement adaptées à l'implantation ; nous étudions des matériaux à la fois flexibles et rigides et examinons des compromis de performance. Les antennes proposées sont conçues pour fonctionner dans une plage de fréquence de 2-11 GHz (ayant S11-dessous de -10 dB) couvrant à la fois la bande 2.45 GHz (ISM) et la bande UWB 3.1-10.6 GHz. Des mesures confirment les résultats de simulation et montrent que les antennes flexibles ont peu de dégradation des performances en raison des effets de flexion (en termes de correspondance d'impédance). Finalement, une comparaison est réalisée entre quatre antennes implantables, couvrant la gamme 2-11 GHz : 1) une rigide, à la polarisation simple, 2) une

rigide, à double polarisation, 3) une flexible, à simple polarisation et 4) une flexible, à double polarisation. Dans tous les cas une antenne rigide est utilisée à l'extérieur du corps, avec une polarisation appropriée. Plusieurs avantages ont été confirmés pour les antennes à la polarisation double : 1) une taille plus petite, 2) la sensibilité plus faible aux désalignements angulaires, et 3) une plus grande fidélité.

Notre troisième contribution fournit la conception niveau système de l'architecture de communication sans fil pour les systèmes implantés qui stimulent simultanément les neurones et enregistrent les réponses de neurones. Cette architecture prend en charge un grand nombre d'électrodes (> 500), fournissant 100 Mb/s pour des signaux de stimulation de liaison descendante, et Gb/s pour les enregistrements de neurones de liaison montante. Nous proposons une architecture d'émetteur-récepteur qui partage une antenne ultra large bande, un émetteur-récepteur simplifié, travaillant en duplex intégral sur les deux bandes, et un nouveau formeur d'impulsions pour la liaison montante du Gb/s soutenant plusieurs formats de modulation. Nous présentons une démonstration expérimentale d'ex vivo de l'architecture en utilisant des composants discrets pour la réalisation les taux Gb/s en liaison montante. Une bonne performance de taux d'erreur de bit sur un canal biologique à 0,5, 1 et 2 Gb/s des débits de données pour la télémétrie de liaison montante (UWB) et 100 Mb/s pour la télémétrie en liaison descendante (bande 2.45 GHz) est atteinte.

Notre quatrième contribution présente la conception au niveau du circuit d'un dispositif d'émission en duplex total qui est présentée dans notre troisième contribution. Ce dispositif d'émission en duplex total soutient les applications d'interfaçage neural multimodal et en haute densité (les canaux de stimulant et d'enregistrement) avec des débits de données asymétriques. L'émetteur (TX) et le récepteur (RX) partagent une seule antenne pour réduire la taille de l'implant. Le TX utilise impulse radio ultra-wide band (IR-UWB) basé sur une approche alliant des bords, et le RX utilise un nouveau 2.4 GHz récepteur on-off keying (OOK).Une bonne isolation (> 20 dB) entre le trajet TX et RX est mis en œuvre 1) par mise en forme des impulsions transmises pour tomber dans le spectre UWB non réglementé (3.1-7 GHz), et 2) par un filtrage espace-efficace du spectre de liaison descendante OOK dans un amplificateur à faible bruit RX. L'émetteur UWB 3.1-7 GHz peut utiliser soit OOK soit la modulation numérique binaire à déplacement de phase (BPSK). Le FDT proposé offre une double bande avec un taux de données de liaison montante de 500 Mbps TX et un taux de données de liaison descendante de 100 Mb/s RX, et il est entièrement en conformité avec les standards TSMC 0.18 μm CMOS dans un volume total de 0,8 mm^2. Ainsi, la mesure de consommation d'énergie totale en mode full duplex est de 10,4 mW (5 mW à 100 Mb/s pour RX, et de 5,4 mW à 500 Mb/s ou 10,8 PJ / bits pour TX).

Notre cinquième contribution est une collaboration avec l'Université McGill dans laquelle nous concevons des antennes simples et à double polarisation pour les systèmes de détection du cancer du sein à l'aide d'hyperfréquences sans fil en utilisant un modèle multi-couche et

inhomogène du sein humain. Les antennes fabriquées à partir de matériaux flexibles sont plus facilement adaptées à des applications portables. Les antennes flexibles miniaturisées monopôles et spirales sur un 50 μm Kapton polyimide sont conçus, en utilisant high frequency structure simulator (HFSS), à être en contact avec des tissus biologiques du sein. Les antennes proposées sont conçues pour fonctionner dans une gamme de fréquences de 2 à 4 GHz. Les mesures montrent que les antennes flexibles ont une bonne adaptation d'impédance dans les différentes positions sur le sein. De Plus, deux antennes à bande ultralarge flexibles 4×4 (simple et à double polarisation), dans un format similaire à celui d'un soutien-gorge, ont été développés pour un système de détection du cancer du sein basé sur le radar.

Abstract

We are working on a fully wireless brain-machine-interface to provide a communication link between the brain and external devices, enabling recording and stimulating the brain for permanent usage. In this thesis we explore channel modeling, implanted and wearable antennas as suitable propagators for this application, system level design of an implantable UWB transceiver, and circuit level design and implementing it by TSMC 0.18 μm CMOS process. Also, in a collaboration project with McGill University, we designed a flexible sixteen antenna array for microwave breast cancer detection.

Our first contribution calculates channel characteristics of implant-to-air UWB wireless link, average specific absorption rate (ASAR), and FCC guidelines on transmitted UWB power spectral density. Knowledge of channel behavior is required to determine the maximum allowable power to 1) respect ANSI guidelines for avoiding tissue damage and 2) respect FCC guidelines on unlicensed transmissions. We utilize a realistic model of the biological channel to inform the design of antennas for the implanted transmitter and the external receiver. Antennas placement is examined under two scenarios having contrasting power constraints. Performance of the system within the biological tissues is examined via simulations and experiments.

Our second contribution deals with designing single and dual-polarization antennas for wireless ultra-wideband neural recording systems using an inhomogeneous multi-layer model of the human head. Antennas made from flexible materials are more easily adapted to implantation; we investigate both flexible and rigid materials and examine performance trade-offs. The proposed antennas are designed to operate in a frequency range of 2–11 GHz (having S_{11} below -10 dB) covering both the 2.45 GHz (ISM) band and the 3.1–10.6 GHz UWB band. Measurements confirm simulation results showing flexible antennas have little performance degradation due to bending effects (in terms of impedance matching). Finally, a comparison is made of four implantable antennas covering the 2-11 GHz range: 1) rigid, single polarization, 2) rigid, dual polarization, 3) flexible, single polarization and 4) flexible, dual polarization. In all cases a rigid antenna is used outside the body, with an appropriate polarization. Several advantages were confirmed for dual polarization antennas: 1) smaller size, 2) lower sensitivity to angular misalignments, and 3) higher fidelity.

Our third contribution provides system level design of wireless communication architecture for implanted systems that simultaneously stimulate neurons and record neural responses. This architecture supports large numbers of electrodes (>500), providing 100 Mb/s for the downlink of stimulation signals, and Gb/s for the uplink neural recordings. We propose a transceiver architecture that shares one ultra-wideband antenna, a streamlined transceiver working at full-duplex on both bands, and a novel pulse shaper for the Gb/s uplink supporting several modulation formats. We present an ex-vivo experimental demonstration of the architecture using discrete components achieving Gb/s uplink rates. Good bit error rate performance over a biological channel at 0.5, 1, and 2 Gbps data rates for uplink telemetry (UWB) and 100 Mbps for downlink telemetry (2.45 GHz band) is achieved.

Our fourth contribution presents circuit level design of the novel full-duplex transceiver (FDT) which is presented in our third contribution. This full-duplex transceiver supports high-density and multimodal neural interfacing applications (high-channel count stimulating and recording) with asymmetric data rates. The transmitter (TX) and receiver (RX) share a single antenna to reduce implant size. The TX uses impulse radio ultra-wide band (IR-UWB) based on an edge combining approach, and the RX uses a novel 2.4-GHz on-off keying (OOK) receiver. Proper isolation (>20 dB) between the TX and RX path is implemented 1) by shaping the transmitted pulses to fall within the unregulated UWB spectrum (3.1-7 GHz), and 2) by space-efficient filtering (avoiding a circulator or diplexer) of the downlink OOK spectrum in the RX low-noise amplifier. The UWB 3.1-7 GHz transmitter can use either OOK or binary phase shift keying (BPSK) modulation schemes. The proposed FDT provides dual band 500-Mbps TX uplink data rate and 100 Mbps RX downlink data rate, and it is fully integrated into standard TSMC 0.18 μm CMOS within a total size of 0.8 mm^2. The total measured power consumption is 10.4 mW in full duplex mode (5 mW at 100 Mbps for RX, and 5.4 mW at 500 Mbps or 10.8 pJ/bit for TX).

Our fifth contribution is a collaboration project with McGill University which we design single and dual-polarization antennas for wireless ultra-wideband breast cancer detection systems using an inhomogeneous multi-layer model of the human breast. Antennas made from flexible materials are more easily adapted to wearable applications. Miniaturized flexible monopole and spiral antennas on a 50 μm Kapton polyimide are designed, using a high frequency structure simulator (HFSS), to be in contact with biological breast tissues. The proposed antennas are designed to operate in a frequency range of 2–4 GHz (with reflection coefficient (S_{11}) below -10 dB). Measurements show that the flexible antennas have good impedance matching while in different positions with different curvature around the breast. Furthermore, two flexible conformal 4×4 ultra-wideband antenna arrays (single and dual polarization), in a format similar to that of a bra, were developed for a radar-based breast cancer detection system.

Contents

List of Tables

List of Figures

Abbreviations

AWG	Arbitrary Wave Generator
ANSI	American National Standards Institute
ASAR	Average Specific Absorption Rate
ASK	Amplitude Shift Keying
BMI	Brain Machine Interface
BER	Bit Error Rate
BPSK	Binary Phase Shift Keying
CMOS	Complementary Metal Oxide Semiconductor
CS	Common Source
CSF	Cerebrospinal Fluid
CPW	Coplanar Waveguide
DPSK	Differential Phase Shift Keying
EM	Electro-Magnetic
FCC	Federal Communications Commission
FSK	Frequency Shift Keying
FDT	Full-Duplex Transceiver
FoM	Figure of Merit
HFSS	High Frequency Structure Simulator
ISM	Industrial, Scientific and Medical
IR-UWB	Impulse Radio Ultra-Wide Band
ISI	Inter-Symbol Interference
LO	Local Oscillator
LNA	Low Noise Amplifier
MI	Microwave Imaging
MT	Microwave Tomography
MB-OFDM	Multi-Band Orthogonal Frequency-Division Multiplexing
MPPM	Multiple Pulse Position Modulation
NF	Noise Figure
OOK	On-Off Keying

PSK	Phase Shift Keying
PRBS	Pseudo-Random Binary Sequence
PCB	Printed Circuit Board
RX	Receiver
SNR	Signal-to-Noise Ratio
SMA	Sub-Miniature version A
TSMC	Taiwan Semiconductor Manufacturing Company
TX	Transmitter
VLSI	Very-Large-Scale Integration

List of Symbols

λ	Wavelength
θ_1	Half-Power Beam-Width of Radiation Pattern in Horizontal
θ_2	Half-Power Beam-Width of Radiation Pattern in Vertical
D_0	Directivity Peak at Broadside
G_t	Maximum Gain
P_t	Maximum Transmitted Power
$\tau(\omega)$	Group Delay
D	Biggest Dimension of the Effective Antenna
$A(\omega)$	Amplitude of Frequency Response
$\theta(\omega)$	Phase of Frequency Response
$H(\omega)$	Frequency Response
F	Fidelity
$S_r(t)$	Actual Received Waveform from One Pair Antenna
$r(t)$	Received Pulse from an Ideal Wireless Link
t_0	Offset Time Domain of Gaussian Pulse
τ	Standard Deviation of Gaussian Distribution
f_0	Center Frequency of Gaussian-Modulated Sinusoidal Waveform
$V(t)$	Gaussian-Modulated Sinusoidal Waveform
E_y	E field in y Direction
E_x	E field in x Direction
Ω	Ohm
J	Joule (Unit of Energy)
W	Watt (Unit of Power)
W_{av}	Time Average Poynting Vector
S_{21}	Reflection Coefficient
S_{11}	Transmission Coefficient

To my family

Acknowledgement

First and foremost, I would like to thank Prof. Leslie Ann Rusch for guiding my research, allowing me to discover several topics, and providing me the resources to carry it out. She encouraged me to perform to the best of my abilities and gave me opportunities to learn different topics. I would never have had these opportunities if I had not joined her group. I will never forget her lessons and all that she did for me. I would also like to thank Prof. Benoit Gosselin for his advice and guidance. I had this opportunity to work closely with him on his brain machine interface project.

I also thank the members of my reading and oral committee, for their comments and thoughts on this thesis. They have all demonstrated an outstanding passion for their work, which translates into great understanding of their respective fields that easily comes across during my conversations with them.

I am also grateful to Prof. Dominic Grenier for letting us to use his lab and measurement equipment. I am also deeply thankful for Prof. Paul Fortier and Prof. Milica Popovich for their guidance and advice. I would also like to thank my team members Seyed Abdullah Mirbozorgi, Emily Porter, and Reza Ameli for their corporation, help and support through the research. I am greatly indebted to Dr. Nguyen, Mr. Chretien and Mr. Gagnon for their assistance and corporation.

Finally, I am deeply grateful to my parents and my family for their endless encouragement. This work could not have been accomplished without their dedicated support, trust, and love throughout my life.

Foreword

Five chapters of this thesis are composed of material already published in technical Transactions. In the thesis, text have been modified to be consistent with the rest of the document. The introduction sections have been most heavily modified. Here, I detail my contributions to five published papers.

Paper 1: H. Bahrami, S. A. Mirbozorgi, L. A. Rusch, and B. Gosselin, "Biological Channel Modeling and Implantable UWB Antenna Design for Neural Recording Systems," IEEE Transactions on Biomedical Engineering, (Accepted, 2014). This transaction paper is devoted to study of the biological channel modeling and TX and RX ultra-wideband (UWB) antenna design for neural recording systems. The original idea is proposed by myself, the experiments were conducted at LRTS lab at Laval University and Ecole Polytechnique de Montreal. I was assisted in the experiments by Seyed Abdollah Mirbozorgi, a PhD student within our group. The simulations were done by me. The manuscript was prepared by me and revised by the other authors before submission.

Paper 2: H. Bahrami, S. A. Mirbozorgi, R. Ameli, L. A. Rusch, and B. Gosselin, "Flexible UWB Antennas with Polarization-Diverse Implantable for Neural Recording Systems," IEEE Transactions on Biomedical Circuits and Systems, (Accepted, 2015). This paper deals with designing of implanted flexible UWB antennas with polarization-diverse for neural recording systems. The idea in this paper was proposed by myself, the experiments were conducted at LRTS labs at Laval University. I was assisted in the experiments by Seyed Abdollah Mirbozorgi and Reza Ameli, a PhD and a master students, respectively, within our group. The simulations were done by me. The manuscript was prepared by me and revised by the other authors before submission.

Paper 3: H. Bahrami, S. A. Mirbozorgi, T. A. Nguyen, B. Gosselin, and L. A. Rusch, "A Novel High-Speed Full-Duplex Transceiver for Neural Recording and Stimulating Systems," IEEE Transactions on Microwave Theory and Techniques, (Under review, 2015). This transaction paper explores a novel high-speed full-duplex transceiver for neural recording and stimulating systems that I proposed. I performed the simulations. The experiment was done by me and Seyed Abdollah Mirbozorgi with valuable help of Dr. Truong An Nguyen at Prof. Rusch's lab in Center for Optics, Photonics and Lasers (COPL) at Laval University. I prepared the

manuscript with the help of Seyed Abdullah Mirbozorgi and all the authors revised it before submission.

Paper 4: S. A. Mirbozorgi, H. Bahrami, M. Sawan, L. A. Rusch, and B. Gosselin, "Fully Integrated Circulator-less Full Duplex Transceiver Circuit Design for Bio-Implant Applications," IEEE Transactions on Biomedical Circuits and Systems, (Under review, 2014). The suggested system level mentioned in third paper is deigned and implemented in this paper. In this work on the transceiver, the transmitter part was my work and the receiver part was designed by Seyed Abdollah Mirbozorgi. During the design of the receiver, I helped my colleague in designing inductors with HFSS. The experiment was done by Seyed Abdullah Mirbozorgi and me at Prof. Rusch's lab in Center for Optics, Photonics and Lasers (COPL) at Laval University. Seyed Abdullah Mirbozorgi prepared the manuscript with my help and all the authors revised it before submission.

Paper 5: H. Bahrami, E. Porter, A. Santorelli, B. Gosselin, M. Popovic, and L. A. Rusch, "Flexible Sixteen Antenna Array for Microwave Breast Cancer Detection," IEEE Transactions on Biomedical Engineering, (Under review, 2014). This journal paper explores a flexible sixteen antenna array for microwave breast cancer detection in a collaboration project with McGill University. The idea in this paper is proposed by myself and I performed the simulations. The experiment was done by me and Emily Porter at LRTS lab and Prof. Popovic's lab at Laval University and McGill University, respectively. I prepared the manuscript and all the authors revised it before submission.

Chapter 1

Introduction

With recent advances in the field of microelectronics, there has been a concerted effort towards using miniature electronics to cure nervous system impairments. Miniature implantable devices, as an integral part of biomedical brain-machine-interfaces, have received particular attention as they provide the neuroscientists with insight into the inner working of the nervous system. This insight results in diagnosis and treatment of many neurological disorders, as well as enabling the disabled (for example the paraplegic) to use advanced brain-controlled prosthetic limbs [2,3].

Designing modern miniature implanted biomedical devices is always challenging as many restrictions apply; these restrictions include but are not limited to 1) low power consumption, 2) small form factor, 3) biocompatibility, and 4) wireless capabilities for power delivery and data transmission. All the mentioned design requirements result in a challenging and complicated design process where care must be taken to respect all criteria early in the design [2].

The untethered nature of the biomedical implantable devices forces the entire system to operate on a very limited power budget. Moreover, the implanted devices must not consume too much power even when a high-capacity power source is available, as the dissipated heat might damage the surrounding tissues. As a consequence, low power operation is inevitable.

In addition, the space inside the brain, that hosts the implantable device, is very small and limited. As a result, it will be necessary to integrate in Very-large-scale integration (VLSI) as many parts as possible on a (single) small chip die to miniaturize the system. Nonetheless, as the number of neural stimulation/recording channels increases, the size and power consumption of the system increases too, resulting in contradicting design requirements.

The implantable system must be isolated from the surrounding environment using biocompatible material to prevent infection in long-term (perhaps permanent) usage. In addition, the need for wireless connectivity is another challenging requirement. Wires always expose the test subject to infection risks and hinder its movement. As a result, long-term experiments,

especially on freely-moving animals, require wireless systems.

As shown in Fig. 1.1, the applications we target in this thesis require a wireless connection to establish a communication link between an implanted device and an external controller. Power and data should be transmitted to the implanted system, which is inside the body of the animals or patients. The neural data should be transmitted outside the body for analysis. A higher number of recording and stimulation channels results in greater flexibility in the brain-computer interface. A high number of neural recording channels results in high bandwidth requirements. Another issue is proper implantable and wearable antennas for these applications. In order to address the problem of implantable high-speed communications, the following techniques have been used: 1) use of ultra-wideband (UWB) communications and 2) designing custom implantable and wearable UWB antennas by considering the inhomogeneous biological environment (body tissues) surrounding the antennas.

Ultra-Wideband radio is a wireless communication system where signals are transmitted in the frequency range of 3.1 to 10.6 GHz. UWB offers several advantages over narrowband systems (such as the Medical Implant Communications Service) as it supports higher bit rates and can be efficiently implemented in highly integrated systems. Also, UWB requires smaller antennas than the conventional narrowband systems, due to its wide bandwidth and higher frequency [2, 3].

The simple structure of a UWB transmitter leads to lower power consumption, smaller size, and lower implementation costs in standard integrated circuit technologies such as complementary metal–oxide–semiconductor (CMOS). The mentioned advantages provide a myriad of opportunities, but also comes with many challenges in RF circuit and antenna design.

Wireless implantable devices require carefully-designed antennas as an antenna surrounded by biological tissues will have very different propagation behaviour compared to an antenna in free space. Before designing an implantable or wearable antenna for biomedical applications, the effect of biological tissues on RF signals must be investigated. This problem has been addressed by creating an electromagnetic model of the human head and designing the antennas accordingly. This modeling approach allows us to explore antenna design for the breast cancer detection solutions using microwave imaging (MI) by modeling the human breast in a separate study.

This thesis focuses on system and circuit level design of a low-power high-bandwidth wireless implantable transceiver, as well as the related wireless channel modeling and antenna design. In this chapter we will introduce the human head and breast modeling in EM software which is very important in designing implantable and wearable antennas. We will explain the modeling of inhomogeneous behavior of biological tissues environment which makes EM propagation waves more challenging.

Next we introduce different types of compact antennas which are appropriate as implantable and wearable antennas. We give a brief overview of system level design flow for a wireless communication link. Finally, we describe the organization of the remaining chapters of this thesis.

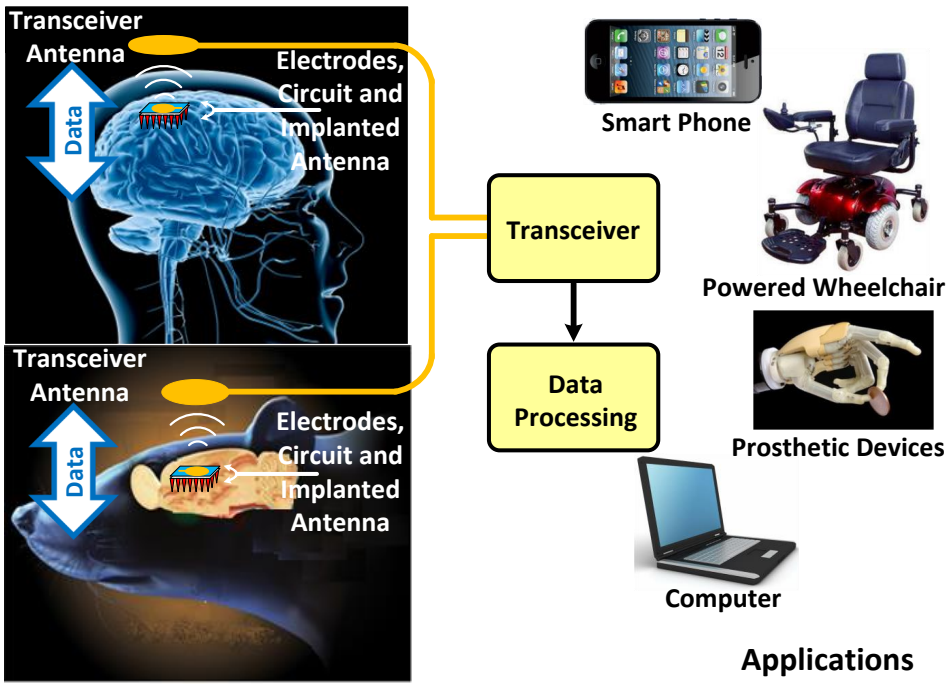

Figure 1.1: An overview of an implanted neural recording and stimulating system and its applications.

1.1 Multi-layer Model of Biological Tissues in EM Software

Unlike free space communications, multiple biological tissues have varying conductivity and dielectric constants leading to complex RF interaction. The thickness and electrical properties of each tissue layer impact the overall antenna performance [4,5]. In the following sections we discuss our methodology in modeling a human head and a breast, which are used in designing the antennas in chapter 2, 3, 6.

1.1.1 Human Head

The head as an EM wave propagation media is modeled by several layers of biological tissues, where each biological tissue is defined as a dispersive dielectric material using three electrical parameters: relative permittivity, loss tangent and mass density. The stacked layers form an inhomogeneous media [6,7] which is simulated in high frequency structure simulator (HFSS).

The multi-layer model consists of brain matter, cerebro spinal fluid (CSF), dura, bone (skull), fat, and skin as shown in Fig. 1.2. The antennas (TX and RX) are designed taking into account the impact of surrounding tissues. Figure 1.3a and 1.3b show the frequency-dependent results for permittivity and the attenuation of different tissues in the parietal lobe region of the human head [1]. Mass density (mass of each tissue per unit volume) is another important parameter for frequency independent tissue. We used the mass density values to calculate the averaged specific absorption rate (ASAR). We used these electrical parameters to define each layer as a specific dielectric material in a multi-layer model implemented in the HFSS.

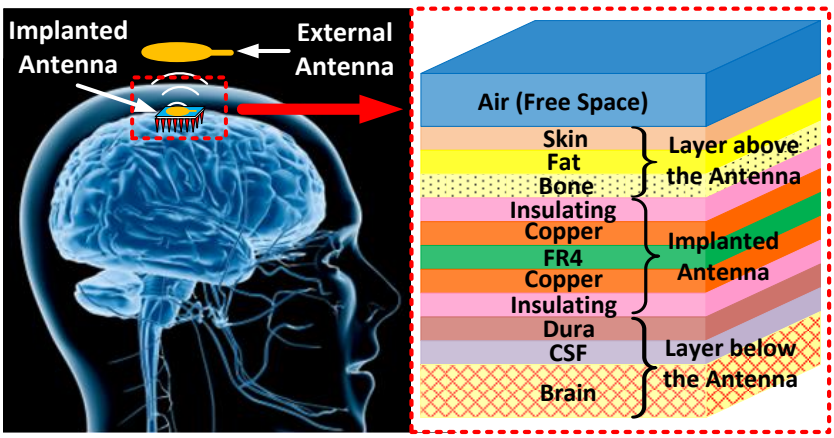

Figure 1.2: Human head model in HFSS software.

1.1.2 Breast

The multiple biological tissues in the breast have varying conductivity and dielectric constants [8]. The breast is modeled by several biological tissues as we did for the human head. By stacking several homogeneous layers, the inhomogeneous environment is modeled with the HFSS software [7]. The multi-layer model that is used to design a wearable antenna for breast

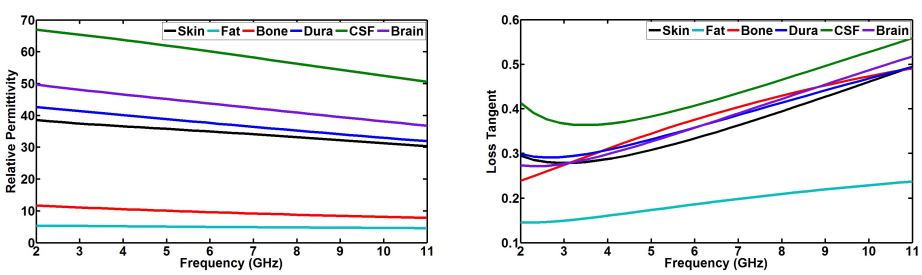

(a) (b)

Figure 1.3: (a) Relative permittivity ε_r of different tissues in the human head, (b) Loss tangent of different tissues in the human head [1].

cancer detection applications includes skin, fat, gland, and muscle, and is shown in Fig. 1.4 [8]. The frequency dependent relative permittivity and loss tangent are presented in [1] for the entire 2-4 GHz band as shown in Fig. 1.5. The mass density, i.e., the mass of each tissue per volume unit, is reported in [8] for different breast tissues.

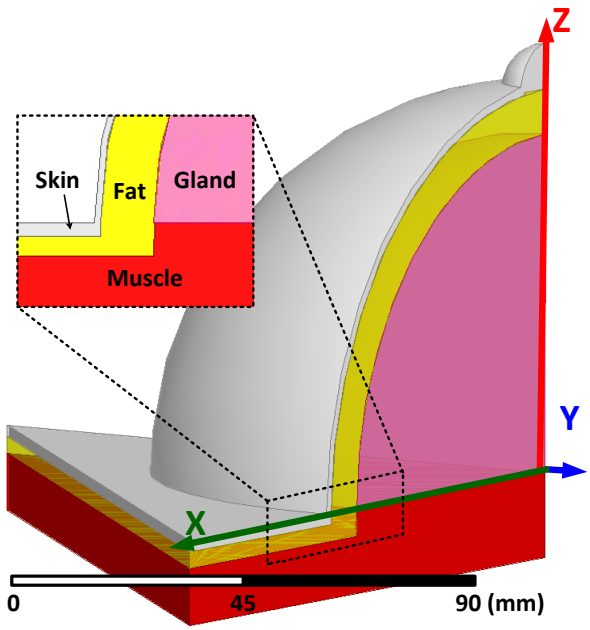

Figure 1.4: Human breast model in HFSS software.

1.2 Classification of Implantable and Wearable Antenna

The implantable UWB antenna is subject to specific requirements that render its design difficult: 1) it is restricted to small dimensions, and 2) it must be bio-compatible [4–6]. Antenna size should be on the order of that of the implantable chip [3].

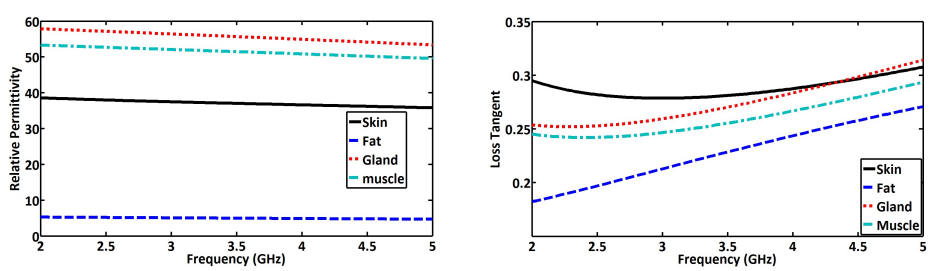

(a) (b)

Figure 1.5: (a) Relative permittivity ε_r of different tissues in the human breast, (b) Loss tangent of different tissues in the human breast [1].

There are several types of antennas which are suitable as implantable or wearable antennas because of their compact size. For designing the antennas, we use a printed circuit board (PCB) due to its small size and planar structure. Four popular categories of candidate antennas are presented in the following sections [9]

1.2.1 Dipole Antenna

A dipole antenna is a very commonly used antenna when space constraints are not strict. It consists of two elements facing away from each other. Generally, the length of each element is $\lambda/4$ where λ is the wavelength of the transmitting wave. The total length of the antenna is $\lambda/2$. Usually, the antenna elements are straight as shown in Fig. 1.6, but in some cases, the elements can be bent to accommodate a confined area. The antenna is fed in the center by the signal. The dipole antenna has a single polarization structure [9].

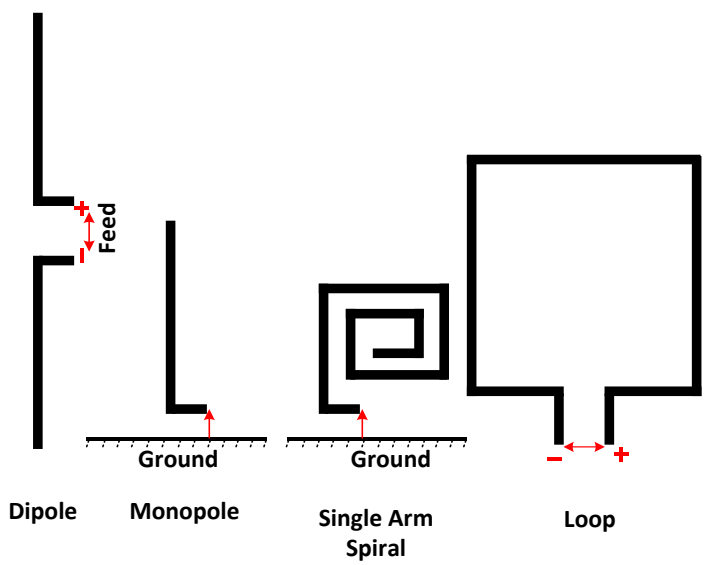

Figure 1.6: Different small antennas for implantable and wearable application

1.2.2 Monopole Antenna

A monopole antenna is the simplest practical antenna. Unlike the dipole, it consists of a single element mounted vertically on the ground plane. As shown in Fig. 1.6, the monopole antenna can be fed from the ground. Since a monopole consists of single element, the antenna length can be $\lambda/4$: half of that of a dipole. Thus the implementation area of a monopole is half of that of a dipole. But the performance of a monopole is inferior to that of a dipole. There is a trade-off between the length of the antenna and its performance. Monopole antennas have a single polarization structure [9].

1.2.3 Loop Antenna

A loop antenna consists of a single element rounded to form a loop. Unlike monopole or dipole antennas, the element in a loop antenna is shorted. Consequently, a loop antenna can be considered as a transmission line with short-circuited ends. When the total length of the loop is equal to the wavelength, the antenna radiates similarly to a monopole or a dipole. Since the perimeter of the loop antenna is equal to the wavelength, its element length is twice or four times that of a dipole or a monopole antenna, respectively. This means, the performance of a loop antenna is superior to that of a dipole or a monopole, at the cost of greater area. Loop antennas have a circular polarization structure [9].

1.2.4 Single Arm Spiral Antenna

A single arm spiral antenna is a bent monopole antenna. Its size is less than that of a monopole antenna and it can support dual polarization. A single arm spiral antenna is the best choice for implanted application in terms of compact size and angular misalignment, which will be discussed in chapter3 [9, 10].

1.2.5 Summary of Antennas

Having examined four candidate antennas, we seek the best trade-off for our application. Dual polarization will increase robustness of our system as it allows for diversity in the presence of misaligned TX and RX antennas. Both spiral and loop antennas support polarization diversity. However the spiral offers a clear advantage in size over the loop antenna. We therefore conclude that the singles spiral antenna is the best choice for implanted antennas in terms of compact size and robustness to angular misalignment (further discussed in Chapter 3).

1.3 System Level Design Flow

1.3.1 Selection of Operation Frequency Band

The transmitter and receiver designs, especially the front-end design, change according to the frequency band of operation. Issues like the path loss, required bit rate, power consumption, size of TX and RX circuits, and antenna design are all affected by the choice of frequency band [11].

Monitoring of neural responses with high resolution in the brain requires a high data rate link as the number of electrodes is increased. Ultra-wideband signals are transmitted in the unlicensed Federal Communications Commission (FCC) approved frequency range (3.1-10.6 GHz). UWB offers several advantages over narrow-band systems such as higher bit rates and highly integrated systems featuring smaller antenna size. The simple structure of a UWB

transmitter leads to low power consumption. The disadvantage of using the UWB band as opposed to a lower frequency band is higher loss [2,3].

1.3.2 Consideration of Propagation Channel Model

In our project, the propagation channel model must include several tissues and two antennas (one implanted and one wearable antenna), as they are in very close proximity (in the near field relative to one another). The close proximity of transmitter and receiver antennas makes it impossible to treat transmission loss as independent of the antenna design (as is typically the case). The channel cannot be investigated separately from the antennas, but encompasses transmitter and receiver antennas and all adjacent tissues. S_{21} is the electromagnetic wave coupling coefficient between the transmitter and receiver antennas, and it is the frequency response for this near field communications system. This parameter can be calculated by simulation or can be measured experimentally.

1.3.3 Link Budget Estimation

The link budget analysis helps to determine the feasibility of the communication system. A link budget calculation is also an excellent means to understand the various factors which must be traded off to realize a given cost and level of reliability for a communication link.

Link budget estimation is the summation of gain and loss in the transmitter and receiver system. From the link budget, we can find the receiver sensitivity and minimal signal to noise ratio SNR needed for an acceptable bit error rate (BER) performance. The link budget involves rough estimation of the following factors [11]:

- Receiver noise level

  This parameter quantifies the extent to which the received signal is corrupted with noise. This parameter can be measured by a spectrum analyzer or a real time oscilloscope.

- Received signal power

  This captures system losses for a reference transmission power, and can be measured by a spectrum analyzer or a real time oscilloscope.

- Receiver sensitivity

  BER performance varies with modulation and demodulation schemes. We investigate both coherent and non-coherent detection, and determine the minimum receiver sensitivity required for acceptable BER performance for each method.

- Link margin

  This parameterizes system robustness to unanticipated impairments.

The receiver sensitivity is calculated by the following equation

$$RXSensitivity(dBm) + LinkMargin(dB) = TXPower(dBm) + PathLoss(dB) \quad (1.1)$$

1.3.4 Modulation and Demodulation Scheme Design

Complexity and power consumption can be traded-off when choosing between coherent and incoherent architectures. Coherent detection requires more complex circuitry which results in higher power consumption; incoherent detection is less complex, which results in lower power consumption, but worse BER performance. In this thesis we work with On-off keying (OOK), differential phase shift keying (DPSK), and binary phase shift keying (BPSK) modulations. The primary purpose of this is optimization of the transmitted pulse and investigation of BER performance of BPSK (coherent), DPSK (incoherent) and OOK (incoherent) modulations [11].

1.3.5 Circuit Level Design

Although circuit level design forms the last step in the design flow, it is one of the most important tasks in the realization of a communication system. The architectures are different for different modulation schemes, however some components are common in most architectures. Components such as a pulse generator at the transmitter, and receiver front-end parts such as LNA and mixer are common to any architecture and play a crucial role in overall performance. In this thesis we investigate circuit level design of the transmitter for BPSK and OOK and an OOK receiver. Details are provided in Chapter 5.

1.4 Thesis Outline

In the previous sections of this chapter we presented the motivation for studying wireless UWB implant-to-air communication systems for neural stimulating and recording applications. We focus on designing of implantable and wearable antennas. To design the antennas, we need to model the biological tissues in EM software like HFSS. These techniques are applicable to antennas for detection of breast tumors, and is a spin-off of our main research line. We also reviewed the critical parameters of system level design flow, which will be addressed in this thesis.

In the following chapters, we present 1) the methodology of designing of implantable and wearable antennas, 2) realistic channel modeling for wireless implant-to-air data communications, and 3) novel system level design for neural stimulating and recording systems.

Chapter 2 is devoted to realistic channel modeling for implant-to-air data communications. Our contributions are the following:

- UWB transmitter antenna design for two locations of the implant.

- Designing an UWB external receiver antenna.
- Calculating the maximum allowable transmitted power to respect ANSI and FCC rules.
- Calculating worst case receiver sensitivities.

In Chapter 3 we introduce a methodology for designing single- and dual-polarization antennas on both rigid and flexible substrates for near-field communications of neural systems operating over two frequency bands (ISM and UWB). Our contributions are:

- A methodology for designing flexible single- and dual-polarization antennas.
- Definition of a figure of merit for near-field communications of neural systems.
- Comparison of single- and dual-polarization antennas for this application.

In Chapter 4 a novel full-duplex data transceiver is proposed for neural stimulating and recording systems. The novel technique has better performance in terms of small size and very low-power consumption. We modified the traditional use of separate up-link and down-link subsystems, and propose a novel full-duplex data transceiver, with one dual band RF bidirectional data link. Our contributions are:

- Proposing a novel full-duplex data transceiver for neural systems.
- Experimental demonstration of achievable data rates of the proposed system.

Chapter 5 presents circuit level design and implementation of the UWB pulse shaper emulated in experiments in chapter 4. Our contribution is:

- Circuit level implementation of a power efficient UWB pulse shaper on CMOS technology.

Chapter 6 presents a methodology for designing a flexible antenna array for radar-based Microwave Imaging (MI) for breast cancer diagnosis. This chapter presents a flexible 4×4 monopole and single arm spiral UWB antenna array, in a format similar to that of a bra, operating in the 2-4 GHz spectrum that meets bandwidth requirements of breast-cancer microwave-imaging. Our contributions are:

- Design of flexible 4×4 monopole and spiral antenna arrays on a 50 μm Kapton polyimide.
- Improved penetration of the propagated EM waves from the antennas into the breast by using a reflector.

Finally, in Chapter 6, conclusions are drawn, and some of the possible future research plans, based on the material developed in this dissertation, are suggested.

Chapter 2

Biological Channel Modeling and Implantable UWB Antenna Design

Abstract

Results from this chapter were published in [J1]. Knowledge of channel behavior is required to determine the maximum allowable power to 1) respect ANSI guidelines for avoiding tissue damage and 2) respect FCC guidelines on unlicensed transmissions. We utilize a realistic model of the biological channel to inform the design of antennas for the implanted transmitter and the external receiver under these requirements. Antennas placement is examined under two scenarios having contrasting power constraints. Performance of the system within the biological tissues is examined via simulation and experiment. Our miniaturized antennas, 12 mm×12 mm, need worst case receiver sensitivities of -38 dBm and -30.5 dBm for the first and second scenarios, respectively. These sensitivities allow us to successfully detect signals transmitted through tissues in the 3.1-10.6 GHz UWB band.

2.1 Introduction

In this chapter the main contributions are:

- UWB transmitter antenna design for two locations of the implant.
- Designing an UWB external receiver antenna.
- Calculating the maximum allowable transmitted power to respect ANSI and FCC rules.
- Calculating worst case receiver sensitivities.

While UWB design for small size, low power consumption and high data rate has been widely examined, most antennas were designed for free space utilization [12, 13], not for use in human tissue. Wireless implantable UWB transmitters specifically designed for data acquisition

systems implanted into the human head for neural recording have been examined in [3,10,14], however channel characteristics, average specific absorption rate (ASAR) and FCC guidelines on transmitted UWB power spectral density were not taken into account. The transmission loss for the human head in the 100 MHz to 6 GHz band has been investigated in [15] for a mm-size antenna without considering of the bandwidth of TX and RX antennas or the effect of biological tissues on system performance.

An antenna surrounded by biological tissues in its near-field acts as a new effective antenna with new propagation behavior and return loss different from the actual antenna. As a result, an antenna designed for one part of the body (i.e., designed according to the dielectric properties of that part of the body) might not operate as expected in another part of the body. Planar microstrip UWB antennas, implanted in human tissues, have been designed and studied [5,16–20], however not for human head tissues. Many of the implanted antennas proposed in the literature are designed for gastro applications [18–20]. In these applications, the antenna is moving in the body and experiences an environment with changing dielectric properties, making the antenna optimization problematic. Furthermore, these antennas were for the most part designed for a single layer of homogenous material [19]. So antennas used for gastro applications will not necessarily work well when implanted in the brain. These papers [5, 16–20] focused on a methodology for designing a reliable wireless link for neural recording system using tissue modeling and designed antennas for this purpose. Head tissue is particularly sensitive, and ASAR requirements will tend to limit achievable data rate. By examining ASAR, we can accurately predict system performance (e.g., signal to noise ratio) for our antenna designs and target increased data rate.

In section 2.2, we present a model of biological tissues used for channel modeling, and discuss the implications of requiring a near-field analysis rather than far field for this application. In section 2.3 we consider TX antenna design for two scenarios for the location of the implant. We also design a receiver antenna to be external to the body (one receiver antenna design covers either location for the transmitter antenna). In section 2.4 we simulate the performance of antennas designed in section 2.3, as well as the overall channel characteristics for the wireless link. In section 2.5 we fabricate and characterize three antennas (scenario 1 transmitter antenna (TX1), scenario 2 transmitter antenna (TX2), and a receiver antenna applicable to either scenario (RX)). Characterization of the antenna with tissue present is accomplished by placing the antennas in fresh brain and bone tissues of a sheep, as well as fat and skin from a chicken. Measured results are in good agreement with simulation. In section 2.6, potential for high data rates is concluded for neural recording which is based on our results. Finally, conclusions are drawn in section 2.7.

Table 2.1: The best and worst cases of the parietal lobe region of the human head in mm.

Tissue	Min.	Max.
Skin	0.5	1.0
Fat	0	2.0
Bone	2.0	7.0
Dura	0.5	1.0
CSF	0.0	2.0
Brain	40.0	40.0

2.2 Channel Modeling Under Two Scenarios

A miniature antenna surrounded by biological tissues will have a very different radiation pattern than one in free-space; hence the gain and directivity of the antennas will be affected. As the impedance of the biological tissues is very different from that of free space, careful impedance matching is required; return loss must be calculated while considering the impact of biological tissues. Transmitting energy in body must always put patient health concerns first. We evaluate safety (avoidance of tissue damage) in terms of the 1-gram ASAR distribution guidelines set by American National Standards Institute (ANSI). Evaluation of signal impact on tissue is captured with our HFSS simulator. We present a design methodology that 1) respects ANSI limits on ASAR, 2) maximizes system performance, and 3) respects FCC regulations limiting transmission power to avoid interference with other devices.

2.2.1 Multi-layer Model of Tissues

We evaluate antenna performance for ASAR and for data transmission. Transmission is captured by H(ω), the frequency response of the neural monitoring channel

$$H(\omega) = A(\omega)e^{j\theta(\omega)} \tag{2.1}$$

where A(ω) and $\theta(\omega)$ are the amplitude and phase [11]. We use a multi-layer model of head tissue, as shown in Fig. 1.2, to find the frequency response and ASAR using HFSS, a commercial finite element method solver. The antennas (TX and RX) are designed taking into account the impact of surrounding tissues.

As we discussed in Chapter 1, the head as a communication channel is modeled by multi-layer of biological tissues including the brain matter, the cerebrospinal fluid (CSF), the dura, bone (skull), fat, and skin.

The thickness of each layer will affect its impact on the channel; hence we consider two extreme cases, minimum and maximal adult tissue thicknesses that are indicated in Table 2.1. The worst case (i.e., leading to greatest signal attenuation) occurs with the maximum thicknesses that can be encountered and are listed in the column labeled Max. Minimal values are listed

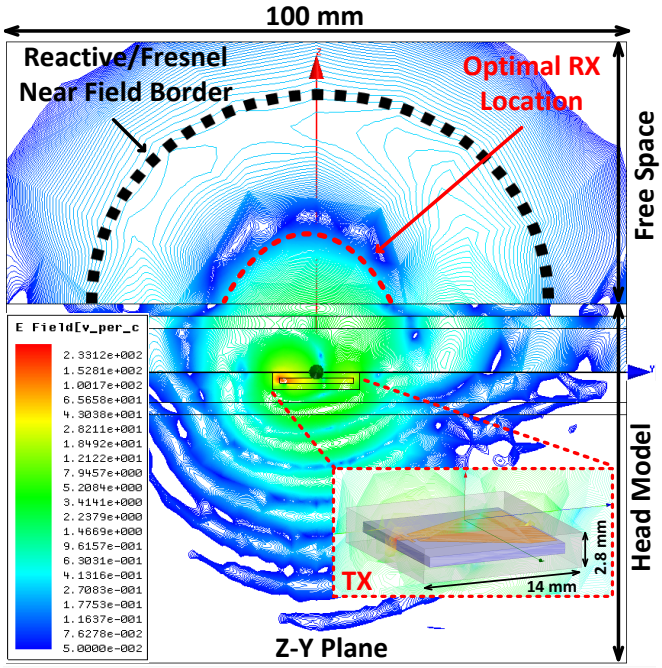

(a)

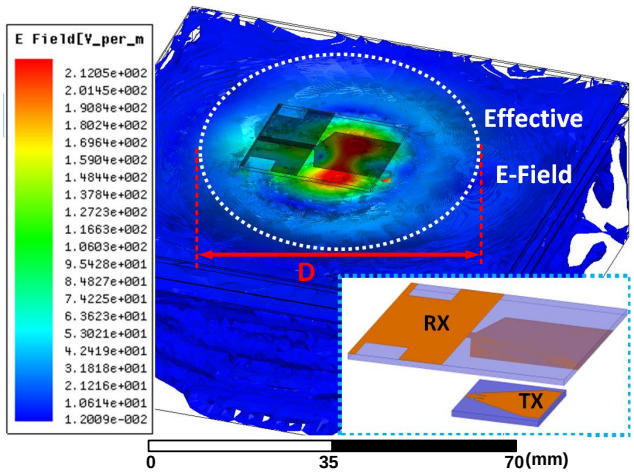

(b)

Figure 2.1: a) E-field intensity at 3 GHz in the multi-layer model, (b) E-field intensity beyond the Z-Y plane.

in the column Min. As the system must function for all cases encountered, we design the antennas for the worst case. We examine their performance for both best and worst case [21].

2.2.2 Near-field Behavior

HFSS provides a three dimensional numerical solution for the electrical field intensity across all tissues. A planar cross section (Z-Y plane) of the intensity is plotted in Fig. 2.1a; a color bar indicates that maximum intensity is in red, and minimal values in blue. The arrows on the far right indicate sections corresponding to tissues in the head, and the section for free space transmission outside the head. The presumed location of the TX antenna is recognizable as the position of maximum intensity (a fine box outlines antenna dimensions). This plot allows us to visualize three important aspects of the transmission: 1) the intensity in surrounding tissue that will be used in ASAR calculations, 2) the border between near and far field effects, and 3) the optimal location for the RX antenna outside the head. We discuss in this section the importance of near field effects.

The space surrounding an antenna is usually divided into three regions, 1) reactive near-field, 2) radiating near-field (Fresnel), and 3) far-field (Fraunhofer) [22]. In the Fresnel region, the angular distribution of the electrical intensity is directive, but it varies with distance, whereas in the far-field, the intensity distribution of the radiated field is relatively constant with distance. As shown in Fig. 2.1b most of the EM field is confined in the white dashed circle that has a diameter of D = 67 mm. To calculate the border between different radiation regions in free space, we consider this dimension D of the effective antenna (combination of the implanted antenna and biological layers around it). The Fresnel region will be between reactive near field and far-field [22]. In Fig. 2.1a, the angular distribution of the electrical intensity begins to smooth out and forms lobes moving from near-field to far-field in the free-space section of Fig. 2.1a. The dashed curve (at a radius of 34 mm from the TX antenna) indicates an approximate border between the reactive near-field and Fresnel regions at 3 GHz. The red dashed curve in Fig. 2.1a (at a radius of 7 mm from the TX antenna) indicates the region where RX placement will receive the strongest signal. Locating the RX antenna in this region will allow the RF signal to be small enough to avoid tissue damage, but strong enough for reliable wireless communications. Hence our system will work in the near-field rather than far-field for propagation. The close proximity of transmitter and receiver antennas (the mutual coupling between the antennas) makes it impossible to treat transmission loss as independent of the antenna design (as is typically the case). The channel cannot be investigated separately from the antennas [23], but encompasses transmitter and receiver antennas and all adjacent tissues. S_{21} is the electromagnetic wave coupling coefficient between the transmitter and receiver antennas and it is the frequency response for this near field communications system.

Antenna design should favor the broadside direction (red arrow in Fig. 2.1a). RF signals below the TX antenna are not useful for communications, and indeed must be attenuated as much as possible to avoid tissue damage to highly sensitive brain cells. When the RX and TX antenna have reflection coefficients below -10 dB and the implanted TX antenna radiation is directive to its broadside and the RX antenna is placed below the red border, we will achieve

the maximum coupling between antennas and reduce insertion loss of the channel. Finally, in Fig. 2.1b we plot a zoomed out image of the E-field intensity, including intensity beyond the Z-Y plane. An inset shows the rough geometry of RX and TX antenna placement whose "shadow" is superimposed on the E-field plots. We see that within the white-dashed circle we find the majority of the E-field power. HFSS simulations for S-parameter calculations need only cover this area to capture near field effects for communications performance and to calculate ASAR, thus reducing simulation time.

The results in Fig. 2.1 are for Scenario 1 with the TX antenna located between bone and dura. For Scenario 2 the TX antenna would be located one layer higher between fat and bone. The tissue impact on antenna response will vary with position, hence antenna design and performance will differ across the two scenarios. But the general behavior of antenna propagation is the same, and we use the same design methodology for each scenario.

2.3 Antenna Design

The implantable UWB antenna is subject to specific requirements that render its design difficult: 1) it is restricted to small dimensions, 2) it must be biocompatible, and 3) it needs to be electrically insulated from the body [4, 5, 16–20]. Antenna size should be on the order of that of the implantable neural recording system [3, 10, 14]. Planar monopole antennas have simple geometry, small size and wide bandwidth [12, 13]. We propose a monopole microstrip antenna combined with a truncated ground plane covered by a biocompatible material to achieve wide bandwidth. Previous results show that employing an insulating layer increases the performance of the antennas [24–26].

The feed-line is a microstrip transmission line having 50-Ω impedance over the UWB bandwidth. The dimensions of the transmission line are a function of the electrical properties of the substrate as well as the environment (tissues and biocompatible material) surrounding the substrate. In [25, 26] we examined various biocompatible materials and settled on an Al_2O_3 superstrate with a thickness of 1 mm and relative permittivity 9.2 to yield the best compromise for small size.

As we are designing a single polarization antenna, current induced on the antenna should follow a single axis of propagation. A rectangular propagator yields the highest linearity in current. As the rectangular propagator is much wider than the transmission line, the return loss will tend to be narrowband. We therefore adopt a taper geometry to couple the propagator to the transmission line at the widest bandwidth [9]. Simulations show that modifying the rectangular ground pad to adopt a staircase shape (truncated ground) provides better return loss. By optimizing the width and length of the staircase, we optimize return loss. In HFSS we modify antenna dimensions and gauge the impact of surrounding biological tissues using the finite element method. We vary the length of the microstrip transmission line, the length of

a transversal, symmetric strip to the transmission line, and the size of the ground plane, and calculate S_{11} and directivity at broadside for the entire UWB band. This numerical method is repeated for TX1 (under skull, i.e., scenario 1), and TX2 (above skull and under skin and fat, i.e., scenario 2) until optimal dimensions are found. The next section describes antenna performance that was optimized. The RX antenna outside the head is less constrained in size and our design constraints can be relaxed. For the RX antenna we adopt the same geometry as TX antennas, but without insulating layers. We optimize S_{11}, but not directivity. Optimal dimensions of the antennas are reported in [26]. We fabricated these designs, and present results in section 2.5.

2.4 Simulated Performance

The performance of our three antenna designs is examined via HFSS simulation. The antennas were designed for the worst case (maximal signal attenuation) tissue thicknesses. The performance of these designs is examined when implanted in the worst and best cases.

2.4.1 Radiation and Return Loss

Figure 2.2a shows simulated directivity and gain as a function of frequency for TX1 and TX2 for implantation in a worst case and a best case head geometry. For all scenarios, the air gap between the receiver antenna and the skin was set to 2 mm. Greater frequency resolution was simulated as compared to results reported in [26]. In all cases directivity is above 0 dB, i.e., the antennas are directive at broadside. Because the loss in biological tissues increases with frequency, the gain of the antenna decreases roughly with frequency for implanted antennas (Fig. 2.2b). The radiation patterns of implanted antennas are directional due to the presence of the dura, the CSF and the brain (because of their high absorption and high permittivity), as can be seen in Fig. 2.1a.

Simulation results for reflection coefficient (S_{11}) are shown in Fig. 2.3a and 2.3b for the worst and best cases. The reflection coefficient is smaller than -10 dB within the UWB frequency range from 3.1 GHz to 10.6 GHz for each antenna. A properly designed pair of antennas for short-range UWB communications has a TX antenna where 1) S_{11} is less than -10 dB and 2) directivity is more than 0 dB at the broadside. For the RX antenna, S_{11} must be below -10 dB when located where the TX antenna has highest radiation intensity [6]. The simulation S_{21} (the channel frequency response) results for both scenarios are plotted in Fig. 2.4a (magnitude) and 2.4b (phase). In general, it shows that channel insertion loss increases with tissue thickness (the worst case having thicker tissues than the best case) and frequency. At higher frequencies, the loss tangent of tissues increases, which causes more loss when electromagnetic waves propagate though the tissues. As absorption in tissues increases with frequency, system performance will increase when exploiting lower frequencies. From Fig.

2.4b, the channel phase is almost linear. When the channel frequency response has non-linear phase, signal distortion can result.

The group delay provides a measure of required guard time to avoid inter-symbol interference (ISI) due to signal distortion which it is defined:

$$\tau(\omega) = -\frac{d\theta(\omega)}{d\omega} \tag{2.2}$$

The computed group delay for this channel is shown in Fig. 2.4c. The maximum group delays are 130 ps and 160 ps for the worst case of scenario 1 and 2 respectively, and confined to frequencies around 7.8 GHz. Discrete multi-tones could be used to avoid data transmission in this frequency band. Pulse shaping could be used to place more power between 3-7 GHz. Pulse shaping could alternatively be used to create short UWB pulses, leaving pulses separated by more than the worst case maximal group delay [27, 28]. In conclusion, at a bit-rate of 430 Mbps the effect of ISI is negligible. Therefore, the only constraining parameter to achieve this bit-rate (with a certain BER performance) is the transmitted power which translates to the received signal-to-noise ratio (SNR). In section 2.6, we discuss how our link can push data rate to our targeted 430 Mbps data rate which is enough to support 512 channels.

2.4.2 Federal Communication Committee (FCC)

UWB transmissions are limited by regulation. In the far field propagation of implanted antenna, we have a limitation on maximum transmitted power. The maximum power of the transmitter plus maximum antenna gain (Pt+Gt) must be below 41.3 dBm/MHz. We will see that this constraint is greater than that imposed by limiting tissue damage (found in the next section). UWB bandwidth is around 7 GHz, thus the Pt+Gt allowed is [29]:

$$P_t + G_t = -41.3[dBm/MHz] + 10 \times log_{10}(7000) = .5mW \tag{2.3}$$

The best case for the first scenario has a maximum gain of around -8.8 dB at 5.2 GHz. The best case for the second scenario has a maximum gain of around -6.3 dB at 5.8 GHz. Therefore the maximum Pt for the first scenario is 3.9 mW (5.96 dBm), and 2.2 mW (3.46 dBm) for the second scenario. In essence, the best case channel sees less signal attenuation, leading to greater restrictions to reduce potential interference.

2.4.3 Specific Absorption Rate (SAR)

ASAR (Average Specific Absorption Rate) is a critical parameter for assessing the tissue safety of our transmissions. The peak 1-g ASAR distribution (maximum ASAR in every tissue) versus frequency is simulated with HFSS for both scenarios using only the worst case parameter set. Note that worst case for signal attenuation is also worst case for ASAR as greater tissue thickness has electromagnetic waves encountering more tissue. The average transmitted power at the excited port of the antenna in HFSS must be below 4.5 mW in order

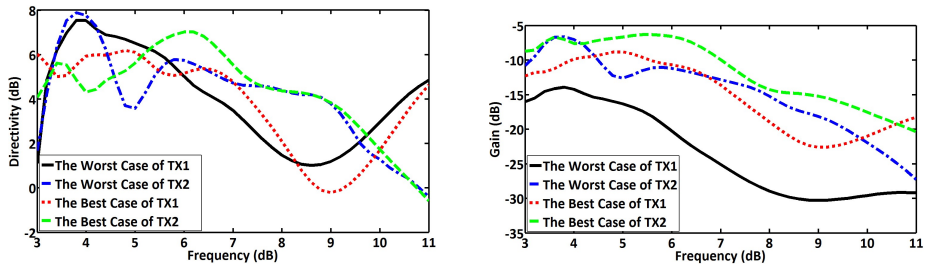

(a) (b)

Figure 2.2: Simulated parameters for implanted antennas (a) directivty at broadside direction (b) gain at broadside direction.

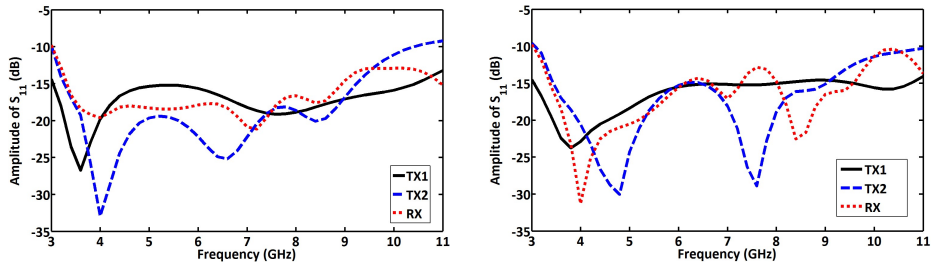

(a) (b)

Figure 2.3: Simulated S_{11} for the antennas (a) the worst case (b) the best case.

to have an average absorption-rate of less than 1.6 W/kg (ANSI limitation [30]) in all tissues in the UWB frequency range. This average transmitted power is equal in both scenarios; transmitting more power results in tissue damage.

This power is smaller than the 8 mW power level calculated in [6] for the biomedical frequency band of 402–405 MHz to satisfy the ANSI SAR limitation. This is understandable as head tissue has significantly more loss in the UWB band than the 402–405 MHz band. Figure 2.5 shows the ASAR for each tissue. In the first scenario, most power is absorbed by the skull (bone). For the second scenario, the skin has highest ASAR.

2.4.4 System Performance

For both antenna placement scenarios, the ANSI restrictions (4.5 mW) are less restrictive than those imposed by the FCC (3.9 and 2.2 mW) for maximum power, so maximum power is set by the FCC criteria. In practice, both constraints are higher than easily achievable signal powers from implantable devices without amplification. The sensitivity of the receiver is obtained from (1.1). For a link margin of 6 dB, the worst case sensitivities of the receiver for both the first and the second scenarios with worst transmission losses of -38 dB and -28 dB at 10.6 GHz are around -38 dBm and -30.5 dBm, respectively. As can be seen in Fig. 2.4a, operation at lower frequency enables better receiver sensitivity, and better detection, because there is lower transmission loss.

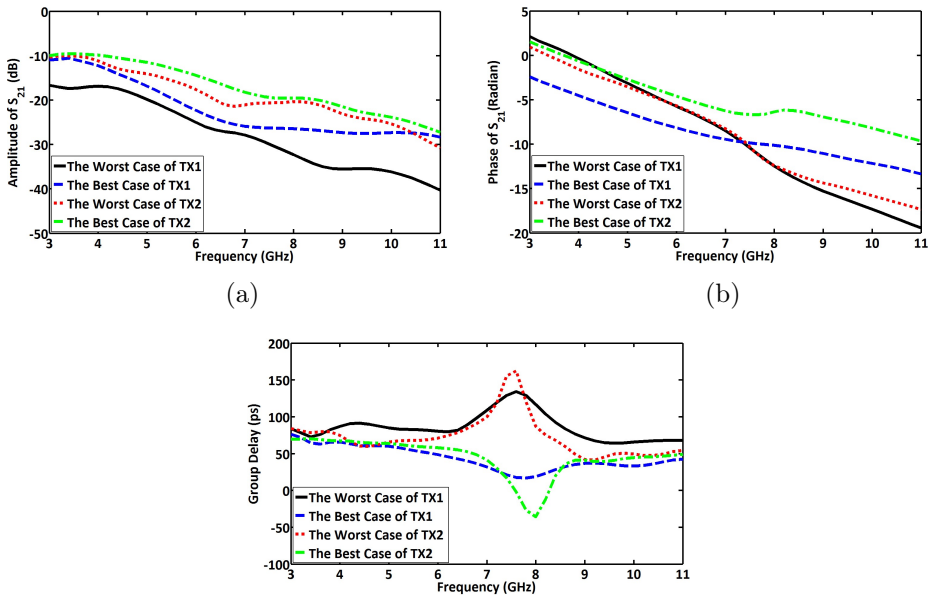

(a) (b)

(c)

Figure 2.4: Simulated parameters for the antennas for two scenarios and best case and worst case (a) amplitude of the channel, (b) phase of the channel, and (c) group delay of the channel.

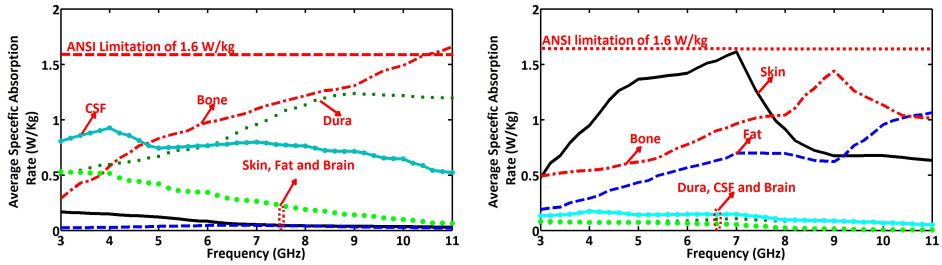

(a) (b)

Figure 2.5: Simulated ASAR for different tissues (a) position under skull (b) above skull.

2.5 Fabrication and Measured Performance

In order to verify our simulation procedure in a realistic environment, we fabricated 12 mm × 12 mm monopole antennas on a FR-4 PCB board with a thickness of 0.8 mm and a dielectric constant of 4.4. A 50-Ohm subminiature A (SMA) connector was used to connect the feeding strip; its outer side was grounded to the ground plane. A 27 mm × 30 mm monopole receiver antenna was fabricated as well (RX). Photos of antennas are provided in Figures 2.6a, 2.6b, and 2.6c. As seen in Fig. 2.6d, implanted antennas are assumed to couple to a neural recording chip via a wire. To mimic implantation, we found animal tissues with thicknesses falling between the worst case and best case values given in Table 2.1. It was not possible to find tissues with exactly the best or worst case thicknesses. In this section we present measurements and compare them to simulation results found with the thicknesses used in

tissues for the experimental measurements.

2.5.1 Network Analyzer Measurements

As reflection coefficient is a function of surrounding tissues, measurements were made in ex vivo using fresh brain and bone tissues of a sheep, as well as fat and skin from a chicken. The air-gap between the larger, external antenna and the skin was set to 2 mm in both simulation and measurements. For scenario 1, the antenna was placed underneath the skull, on top of the brain and the bone, and the skin and fat were put back in place to cover the antenna. For scenario 2, the antenna was placed on top of the skull, underneath the fat and skin. Actual tissue thicknesses used in the measurement are 0.5, 1, 4, 0.5, 0.5 and 30 mm for skin, fat, bone, CSF, dura and brain, respectively.

In simulations, the relative permittivity and loss tangent of human tissue (not animal) were used, with the actual thicknesses of the animal tissue present in experiments. S_{11} and S_{21} of the antennas were measured using an HP-8722ES network analyzer over a 8-GHz bandwidth, from 3 to 11 GHz. Figure 2.7 shows the experimental setup for S-parameter measurements for both scenarios. Figure 2.8 compares the simulated and measured S_{11} (reflection coefficient) for all three fabricated antennas. Results show good impedance matching across a bandwidth of 3–10.6 GHz (S_{11} below 10 dB across the UWB band).

Although there is a slight difference between simulation and experimental results, they still match (within 3 dB). Figure 2.9a and 2.9b compare simulation and measurement results for S_{21} (both amplitude and phase). Figure 2.9c shows the comparison between the simulated and measured group delay. The electrical parameters of head tissues of most animals (except for some animal tissues like porcine skull) closely match those of humans [31]. However, these parameters do not exactly match, and slight differences between measured and simulated results arise. The differences can be attributed to: 1) inevitable deviations of electrical parameters of the test setup from those of the simulated model due to tissue age, temperature, the time passed since its death, etc. [32–34], 2) parasitic effects caused by soldering the SMA connector to the PCB and the PCB fabrication errors, 3) uncertainty in the reported electrical parameters in the literature [35], and 4) presence of a small error in HFSS simulations due to convergence. Taking into account all these factors, we find the deviations between simulations and measurements acceptable.

2.5.2 Anechoic Chamber Measurements

Measurements were performed in an electromagnetic anechoic chamber with biological tissues present (using appropriate antenna geometry for each scenario). The radiation pattern at 7 GHz (center frequency) was measured and is presented, in the XZ and YZ planes for both scenarios, in Fig. 2.10. Patterns at other frequencies showed similar behavior. The measured patterns are in good agreement with the simulated patterns. Clearly our modeling captures

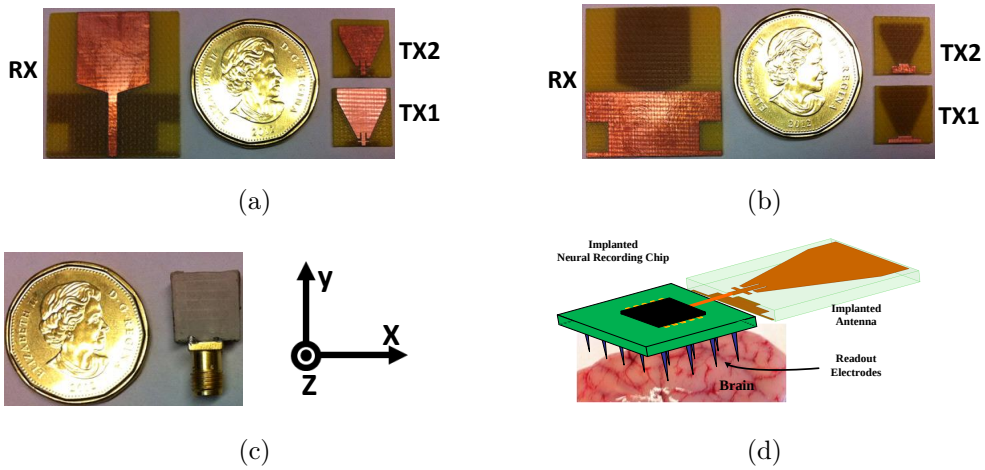

Figure 2.6: The fabricated antennas (a) radiator side, (b) ground plane side, (c) implanted antenna covered with an insulating layer (Al_2O_3 ceramic substrate ($\varepsilon_r = 9.8$)), and (d) illustration of connection of implanted antenna to integrated recording chip.

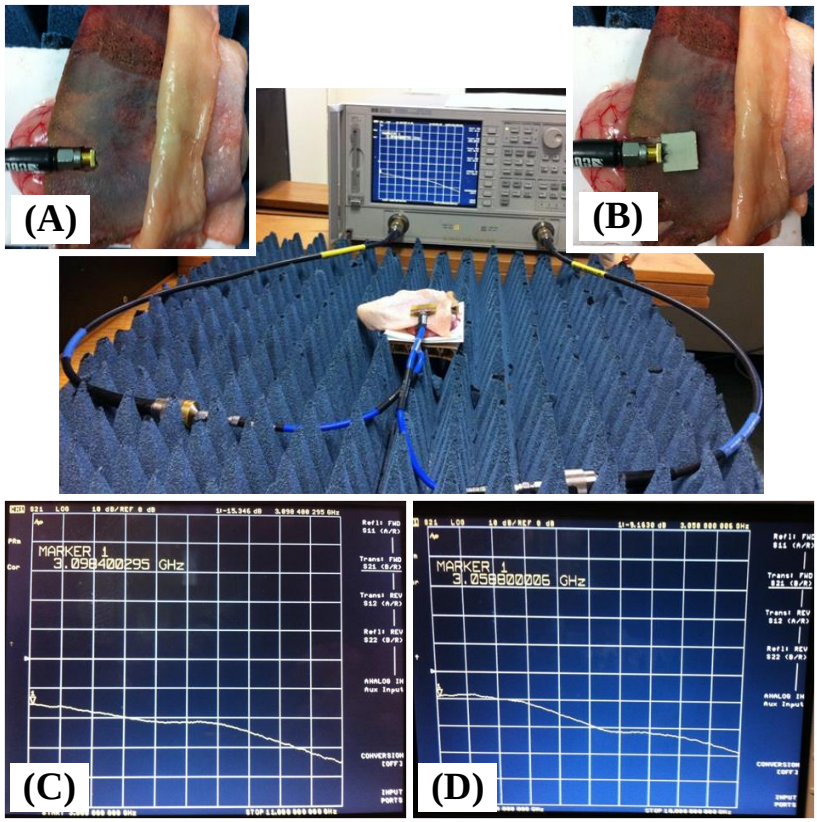

Figure 2.7: Setup for S-parameter measurement; A and B mimic biological model for scenarios 1 and 2, respectively; C and D are screen shots of transmission losses for scenarios 1 and 2 respectively.

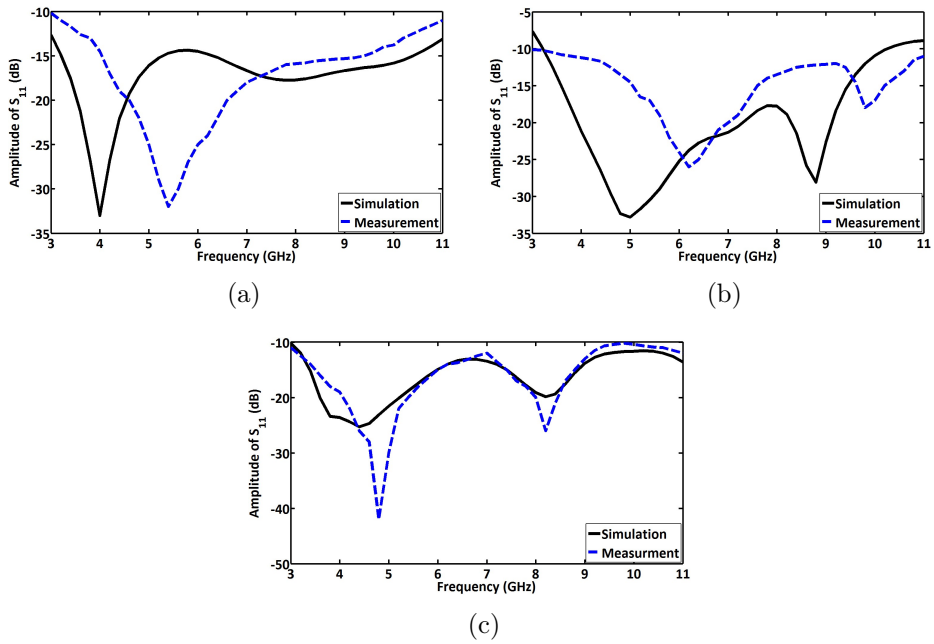

Figure 2.8: Comparison of simulated and measured return losses (a) the TX antenna for scenario1, (b) the TX antenna for scenario 2, and (c) the RX antenna.

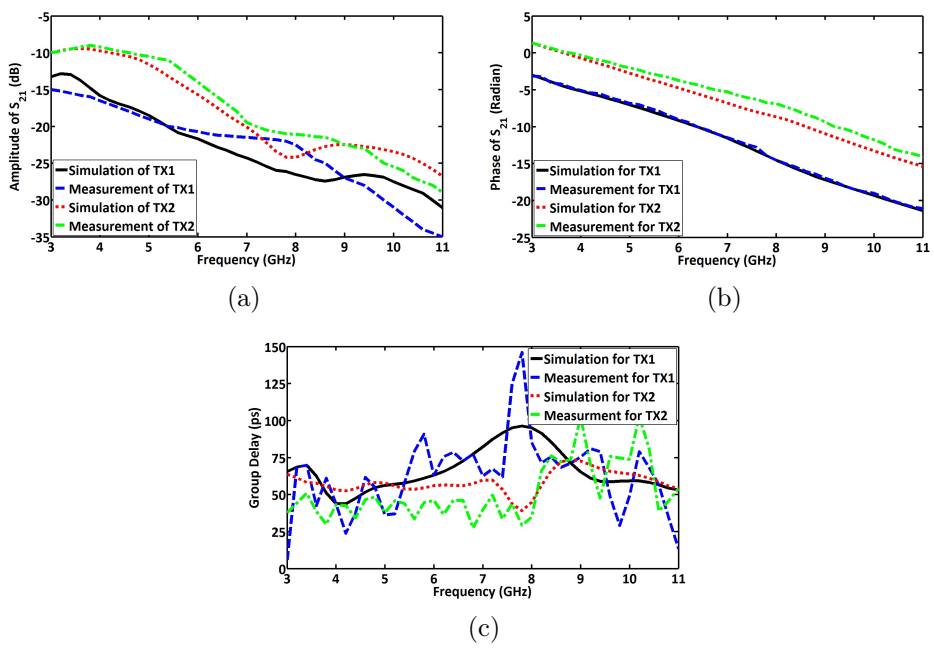

Figure 2.9: Comparison of simulated and measured (a) amplitude of the channel, (b) phase of the channel, and (c) group delay characteristic of scenario 1 and scenario 2.

the influence of the human tissues on the antenna radiation patterns and it can be seen that the effective antennas (combination of the biological tissues and the actual antenna) are directional. There is a slight distortion in the YZ plane, both in simulation and measurement results. Despite this small distortion, the directivity peak of the implantable antennas is properly located at broadside. The radiation pattern is perturbed by layers sliding on each other when the antenna is rotated (by the motor that rotates the antenna when measuring the radiation pattern). The radiation measurement of the antennas with biological tissues is a challenging task because of the difficulties of keeping the tissue layers in a fixed position relative to one another. As expected, the omnidirectional radiation of monopole antenna in free space has become directional due to the reflection and absorption by the tissues, such as the dura, CSF and the brain.

By measuring the radiation patterns in E and H planes for each frequency, the directivity peak at broadside has been calculated using the following formula for different frequencies [22]:

$$D_0 = \frac{4\pi}{\theta_1 \times \theta_2} \tag{2.4}$$

where

θ_1= half-power beam-width in one plane.

θ_2= half-power beam-width in a plane at right angles.

The maximum total gain vs. frequency in the broadside direction ($\theta = 0$ and $\phi = 0$) was measured. From these results, the efficiency of the antenna (shown in Fig. 2.11) is calculated by dividing the gain by the directivity. The antenna efficiency is much lower than the one for antennas designed for free-space applications, which are typically having efficiencies around 70% [22], because the antenna is surrounded by the lossy biological environment. Figure 2.11 shows that the antenna efficiency is greatest at lower frequencies where biological tissues have lower losses.

2.6 Potential for High Data Rate

In wireless communications, bit-error rate performance (BER) is limited by several factors including inter-symbol interference (ISI), maximum allowable transmitted power, path-loss, etc. When ISI is not present, the only constraint on achieving higher bit-rates, for a specific bit -error rate (BER), is the signal-to-noise ratio [11]. Avoiding ISI requires wide bandwidth. For data-rates of several hundred kilobits per second, the 400-MHz and 2.4 GHz frequency bands can be used for implant-to-air communications [36, 37].

However, for multichannel neural recording applications, the implanted transmitter needs higher data -rates. For this reason, we use UWB modulation techniques due to its wide bandwidth. However, UWB signaling suffers from large attenuation for implant-to-air, which

leads to performance degradation. Therefore, characterizing the wireless channel is crucial. Several papers have studied different parts of the body as a wireless digital communication

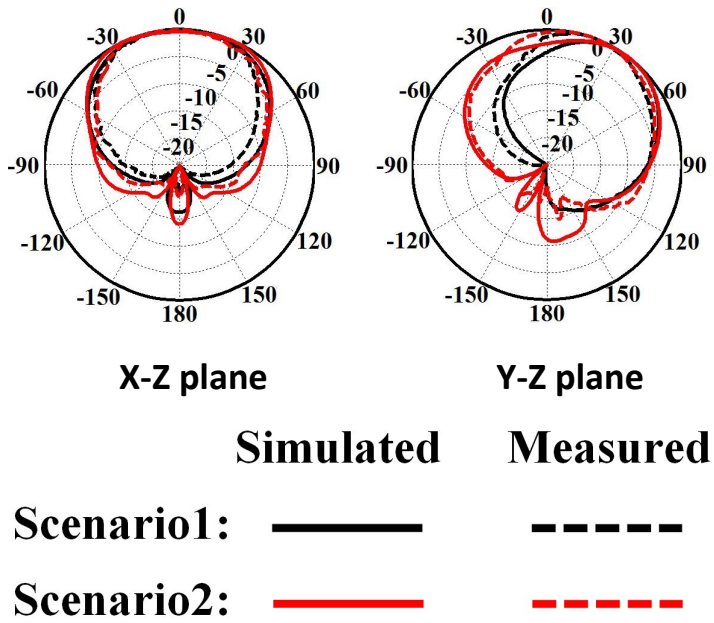

Figure 2.10: Comparison of measured and simulated radiation pattern in the XZ plane and YZ plane for 7 GHz.

channel; however, none has studied the head [38–42]. Recently, two papers have investigated implant-to-air data communications [43, 44]; one has a multi-pulse position modulation (MPPM) transmitter with a bit-rate of 1 Mbps [43] and another has a multi-band orthogonal frequency division multiplexing (MB-OFDM) wireless system with a bit-rate of 80 Mbps [44]. In those systems, the distance between the TX and RX antennas is around 120 mm in [43] and 33 mm in [44], which results in greater loss than our system with 10 mm separation. Additionally, their transmitters respect the FCC limitations assuming free-space transmission. A TX antenna surrounded by biological tissues suffers significant signal attenuation before leaving the body. Therefore, the implanted transmitters can transmit more power to compensate the loss, as long as tissue damage is avoided. In [44], the antenna was designed for free-space, which also results in much more channel insertion loss. The BER performance of implant-to-air UWB data communications for high-speed applications and the capacity of UWB wireless channel for neural recording systems have been discussed in [45, 46].

2.7 Conclusion

Designing a reliable wireless data link in the presence of lossy tissues featuring frequency dependent dielectric properties is a challenging task. In this paper we introduced a methodology for designing a reliable wireless link for neural recording system using tissue modeling and de-

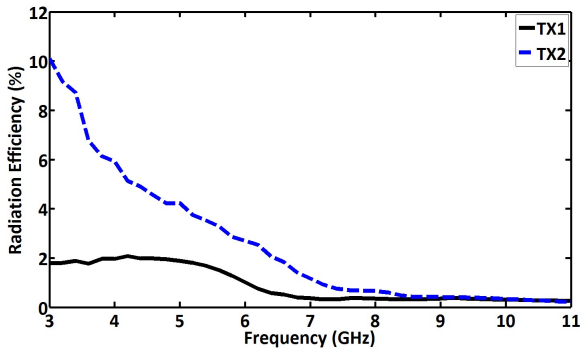

Figure 2.11: Measured radiation efficiency of the TX antennas at broadside (ϕ= 0, θ= 0) for scenario 1 and 2.

signing suitable antennas. For neural implants the antennas and the channel cannot be treated separately and needed to be simulated holistically. Simulations were carried out with HFSS, exploiting a layered model with different dielectric constants to capture the effect of surrounding tissues. The maximum power allowed to be transmitted from the implanted antenna, taking into account the limits imposed by both the ANSI and the FCC, was deter-mined. Then receiver sensitivity was evaluated for two scenarios for transmitter antenna placement.

We reported simulation and experimental results for the two scenarios in a UWB wireless link for neural recording systems. Two UWB microstrip monopole antennas were designed and fabricated as the implantable transmitter antennas. A receive antenna was also designed, fabricated and tested. To verify our modeling and design procedure in a realistic environment, measurements were made in ex vivo using fresh brain and bone tissues of a sheep, as well as fat and skin from a chicken. Measurements matched simulation results, validating our approach. Our results are significant as the measured S_{21} between the receiver and the transmitter antenna allows derivation of the impulse response of the link, and hence computing of the achievable bit error rate of the communication link.

Chapter 3

Flexible, Polarization-Diverse UWB Antennas for Implantable Neural Recording Systems

Abstract

In this chapter, published in [J2], we design single and dual-polarization antennas for wireless ultra-wideband neural recording and stimulating systems using an inhomogeneous multi-layer model of the human head. Antennas made from flexible materials are more easily adapted to implantation; we investigate both flexible and rigid materials and examine performance trade-offs. The proposed antennas are designed to operate in a frequency range of 2–11 GHz (having S_{11} below -10 dB) covering both the 2.45 GHz (ISM) band and the 3.1–10.6 GHz UWB band. Measurements confirm simulation results showing flexible antennas have little performance degradation due to bending effects (in terms of impedance matching). Our miniaturized flexible antennas are 12 mm $\times$ 12 mm and 10 mm $\times$ 9 mm for single- and dual-polarizations, respectively. Finally, a comparison is made of four implantable antennas covering the 2-11 GHz range: 1) rigid, single polarization, 2) rigid, dual polarization, 3) flexible, single polarization and 4) flexible, dual polarization. In all cases a rigid antenna is used outside the body, with an appropriate polarization. Several advantages were confirmed for dual polarization antennas: 1) smaller size, 2) lower sensitivity to angular misalignments, and 3) higher fidelity.

3.1 Introduction

In this chapter the main contributions are:

- A methodology for designing flexible single- and dual-polarization antennas.
- Definition of a figure of merit for near-field communications of neural systems.

- Comparison of single- and dual-polarization antennas for this application.

As we mentioned in the previous chapter, the design of a miniature antenna surrounded by biological tissues must take into account the effects of the tissues. Additionally the brain tissues are physically sensitive in nature and flexible antennas, being more supple and more easily introduced into surrounding tissue, are highly suitable for use in implanted systems [47, 48]. Different wearable flexible antennas have been designed taking into account the effects of biological tissues [49, 50]. In [47, 48], different types of flexible implanted antennas were designed for the ISM and Med-Radio bands. To our knowledge, all reported implanted microstrip UWB antennas are rigid.

In our previous chapter, we designed a rigid single-polarization UWB microstrip antenna for neural recording systems [25, 26, 51]. Single-polarization antennas performance degrades in the presence of angular misalignment between TX and RX antennas, which dual-polarization antennas can correct [22,52–54]. Most narrowband flexible implanted antennas reported in the literature are single-polarization [47, 48]. Implantable antenna with flexible substrates to be placed inside the head must be biocompatible, and as thin and as soft as possible. In [55, 56], a type of Kapton polyimide substrate showed these features.

In this chapter, we employed the same substrate as used in [55, 56]. The copper (antenna) on this substrate is covered by an identical layer of polyimide as is the superstrate. In section 3.2, we present the simulation setup for designing the antenna and identify the important criteria in designing the wireless link. In section 3.3 we describe the antenna design methodology. Section 3.4 presents simulation and measurement results. Performances of different antennas were measured in realistic conditions by placing the antennas in fresh brain and bone tissues of a sheep, as well as fat and skin from a chicken. Reported simulation results closely match our measurements. Section 3.5 compares the flexible and rigid, single- and dual-polarization antennas in terms of 1) average specific absorption rate (ASAR), 2) power efficiency, 3) fidelity, and 4) a figure-of-merit (FoM) defined in section 3.5. Finally, conclusions are drawn in section section 3.6.

3.2 Modelling and Methodology

As we discussed in previous chapters, the multi-layer model [21] used to design the antennas includes brain matter, cerebro-spinal fluid (CSF), Dura, bone (skull), fat, and skin, as shown in Fig. 1.2. Antenna design for implanted medical devices should favor the broadside directivity [25,26,51], as RF signals below the TX antenna are not useful for communications, and indeed must be attenuated as much as possible to avoid tissue damage to highly sensitive brain cells.

As already mentioned, in order to achieve the maximum coupling between TX and RX antennas, 1) their reflection coefficients (S_{11}) must be kept below -10 dB (in order to have acceptable

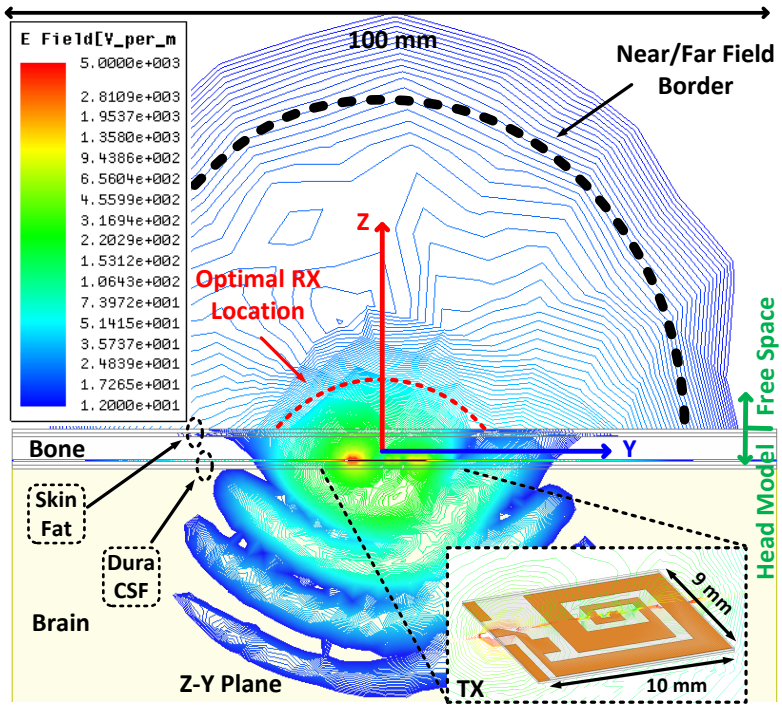

Figure 3.1: Propagation behavior of E field intensity around the implanted antenna in Z-Y plane (referenced to 1 W transmitted power by the antenna).

matching with a 50 ohm impedance), 2) the implanted TX antenna near-field radiation pattern must be directed towards its broadside, and 3) the RX antenna must be positioned at the intensity peak of the radiated EM field (outside the biological tissue). Our first step is designing a 50 ohm transmission line connected to the antenna propagator, while taking into account the effect of biological tissues. The next step is finding initial dimensions of the propagator to meet required specifications (i.e., S_{11} below -10 dB for both TX and RX antennas and near-field directive radiation towards the broadside of the TX antenna) at a single frequency. Next, the propagator dimensions are optimized to extend the antenna bandwidth to achieve the bandwidth of interest. Details of design are given in the next section. The red dashed curve in Fig. 3.1 indicates the region where the RX antenna will receive the strongest signal. Placing the RX antenna in this region (near-field) allows to transmit an RF signal small enough to avoid tissue damage, but strong enough for reliable wireless communications.

3.3 Antenna Design

Planar monopole (single-polarization) antennas have the potential to meet the mentioned constraints in the previous chapter for implanted biomedical systems [12, 25, 26, 51]. However, angular misalignment between these antennas degrades the received signals heavily. In order to alleviate this problem, dual-polarization TX and RX antennas can be used [22, 52–54].

Recently rigid single-arm spiral antennas have been used for capsule endoscopy, body area networks and implantable neural recording systems [10, 57, 58]. The antennas presented in [57, 58] are narrowband and operate at frequencies lower than those of UWB communications. These antennas were also rigid. The rigid antenna in [10] was designed without considering the biological tissue effects. In this study we designed four types of TX antennas, two implanted single-polarization antennas (flexible and rigid) and two dual-polarization antennas (flexible and rigid). Two external single- and dual-polarization antennas were designed as RX antennas.

Our signal-polarization and dual-polarization antennas are realized as monopole microstrip and single-arm spiral antennas, respectively and are covered with a biocompatible material (Kapton polyimide). For all antennas, the feed circuit is a coplanar waveguide transmission line (CPW) having 50-Ω impedance over the 2-11 GHz frequency range. We have chosen the CPW since its integration into the system, i.e., wire-bonding to the implantable chip, is convenient and straightforward. Dimensions of the CPW transmission line are designed respecting the electrical properties of its substrate as well as those of the surrounding biological tissues. We use 0.1 mm Kapton polyimide as the biocompatible substrate for the flexible antennas. The rigid antennas have an Al_2O_3 substrate with a thickness of 0.7 mm. The relative permittivity of Kapton polyimide and Al_2O_3 is 3.5 and 9.2 respectively. For both antennas, a superstrate layer identical to their substrate layers covers the metal antenna traces. This superstrate layer completely isolated the antenna from the biological tissues making the antennas fully biocompatible. The RX antennas, located outside the head, are less constrained in size and flexibility, so the design process is less complicated. Our RX antennas are fabricated on a FR4 substrate (relative permittivity 4.4). RX antennas have the same structure as TX antennas, however, since they do not need to be biocompatible, they do not have the superstrate layer and they are slightly larger.

3.3.1 Single-Polarization Antennas

We proposed a monopole antenna that was optimized for implanted biomedical applications with a rigid substrate in the previous Chapter. In this work, we revisited the design from chapter 2, using the same methodology but incorporating a flexible substrate more suitable for neural implantation. We modified the transmission line dimensions for the TX and RX antennas to accommodate the new substrate and/or superstrate that are appropriate.

3.3.2 Dual-Polarization Antennas

Single-polarization antennas suffer from angular misalignment [22, 52–54], which can be overcome using dual-polarization antennas. We design two implanted dual-polarization flexible and rigid TX antennas and one rigid dual-polarization external RX antenna.

As in the previous section, the first step of design is tuning the CPW transmission line to have a 50-Ω impedance in the frequency range of interest. We incorporate a spiral propagator

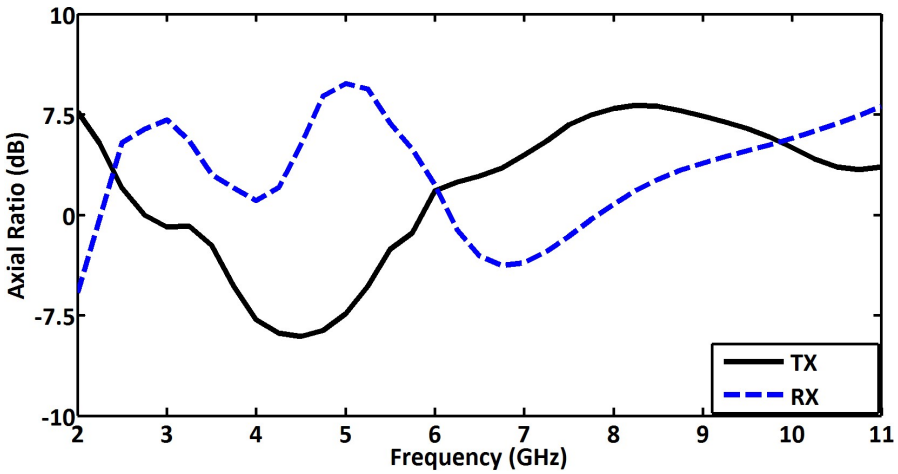

Figure 3.2: Simulated axial ratio of the dual polarization flexible TX and rigid RX antennas.

structure that induces a current equally on the antenna in both the horizontal and the vertical axes. The spiral structure of the propagator consists of several rectangle-shaped pieces of copper placed on the X and the Y axes with shared current.

To have equal radiated power in the X and Y directions, the total length of the rectangles in each direction must be equal. We achieve an S_{11} below -10 dB in the frequency range of interest (2-11 GHz) by matching the spiral propagator to the 50-Ω transmission line. To improve S_{11} bandwidth (while keeping it below -10 dB), the width of each rectangle in the spiral propagator is tuned. We placed the rectangular shapes as close as possible to decrease the antenna size.

During optimization of the antenna dimensions, the maximum near-field radiation intensity is checked to assure it is directed towards the broadside over the desired frequency range. Figure 3.3 shows the induced current on implanted (TX) and external (RX) antennas. The current is distributed almost equally in the X and Y directions.

We examine the axial ratio, i.e., the ratio of orthogonal components of an E-field. To calculate the axial ratio (Ex/Ey), a single polarization antenna is needed to capture S_{21} in the X direction (representative of Ex) and S_{21} in the Y direction (representative of Ey) of the antenna of interest. For the implanted flexible TX dual polarization antenna, the external RX single polarization antenna is used. To calculate the axial ratio of the RX dual polarization antenna, the implanted flexible TX single polarization antenna is used.

The simulated axial ratio is shown in Fig. 3.2. Every attempt was made to orient antennas for maximum coupling and least insertion loss in the simulation. Because the implanted antenna is roughly three times smaller than the external antenna and the TX and RX antennas are very close to each other, Fig. 3.2 is our best approximation of the axial ratio.

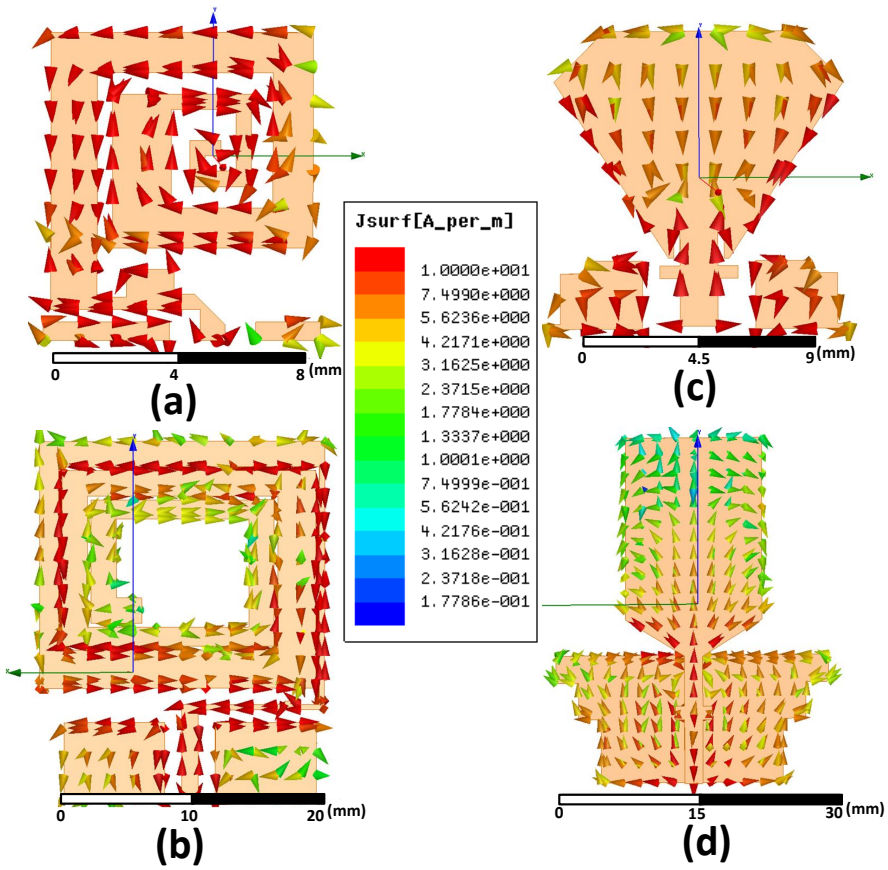

Figure 3.3: The induced current on the antennas (a) TX, (b) RX for the single-polarization antennas, (c) TX, and (d) RX for the dual-polarization antennas.

3.4 Simulation and Measurement of S-Parameters

3.4.1 Measurement Setup

In order to verify our simulation results, we fabricated six antennas on different PCBs (flexible and rigid). Table 3.1 summarizes the properties of the fabricated antennas. Two of the antennas are receiver antennas (single- and dual-polarization) and the other four are the implanted transmitter antennas. A 50-Ω SMA connector connects the antenna to the measurement equipment. We used the following animal tissues: skin (0.5 mm), fat (0.5 mm), bone (3 mm), CSF (0.5 mm), Dura (0.5 mm) and brain (30 mm), thicknesses chosen to mimic typical human head tissues [28]. The S_{11} and S_{21} of the antennas are measured using a HP-8722ES network analyzer from 2 to 11 GHz. Figure 3.4 shows the block diagram and setup used for antenna S-parameter measurements. For characterizing the flexible and rigid single-polarization TX antennas, the single-polarization RX antenna is used. For the dual-polarization TX antennas, the dual-polarization RX antenna is used. To show that the dual-polarization antennas are

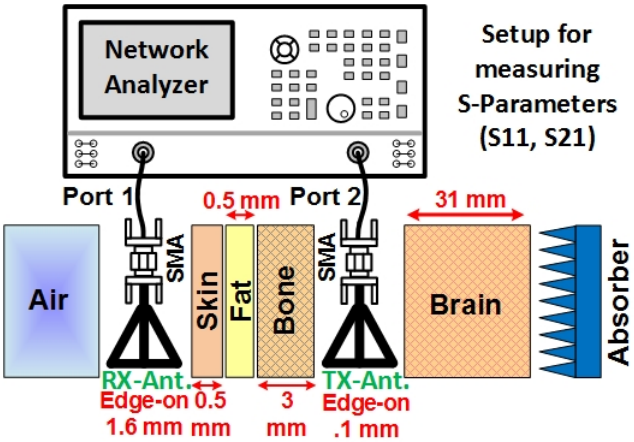

(a)

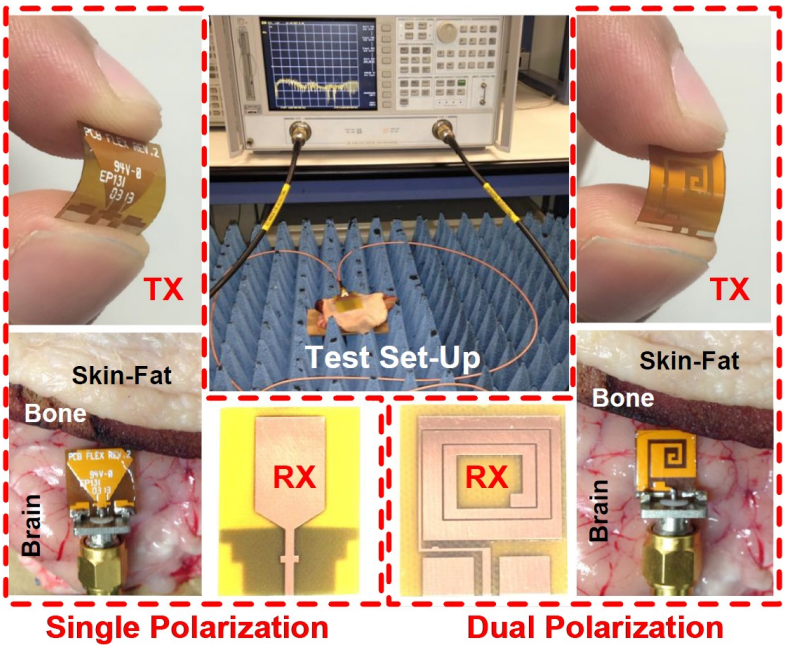

(b)

Figure 3.4: S-parameter measurement (a) Block diagram of the set-up, and (b) the set-up, for S-parameter measurements.

not sensitive to angular misalignment, we fixed the implanted TX antennas and rotated the RX antennas to three different angles (0, 45 and 90 degrees) which are illustrated in Fig. 3.5.

3.4.2 Flexible Single- and Dual-Polarization Antennas

Figure 3.6a shows the measured and simulated S_{11} of the single-polarization (flexible) TX and (rigid) RX antennas and Fig. 3.6b shows the measured and simulated S_{11} of the dual-

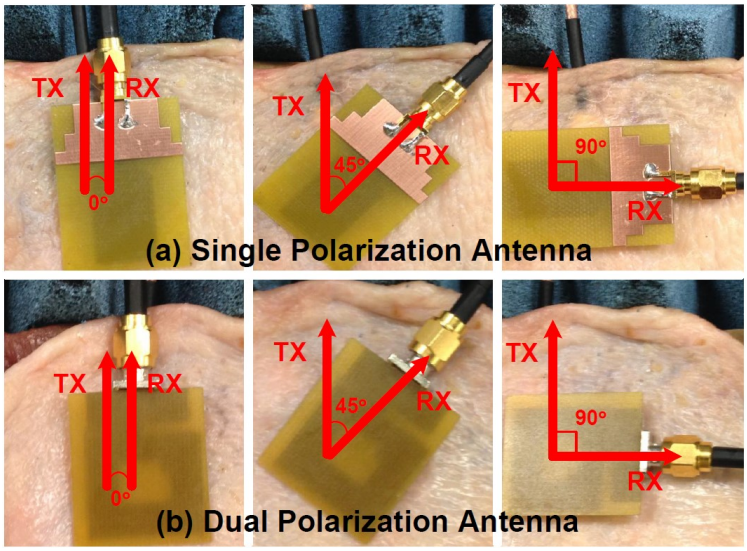

Figure 3.5: Set up for characterizing sensitivity to angular misalignment between TX and RX antennas (a) single-polarization antennas, and (b) dual-polarization antennas.

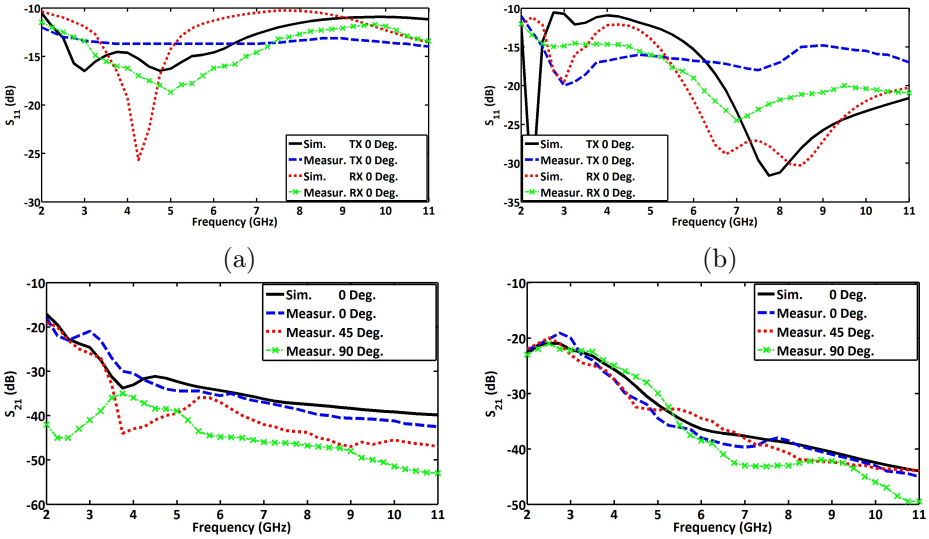

Figure 3.6: Simulated and measured S-parameters for implanted flexible antennas for different angular missalignment between TX and RX (a, c) single-polarization, and (b, d) dual-polarization.

polarization (flexible) TX and (rigid) RX antennas. S_{11} results show good impedance matching (S_{11} below -10 dB) across the 2-11 GHz frequency range. From a practical point of view, the discrepancies between the simulation and measurement of S_{11} results are not important as long as S_{11} remains below -10 dB. Figure 3.6a and 3.6b clearly show that simulated S_{11} acceptably predicts the behavior of the antennas in measurements (below -10 dB).

Contrary to S_{11}, the frequency behavior of S_{21} is important since it is the wireless channel frequency response. Figure 3.6c and 3.6d present simulation and measurement results of S_{21} (amplitude) for the antennas. For all antennas the S_{21} simulation and measurement results follow the same trend.

For both polarizations, HFSS simulations and experimental results agree. Sources of small differences between the measured and the simulation results can be attributed to: 1) inevitable deviations of electrical parameters of the test setup from the simulated model because of animal age, temperature, time passed since animal death, etc. [31, 34], 2) parasitic effects caused by soldering the SMA connector to the PCB and PCB fabrication error, 3) uncertainty in reported electrical parameters in the literature [35], and 4) residual error in HFSS numerical solutions. Despite these issues and inaccuracies, the HFSS simulations predict the antenna performance well. The lower S_{21} values at lower frequencies indicate that the body has lower loss at these frequencies. This frequency band should be exploited for implant-to-air communications. As shown in Fig. 3.6c and 3.6d, when the RX antenna is rotated the dual-polarization antennas have almost the same insertion loss.

Table 3.1: Characteristics of TX and RX antennas

Tissue	TX	TX	TX	TX	RX	RX
Polarization	single	dual	single	dual	single	dual
Width (mm)	12	9	12	10	30	26.3
Length (mm)	12	10	14	11	40	30
Thickness (mm)	0.1	0.1	0.7	0.7	1.6	1.6
Thickness (mm)	0.1	0.1	0.7	0.7	NA	NA
Permittivity	3.5	3.5	9.8	9.8	4.4	4.4
Substrate	flex	flex	rigid	rigid	rigid	rigid
Material	Poly-imide	Poly-imide	AL2O3	AL2O3	FR4	FR4

3.4.3 Comparing Flexible and Rigid Antennas

Finally, Fig. 3.7 presents measurements demonstrating that there is no significant compromise in performance due to the use of a flexible substrate. Antennas are designed as described in section 3.3 to the same performance targets and are implemented on both flexible and rigid substrates. In total four antennas are fabricated as both single and dual polarization are investigated. In Fig. 3.7a, we see almost indistinguishable performance for all four antennas, all of which achieve our goal for S_{11} below -10 dB in the 2-11 GHz frequency range. The

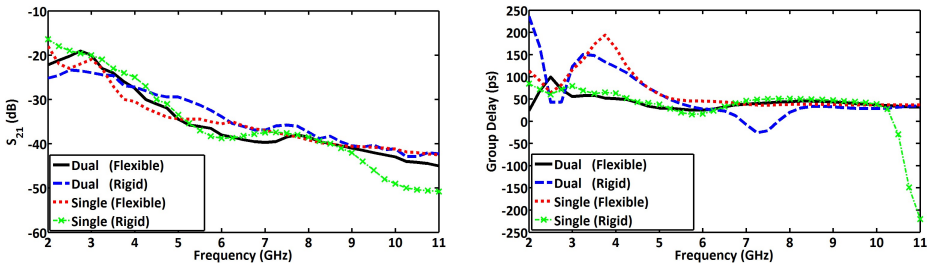

(a) (b)

Figure 3.7: Comparison of the measured results of the antennas (a) S_{21}, and (b) group delay.

measured group delay in Fig. 3.7b shows that the flexible dual-polarization antenna exhibits the best performance of the four antennas, introducing little pulse distortion across the entire UWB frequency band. In conclusion, flexible and rigid antennas have similar efficiency, while in our opinion, flexible antennas are likely to offer less risk of tissues damage.

3.5 Near-Field Characteristics of Antennas

In near-field communications, the close proximity of the transmitter and receiver antennas leads to high mutual coupling between the antennas. Transmission loss is therefore not independent of the antenna effects [25,26,51]. In this section, we discuss the efficiency of antennas from a near-field link viewpoint. We find the ASAR and the received power when a specific signal is transmitted for each implanted antenna. Furthermore, we define fidelity and a figure-of-merit (FoM) for the near-field link.

3.5.1 Specific Absorption Rate (ASAR)

Average Specific Absorption Rate (ASAR) describes the electromagnetic energy that is absorbed in biological tissues and is a critical parameter for assessing the tissue-safety of implant-to-air wireless communications. The peak 1-g ASAR spatial distribution versus frequency is simulated in HFSS for all four implanted antennas. The results are presented in Table 3.2. ANSI limitations for a maximum peak 1-g ASAR of 1.6 W/kg [30] translates into different average radiated power for each antenna: 3.5 mW for single-polarization flexible and rigid implanted antennas, 5.7 mW for flexible dual-polarization antennas, and 3.9 mW for rigid dual-polarization antennas. Sending more power can damage the biological tissues. Figure 3.8 shows that most of the radiated power is absorbed by the skin for single-polarization and by the Dura for dual-polarization antennas.

3.5.2 Power Efficiency

Both ASAR limitations on tissue damage and FCC limitations on maximum transmitted power lead to challenging reception of UWB signals [51]. The pulse selected for transmission will

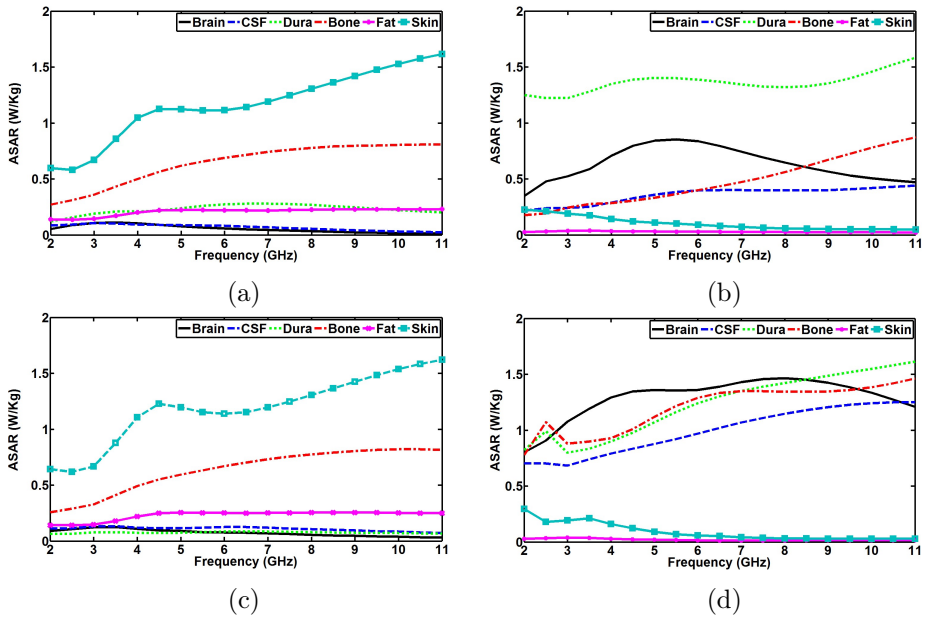

Figure 3.8: The simulated ASAR of the implanted antennas and calculated allowable maximum transmitted power (PMax) for (a) rigid, single-polarization (PMax = 3.5 mW), (b) rigid, dual-polarization (PMax = 3.9 mW), (c) flexible, single-polarization (PMax = 3.5 mW), and (d) flexible, dual-polarization (PMax = 5.7 mW).

influence the power efficiency. We investigate via simulation the anticipated received power when our antenna is used with a common UWB pulse shape. The excitation pulse is shown in Fig. 3.9a; it consists of a Gaussian-modulated sinusoidal waveform mathematically described by [59]

$$V(t) = \sin(2\pi f_0(t - t_0)) \times e^{\frac{(t-t_0)^2}{2\tau^2}} \tag{3.1}$$

where f_0 = 6.5 GHz, τ = 120 ps and t_0 = 3 ns. This pulse has a temporal width of 0.6 ns and its frequency spectrum is centered at 6.5 GHz with a bandwidth from 2 to 11 GHz (Fig. 3.9b).

MATLAB was used to characterize the performance of the near-field link using the measured S-parameters of each TX and RX antenna-pair. Simulation results include the reflected power, received power and the dissipated power. To calculate the reflected signal, the spectrum of the pulse is multiplied by S_{11}; for the received signal, the spectrum of the pulse is multiplied by S_{21}.

Table 3.2 shows the portion of the total power that is reflected from the TX antennas and received power (power efficiency) by the RX antennas. This table also shows the amount of power dissipated in the antenna and the environment. It can be seen that the antenna reflected power is relatively low and most power is propagated. Received power is low; we note, however, that these results depend on the excitation waveforms and their spectrums, which can be optimized.

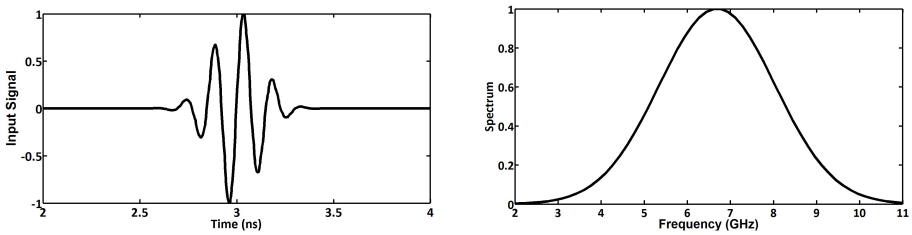

(a) (b)

Figure 3.9: (a) Waveform of the Gaussian modulated sine wave described by (3.1), and (b) its spectrum.

3.5.3 Fidelity Factor of the Near-field Links

System performance is optimized when the received waveform is a replicate of the transmitted waveform with no distortion. Simple design goals for amplitude and group delay attempt to minimize the distortion. Unlike narrowband antennas, UWB antennas can significantly alter transmitted pulses, due to considerably different behavior across the wide frequency band [60,61]. The antenna fidelity factor (in the far-field) captures the similarity between the ideal expected output waveform of an antenna and the actual radiated waveform. The antenna is assumed to introduce one of three effects (replication, integration or derivation), which we refer to as the antenna effect, that is incidental to the design process. For a given pulse shape, the result of an ideal antenna effect acting on that pulse shape is different from the actual radiated waveform. The fidelity factor is defined as the maximum cross-correlation between the ideal and the actual radiated waveforms when both waveforms are normalized by their energies [16,59–61]. Fidelity varies between zero and one, with one showing the minimum and zero showing the maximum distortion introduced by the antenna.

The impact of UWB transmit antenna geometry, material, current mode and transmitter impedance interact to a combined effect that might introduces integration or derivation instead of simple replication [60,61]. More importantly, the TX antenna can interact with other system components (exciting pulse shape, communication channel, and receive antenna geometry, material, etc.) to have an overall effect which we call the link effect. This behavior can be particularly influenced by operation in the near-field. We define a fidelity factor for near-field applications. Unlike the far-field definition of fidelity, our near-field definition considers the effect of the TX antenna, the radiation medium (the biological tissues) and the receiver antenna characteristics. Let r(t) be the received pulse for an ideal link effect (which we assume takes one of three forms of replication, integration or derivation) for a given excitation pulse shape. Let Sr(t) be the actual received waveform for that excitation pulse shape. The near-field fidelity is defined as the following assuming r(t) and S_r(t) have normalized energies

$$F = \max \int_{-\infty}^{+\infty} r(t) \times S_r(t+\tau)dt \tag{3.2}$$

We examined the four transmit antennas we designed (dual/single polarization, rigid/flexible

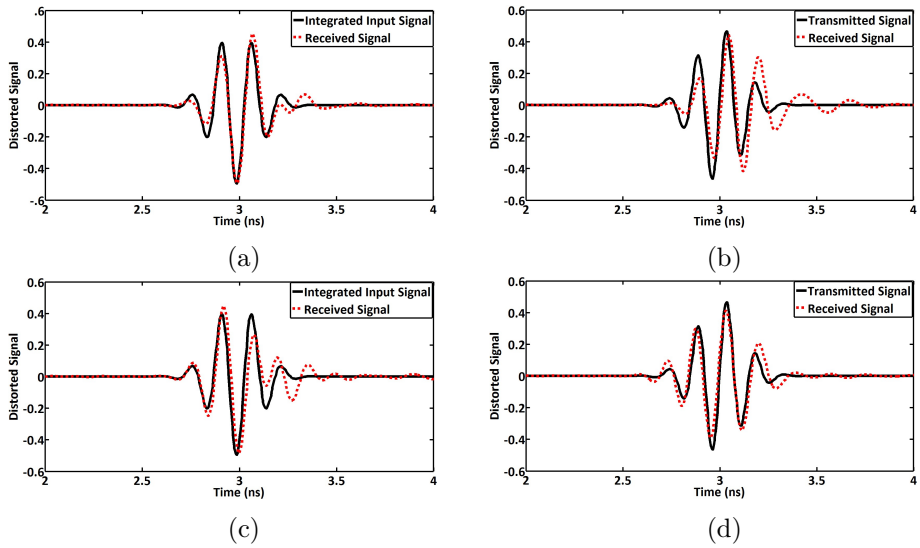

Figure 3.10: Distorted received pulse which is calculated based on the measured S21 for antennas with (a) flexible, dual-polarization, (b) flexible, single-polarization, (c) rigid, single-polarization, and (d) rigid dual-polarization.

substrate) and determined the link effect for each for the near-field biological channel. As indicated in Table 3.2, we found the single polarization, flexible substrate antenna and the dual polarization, rigid substrate antennas formed a system that replicated the transmitted signal without integration or derivation. The other two antennas formed a link whose overall effect was integration. In Fig. 3.10 we plot r(t) (solid lines) and Sr(t) (dotted lines) for each of the four transmit antennas. We derive Sr(t) by calculating the inverse Fourier transform of the multiplication of the pulse spectrum of (3.1) by the measured S_{21} of the antenna pairs. In two cases the link effect is to replicate the input transmit signal, whereas the other two integrate the input transmit signal. The fidelity factors calculated from (3.2) are given in Table 3.2, showing dual-polarization antennas perform better than single-polarization antennas. In sum, the dual-polarization antennas have three advantages in comparison with the single-polarization antennas: 1) smaller size, 2) lower sensitivity to angular misalignments, and 3) higher fidelity.

3.5.4 Figure of Merit (FoM)

To compare the designed antennas in near-field applications, we propose a figure of merit (FoM). Our FoM is based on parameters that play an important role in the performance of the near-field wireless links: 1) Pe: power efficiency (%), 2) A: TX antenna area (m^2) (RX antenna is much larger than TX antenna and changing its size does not change the link performance when it is close to a small antenna), 3) d: the distance between the RX and TX antennas which in this work is 4.0×10^{-3} m, 4) PMax: maximum allowable transmitted power

Table 3.2: Near-field characteristic of the TX antennas

Performance	single	dual	single	dual
Substrate	flex	flex	rigid	rigid
Reflected Power	2.4%	2%	2.6%	2.8%
Power Efficiency	.04%	.05%	.03%	.11%
Dissipated Power	97.56%	97.95%	97.37%	97.09%
Link Effect	replication	integration	integration	replication
Link Fidelity	.81	.96	.84	.93
FoM	3.2	7.3	2.1	14.5
PMax (mW)	3.5	5.7	3.5	3.9
RX sensitivity (dBm)	-34.6	-31.5	-35.8	-29.7

(mW) (according to ANSI limitations), and 5) F: fidelity factor. The FoM is defined as

$$FoM = \frac{P_e \times d \times F \times P_{Max}}{A} \tag{3.3}$$

In Table 3.2, FoM is calculated for the four designed links with different polarizations. The results show that the dual-polarization antennas have a higher FoM. As a result, this type of antenna is the best candidate for neural recording application.

3.5.5 Bending Effect

Given the size of antennas and the natural curvature of the head, at most 10 degrees of bending would be encountered in vivo. To stress our design, we examined impairments with 30 degrees of bending of the implanted antenna. The S_{11} behavior of the flexible antennas under bending is characterized and shown in Fig. 3.11 (the antennas are bent 30° while still touching the biological tissues). The results show that the S_{11} remains below -10 dB irrespective of bending. Power efficiency passed from .04% and .05% to .03% and .04% for single and dual polarization under 30 degrees flexing, respectively. Fidelity went from 0.81 to 0.72 for single polarization, and 0.96 to 0.81 for dual polarization. Finally, ASAR considerations would lead to the maximum transmit power of 3.5 mW reduced to 1.3 mW for single polarization, and 5.7 mW reduced to 1.5 mW for dual polarization. Bending would lead to some impairment, though parameters are still acceptable even in the extreme 30 degree case.

3.6 Conclusion

We presented a methodology for designing implanted single- and dual-polarization antennas on a flexible substrate for neural recording systems operating over two frequency bands (ISM and UWB). We compared single and dual polarization antennas on both rigid and flexible substrates. We found that no significant performance reduction was incurred in moving to flexible substrates that are better adapted to neurological implants. Several advantages were

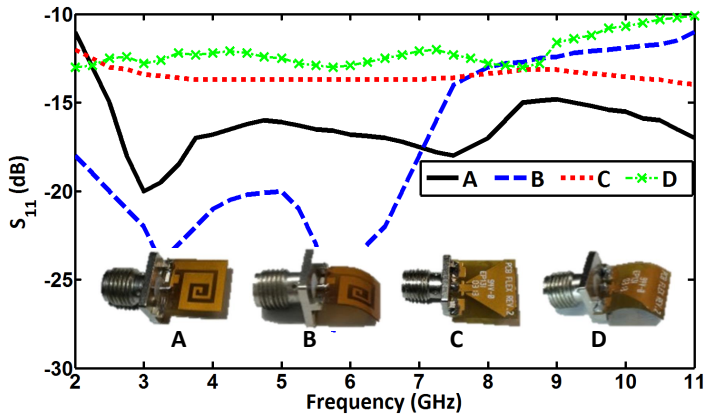

Figure 3.11: Comparison of measured S_{11} (A, C) for zero bending of the flexible TX antennas and (B, D) for 30 degree bending of the flexible TX antennas.

uncovered for dual polarization antennas: 1) smaller size, 2) lower sensitivity to angular misalignments, and 3) higher fidelity.

In near-field implant-to-air biomedical applications, the TX and RX antennas and the biological tissues between them cannot be treated separately and need to be simulated holistically. All our simulations were carried out in HFSS by exploiting an inhomogeneous, multi-layer model of biological tissues. To verify the validity of our model and the antenna design procedure, ex vivo measurements were made using fresh brain and bone tissues of a sheep, and fat and skin from a chicken. Measurement and simulation results are in good agreement and validate the proposed antenna design methodology and biological tissue modeling. We investigated the maximum allowable transmitted power with respect to ANSI limitations. We also simulated and measured the biological channel overall link effect on pulse transmission and reception. Finally, in order to compare the designed antennas for near-field biological applications, a figure of merit has been suggested.

Chapter 4

System Level Design of High-Speed Full-Duplex Transceiver for Neural Recording and Stimulating Systems

Abstract

Results from this chapter were presented in [J3]. We propose a wireless communications architecture for implanted systems that simultaneously stimulate neurons and record neural responses. This architecture supports large numbers of electrodes (>500), providing 100 Mb/s for the downlink of stimulation signals, and Gb/s for the uplink neural recordings. We propose a transceiver architecture that shares one ultra-wideband antenna, a streamlined transceiver working at full-duplex on both bands, and a novel pulse shaper for the Gb/s uplink supporting several modulation formats. We present an ex-vivo experimental demonstration of the architecture using discrete components achieving Gb/s uplink rates. Good bit error rate performance over a biological channel at 0.5, 1, and 2 Gbps data rates for uplink telemetry (UWB) and 100 Mbps for downlink telemetry (2.45 GHz band) was achieved.

4.1 Introduction

In this chapter the main contributions are:

- Proposing a novel full-duplex data transceiver for neural systems.
- Experimental demonstration of achievable data rates of the proposed system.

Simultaneous neural stimulating and recording systems require many electrodes interfaced, perhaps permanently, to the central and peripheral nervous systems. In wireless neural record-

ing applications, increasing the number of electrodes enhances understanding of the targeted part of the brain. More electrodes lead to a requirement for higher speed links.

In neural stimulating and recording systems, as shown in Fig. 4.1, conventionally three separate links are required: one power inductive link and two separate communication subsystems (uplink and downlink) [10, 62, 63]. Inductive data subsystems are utilized when the required data rate is low, on the order of a few Mbps [10, 62, 63]. To achieve a higher data rate for the uplink in a neural recording system, an ultra-wideband RF communication subsystem was utilized instead of the inductive approach; the inductive approach was kept for the downlink [3, 10]. As the number of electrodes increases, the downlink needs wider bandwidth (and hence a higher RF frequency) to be able to support modulated (100 Mbps) datarates. Recently, we proposed 2.45 GHz industrial, scientific and medical (ISM) band as a forward link [64]. We will show in this paper that the 2.45 GHz downlink receiver can be operated in full duplex with a high data rate ultra-wideband band (UWB) uplink transmitter. The

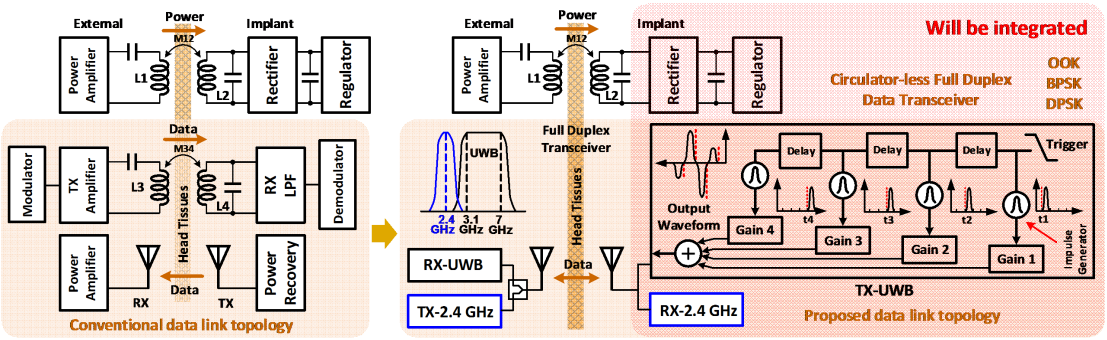

Figure 4.1: Brain-machine interface solutions: (a) conventional architecture with separate uplink transmitter and downlink receivers, and (b) the proposed full-duplex, dual-band transceiver.

most important features for the implanted circuit are small size and very low power consumption [3,3,14,65–67]. To achieve these goals we modify the traditional use of separate uplink and downlink subsystems, and propose a novel full-duplex data transceiver, with one dual band RF bidirectional data link. We avoid a power-hungry circulator by shaping the transmitted signal to take advantage of the low noise amplifier (LNA) filtering feature at the implanted downlink receiver. We shape the transmitted pulse to put most energy between 3.1-7 GHz. This also allows for good isolation from the 2.4 GHz achieving low crosstalk between uplink and downlink. Because of very lossy behavior of head tissues at 7-10.6 GHz [51], this pulse shaping also enhances uplink power efficiency. This novel technique is the simplest possible full-duplex transceiver structure, employing a circuit that is power efficient and small in size, making it suitable for biomedical applications.

The final enabling element for our architecture is an antenna which covers both frequency bands with small size and good performance in biological materials. We develop and fabricated antennas, one implantable and one external, designed specifically for transcranial channels using techniques developed in [51]. The antenna for this work was designed for dual bands, supporting both uplink and downlink, whereas previous designs were for a UWB uplink only. We investigate achievable data rates of the proposed wireless link via ex vivo experiments with discrete components and biological tissues as the transmission media. We examine data rates of 0.5, 1 and 2 Gbps for the uplink. For the downlink for stimulation signals we consider only OOK at 100 Mbps. We confirm that acceptable bit error rates (BER) can be achieved at these rates. These results greatly outstrip previous data rates for biological channels, such as 80 Mbps for wireless implant-to-air data communications for gastro applications [44]. In that work, a multiband orthogonal frequency division modulation (MB-OFDM) was used, which consumes more power than impulse-radio UWB.

In section 4.2, we present an overview of the proposed system. In section 4.3 we describe the experimental implementation of the proposed architecture with discrete components and an implanted antenna surrounded by fresh animal tissues (brain, bone, fat, and skin). Section 4.4 presents measurement results. In section 4.5 we discuss the reasons we were able to improve data rates and present our BER performance. Finally, conclusions are drawn in section 4.6.

4.2 System Architecture

As shown in Fig. 4.1, to date two separate communication subsystems are used for uplink and downlink data transmission. We propose a full-duplex data transceiver which consists of one dual band RF bidirectional subsystem. This architecture minimizes size and power consumption by concentrating on a small set of efficient, integrable components: a single antenna, an LNA that doubles as a bandpass filter, a pulse shaper formed from delay elements and amplifiers. In this section we motivate the selection of this set of components, and contrast them with other solutions available in the literature. In section 4.3 we present an experimental proof-of-concept demonstration for this architecture (destined for integration) using discrete components.

Figure 4.1 shows a block diagram of the proposed transceiver supporting a bidirectional, high-data rate link through the head for neural stimulation and recording. The integrated solution will include a UWB pulse shaping transmitter and a 2.4 GHz receiver with an LNA with limited passband. The design of the external system, not considered here, is less demanding than the implantable system which must be biocompatible and support CMOS integration. Compared to prior solutions, our architecture, eliminates one antenna or inductive link.

4.2.1 Diplexer

We propose one dual band transceiver to replace separate 1) 2.4 GHz band down link antenna and receiver, and 2) UWB uplink antenna and transmitter. The transceiver must operate in full-duplex (stimulation and simultaneous recording). Typically circulators or diplexers are used to implement a full-duplex transceiver (FDT) [68–73]. We are interested in a CMOS compatible solution for integration, hence an active circulator would be required instead of a passive one [68–70]. Active circulators attenuate the signal at least 3 dB, increase size and power consumption, and decrease the signal-to-noise ratio of the receiver. Another solution might be implementing a diplexer (two sharp band-pass filters) to separate the frequency bands [69–73]. These two frequency bands must be very close for coverage by a single antenna (TX and RX). UWB 3.1-10.6 GHz and 2.4 GHz IMS bands are unlicensed bands freely available for bio-applications. Implementing filters to operate in these two bands in CMOS technology would require significant space and add loss to transmitted and received signals.

We thus consider instead a diplexer where two separate frequency bands are supported with good isolation between them. The UWB band (uplink) and 2.4GHz IMS band (downlink) were chosen for the communications bands because 1) the two frequency bands are close enough to be covered by a single antenna, and 2) they are readily available unlicensed bands per Federal Communications Commission (FCC) regulations. We show in the inset in Fig. 4.1 the spectra of a UWB and a 2.4-2.5 GHz signal.

Implementing a diplexer with two band-pass filters would be challenging in CMOS technology. We propose implementing a FDT by 1) shaping the UWB pulse and 2) exploiting the LNA 2.4 GHz passband. The UWB pulse (see next section) is sculpted to have a spectrum beginning at 3.1 GHz. This signal is routed to the implanted antenna. This signal therefore also propagates to the 2.4 GHz receiver. Within that receiver is a low noise amplifier (LNA) designed to operate at 2.4 GHz for reception of uplink signals. The LNA has a limited passband, rejecting any UWB signal components (high impedance in UWB). The FDT thus avoids use of a circulator or separate band pass filters.

4.2.2 UWB Pulse Shaping

UWB impulse radio (UWB-IR) transmits information through short nanoseconds baseband pulses without employing a carrier, leading to advantages such as low complexity, and low power consumption [74,75]. To generate a UWB pulse, a number of methods are available. The choice is affected by several factors such as power consumption, simplicity in implementation, modulation scheme achievable, bit error rate (BER), data rate and so on. Pulse filtering is less space efficient than shaping the pulse [75]. Among different pulse shapes, the Gaussian pulse and its derivatives have a desirable compromise in frequency and time-bandwidth [75]. Gaussian derivatives are widely used in UWB transmitters; their center frequency is increased

when taking an additional derivative and their spectrum bandwidth is optimized by tuning the pulse time duration [75].

We optimize the transmitted pulse subject to multiple constraints. The first one is efficient exploitation of the FCC mask. Second is isolating the transmitter and receiver in our full-duplex structure. The third is matching the frequency response of the biological communications channel. EM waves see more loss at higher frequencies in our channel; we should try to put more power in the lower band of UWB band (3.1-7 GHz). And finally, the achieved pulse duration should be short to support high data rates (to avoid intersymbol interference). We target pulses with 500 ps duration to support data rates as high as 2 Gbps.

To shape the UWB pulse, the amplitude and the time duration of the fifth derivative of a Gaussian pulse is manipulated. The optimized pulse is generated by summing time-shifted Gaussian pulses algorithm as shown in Fig. 4.1. This architecture promises a low power implementation because of its simplicity compared to other pulse shaping methods [76–79]. To provide the systems designer maximum flexibility this architecture has the added advantage of supporting three signaling methods: OOK, BPSK and DPSK. Four impulses are used to shape and generate the required UWB signal for transmitting a logical "1" data during OOK modulation. To produce BPSK and DPSK modulated signals, a similar algorithm is used, producing the same signal with a 180° phase difference when a logical 0" data is transmitted.

The choice of modulation scheme depends on the required BER and data rate, power consumption and system complexity. There is a trade-off between complexity and power consumption, leading us to consider both coherent and incoherent architectures. Coherent detection requires more complex circuitry which results in higher power consumption; incoherent detection is less complex, which results in lower power consumption, but worse BER performance [11]. We consider binary phase shift keying (BPSK: coherent), differential phase shift keying (DPSK: incoherent) and on-off keying (OOK: incoherent) modulations for the uplink. DPSK has the low complexity of incoherent detection and has only a 1 dB power penalty vis-a-vis BPSK for an additive white Gaussian noise channel. A 3 dB power penalty is incurred for OOK [63].

4.2.3 Antenna Design

The final enabling element for our architecture is an antenna which covers both frequency bands with small size and good performance in biological materials. We developed and fabricated antennas in Chapter 3, one implantable and one external, designed specifically for transcranial channels. We designed and fabricated TX and RX spiral antennas that cover the 2-11 GHz frequency band (dual band) using HFSS (a commercial finite element method solver). We plot in Fig. 4.2 the propagated electric-field between the antennas (TX and RX). The illustration shows placement of both antennas and the layers of inhomogeneous model used in the HFSS model. The highest electric-field intensity is localized close to the anten-

nas, leading to higher coupling between the antennas, and thus higher received signal-to-noise (SNR).

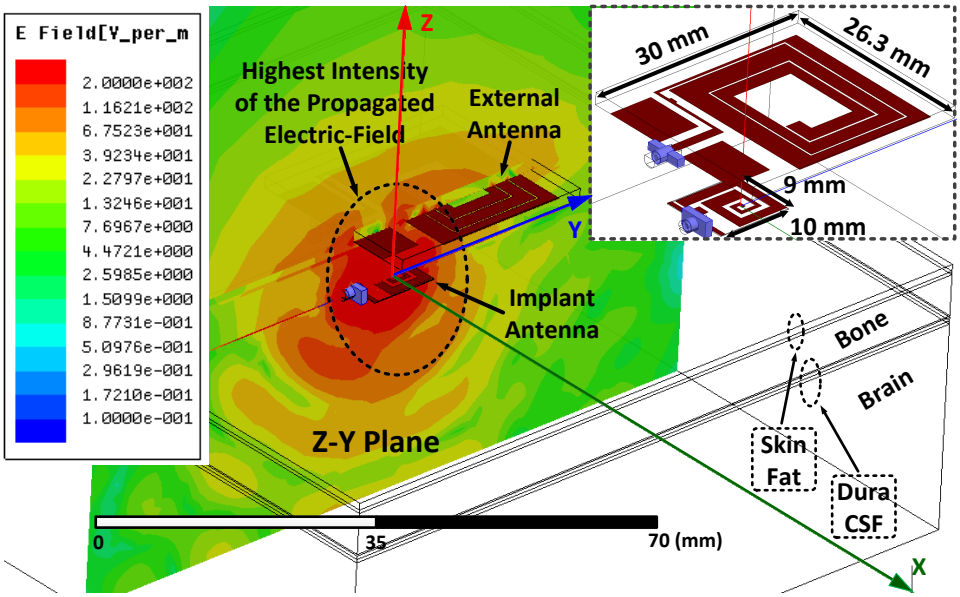

Figure 4.2: Radiated E-field while implant and external antennas are communicating through biological tissues in Z-Y plane in HFSS.

4.2.4 Average Specific Absorption Rate (ASAR)

Average Specific Absorption Rate (ASAR) describes the electromagnetic energy that is absorbed in biological tissues and is a critical parameter for assessing the tissue-safety of implant-air wireless communications. The peak 1-g ASAR spatial distribution is simulated in HFSS for implanted antennas in the 3.1-7 GHz frequency range (transmitter for backward link) and external antenna in the 2.4-2.5 GHz band (transmitter for forward link). The ASAR is calculated for the implanted antenna transmitting on the UWB band, and for the external antenna transmitting on the 2.4 GHz band. The ANSI limitations for a maximum peak 1-g ASAR of 1.6 W/kg [80] translates into the following average radiated power: 6.4 mW (8 dBm) for the implanted antenna and 9 mW (9.5 dBm) for the external antennas. The ASAR for the external antenna is calculated assuming the antenna is placed 0.7 mm from the skin. Sending more power can damage the biological tissues.

4.3 Experimental Proof-of-Concept

In the previous section we proposed an architecture that can be integrated in CMOS technology in smaller size and with lower power consumption than previously proposed systems. In this section we use test equipment and discrete components to measure the achievable bit rates

with this architecture. We test several modulation formats and measure bit error rate when propagating through animal tissue in an ex-vivo trial.

Test equipment and discrete components for our test set-up are shown in Fig.4.3. An arbitrary waveform generator (AWG) is programmed to generate the uplink UWB pulse, a pulse shape resembling that which would be produced by the architecture in Fig. 4.1. The UWB pulse is modulated by a pseudorandom binary sequence (PRBS) of order 15 by the arbitrary waveform generator. One million bits are transmitted using OOK, BPSK, or DPSK modulation. An attenuator is used at the transmitter for sweeping the signal-to-noise ratio (SNR) in the receiver. The attenuator is followed with a UWB bandpass filter to achieve high impedance outside its supported frequency band. The uplink signal in transmitted through the animal tissue. At the external receiver, a 3 dB power divider (22 dB isolation) is used between the two summation ports. The signal is amplified with an ultra-wideband low noise amplifier (LNA) with 27 dB flat gain and noise figure (NF) 4 dB. The uplink signal is captured by a real-time oscilloscope to be analyzed off-line in MATLAB.

In the downlink transmitter, the output of bit pattern generator (PRBS of order 15) running at 100 Mb/s is mixed with a 2.45 GHz tone, followed by an attenuator used for sweeping the SNR. The downlink signal in transmitted through the animal tissue. The 2.4 GHz signal received by the implanted antenna is rejected by the UWB bandpass filter before the uplink transmitter and is diverted to the implanted receiver which is 50 ohm matched. A discrete band-pass filter centered at 2.45 GHz with sharp cutoff is used to emulate the passband of a LNA specially designed for this application. The LNA has NF= 2.1 dB and a gain of 15 dB. The amplified signal is captured by a real-time oscilloscope for processing offline in MATLAB.

We fabricated the implanted antenna on flexible PCB and the external antenna on rigid FR4 PCB. 50 ohm SMA connectors connect the antennas to the other equipment, as shown in Fig. 4.4. To emulate the head environment, the following fresh animal tissues are used: skin (1 mm), fat (0.5 mm), bone (6 mm), and brain (30 mm), thicknesses chosen to mimic typical human head tissues [21]. We measured and plot in Fig. 4.3 the frequency response of the wireless channel (S_{21}), amplitude and phase, using an HP-8722ES network analyzer. We see the insertion loss of the channel increases with frequency. Operation at lower frequencies improves the BER performance of the system. Pulse shaping can help us to put more power of the transmitted pulse in lower frequency and increase link efficacy. Figure 4.4 shows a photo of the measurement setup.

Isolation of the uplink transmitter from the downlink receiver in our implant is challenging. For the external unit we can use a discrete power divider with excellent isolation (22 dB in Fig. 4.3). The implant requires an integrated solution. The UWB uplink transmitter in an integrated solution (on-chip) will naturally have very high impedance, providing isolation to the 2.4 GHz downlink receiver. In our experiment with discrete components (not integrated)

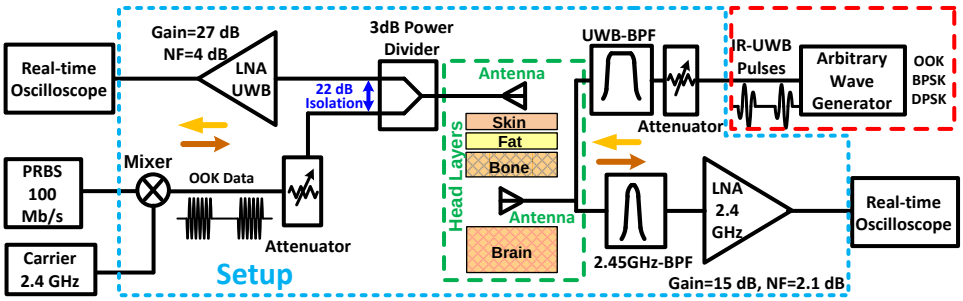

(a)

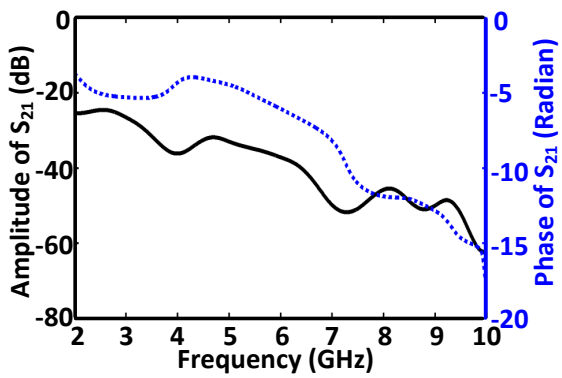

(b)

Figure 4.3: (a) Block digram of the system level implementation of the proposed link, and (b) the measured frequency response of the wireless channel.

we emulate this high isolation via a UWB bandpass filter (see Fig. 4.3). The bandpass filter rejects the 2.4 GHz downlink signal, effectively routing all energy to the 2.4 GHz receiver.

To isolate the 2.4 GHz downlink receiver from flooding by the UWB transmitter, we use pulse shaping. Figure 4.5 shows the measured UWB pulse with OOK modulation at the output of the AWG, as captured by the real-time oscilloscope. In Fig. 4.5 we see the spectrum for the UWB signal. The pulse is shaped to place energy between 3.1-7 GHz, and to introduce a notch at 2.45 GHz, yielding good isolation between uplink and downlink.

The final determination of the effectiveness of isolation is the bit error rate performance of uplink and downlink. We will see in the following sections that measured BER is close to theoretical limits, hence crosstalk is negligible.

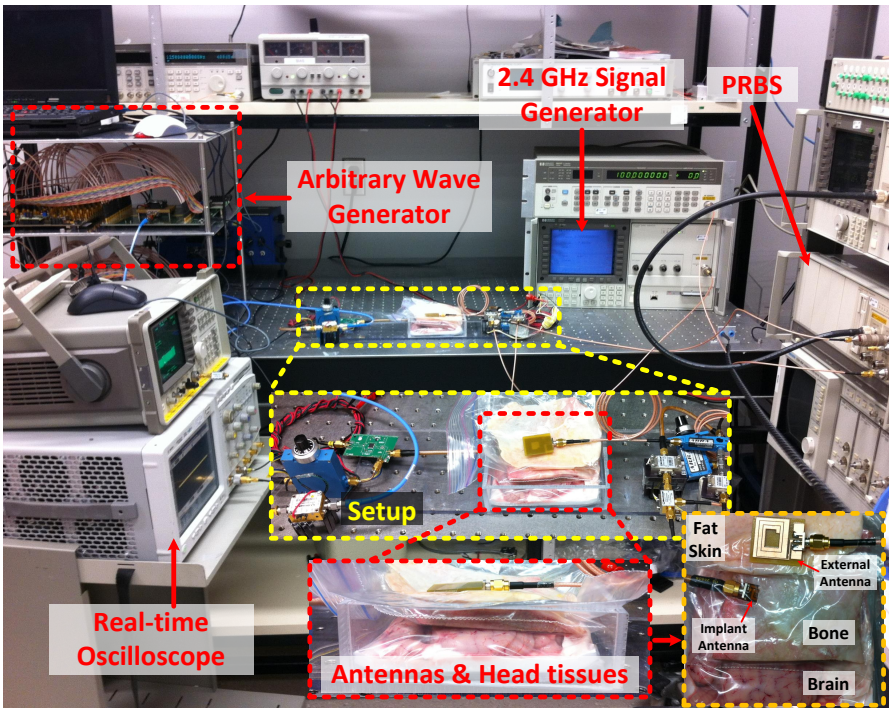

Figure 4.4: Set-up for data communications.

4.4 Experimental Results

To provide the systems designer maximum flexibility this architecture has the added advantage of supporting three signaling methods: OOK, BPSK and DPSK. Each modulation format is briefly described, including the required receiver.

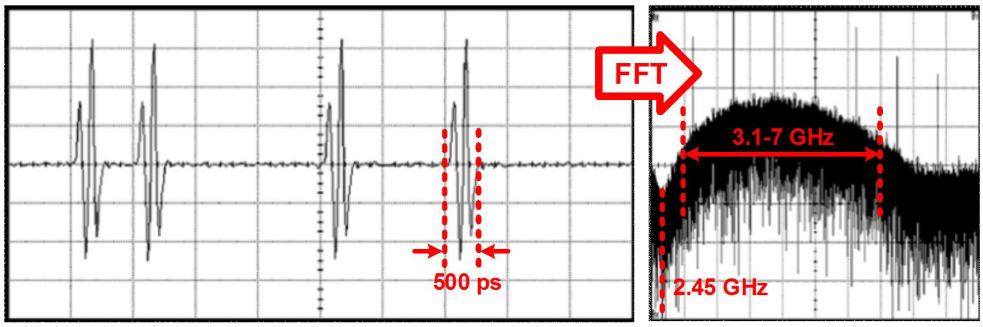

Figure 4.5: Measurment result: (a) OOK modulation waveform in AWG output for 500 Mbps (b) its spectrum.

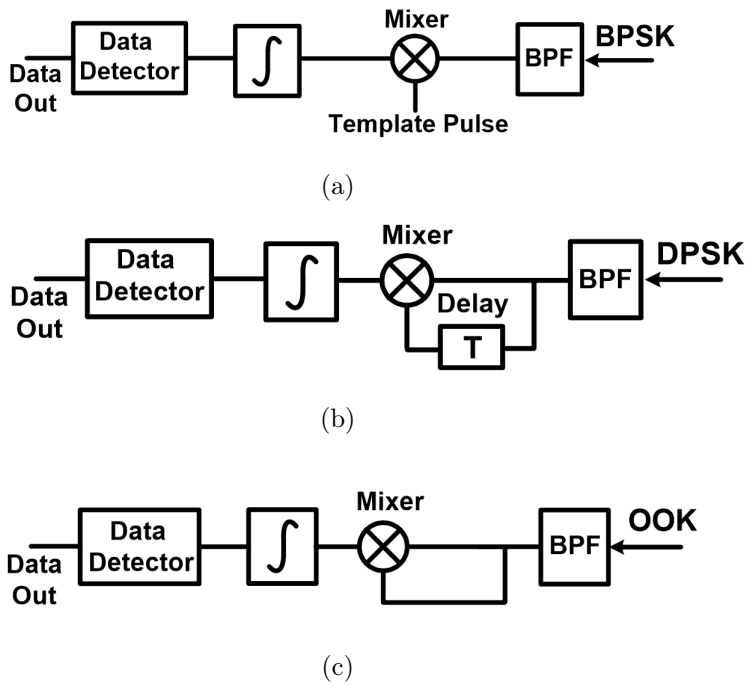

Figure 4.6: Reciver blocks implemented in MATLAB (off-line processing) for (a) BPSK, (b) DPSK, and (c) OOK.

4.4.1 BPSK Modulation

Phase-Shift Keying (PSK) is a modulation scheme in which the phase of a signal is varied to transmit information. In binary phase shift keying (BPSK) the phase of the signal is varied by 180 degrees with the polarity of the binary data. BPSK is detected by using a matched filter or the equivalent correlation receiver. To detect the received signal coherently a template pulse is needed for the correlation receiver as shown in Fig. 4.6. To generate the optimal template, the frequency response of the channel must be known [11]; the measured frequency response of the channel is plotted in Fig. 4.3. The transmitted, received and detected signals are shown in Fig. 4.7a for 500 Mbps and SNR = 20 dB.

4.4.2 DPSK Modulation

DPSK modulation transmits data on changes in phase from symbol to symbol. Because the data are detected by correlation with a delayed version of the received waveform, the data must first be encoded in a differential fashion [11]. Self-homodyne detection (i.e. correlation with a delayed version of the received signal), is followed by integration and detection blocks as shown in Fig. 4.6b. The transmitted, received and detected signals are shown in Fig. 4.7b for 500 Mbps and SNR = 20 dB.

4.4.3 OOK Modulation

On-Off Keying (OOK) is the simplest form of amplitude-shift keying modulation. The presence of a waveform for a specific duration represents a binary one, while its absence for the same duration represents a binary zero [11]. For detection, the received signal is multiplied by itself, integrated and detected as shown in Fig. 4.6c. The transmitted, received and detected signal for the backward link are shown in Fig. 4.7a for 500 Mbps and SNR = 20 dB. Also, the data transmission for forward link is presented in Fig. 4.7d for 100 Mbps and SNR = 20 dB.

Figure 4.6 shows the block diagram of the receiver systems for different modulations, performed offline in MATLAB on data captured by the real-time oscilloscope. For the backward link, Fig. 4.7 shows the modulated waveforms with random digital data at the transmitter, the receiver, and following detector. In Fig. 4.7 "Transmitted signal" is the waveform modulated with a PRBS of order 15 and 1 million bits length for different modulations which is uploaded in AWG. "Received signal" is the signal which is captured by real-time oscilloscope. "Filtered signal" is the captured signal after the band-pass filter in Fig. 4.6. "Integrated signal" is the output of the integrator (a RC low-pass filter) in Fig. 4.6. The red dash-lines in the "Integrated signal" are the sampling times. In order to detect transmitted data, the sampled signal (dashed red line) is compared with a threshold value. "Transmitted signal" in Fig. 4.7d refer to the forward link at output signal of the mixer which is captured by the real-time oscilloscope. "Received signal", "Filtered signal" and "Integral Signal" are similar to those discussed for the backward link. Discussions about different modulations are provided below.

4.5 Data Rates and BER Performance

Recently data transmission performance at 80 Mbps was investigated for wireless implant-to-air data communications for gastro applications [44]. In that work, a multiband orthogonal frequency division modulation (MB-OFDM) was used, which consumes more power than impulse-radio UWB. We were able to push data rates above this previous maximum of 80 Mbps [45]. We achieved 2 Gb/s for neural recording systems (downlink) due to the following. 1) For gastro application, the distance between the TX and RX antennas is 33 mm. The worst case separation for neural recordings is around 10 mm. Smaller separations leads to less signal attenuation.

2) In [44] the transmission powers were chosen to respect the FCC limitations assuming antennas are in free-space. This level was pessimistic as it did not take into account insertion loss caused by biological tissues The true limit should balance avoiding biological tissue damage, while still respecting FCC limitations after attenuation.

3) Antennas in [44] are designed for free-space, resulting in much greater channel insertion

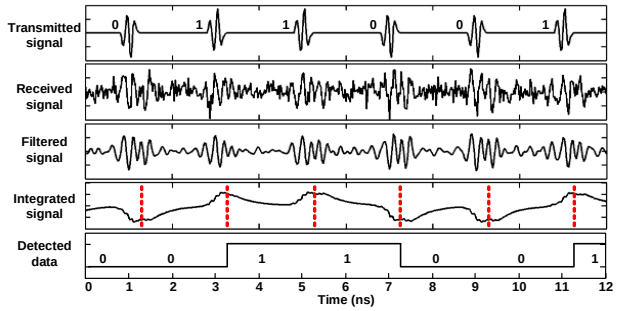

(a)

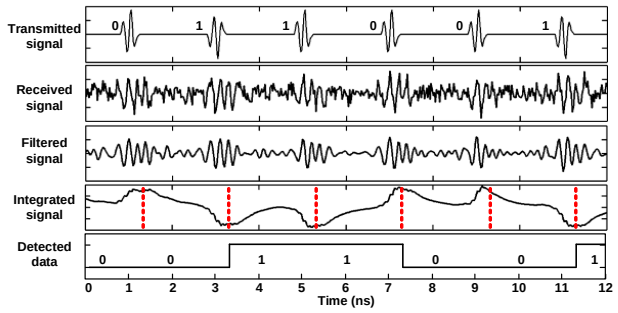

(b)

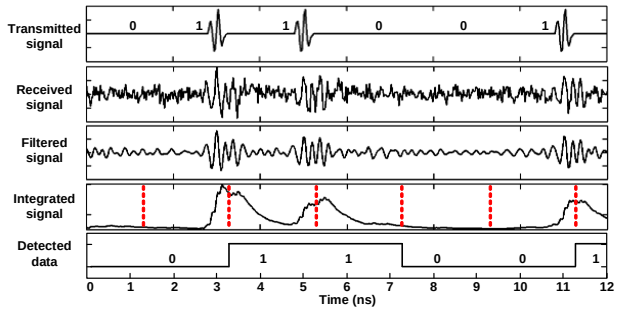

(c)

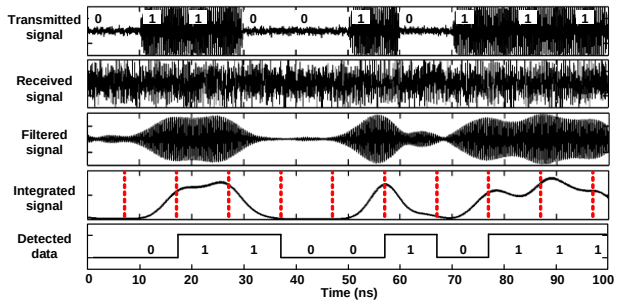

(d)

Figure 4.7: Different stages of data transmission for (a) BPSK uplink, (b) DPSK uplink, (c) OOK uplink, and (d) OOK downlink.

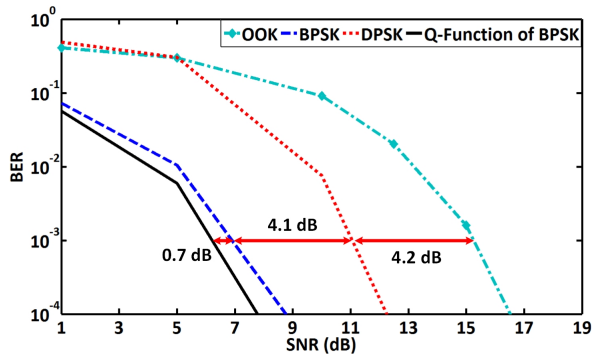

(a)

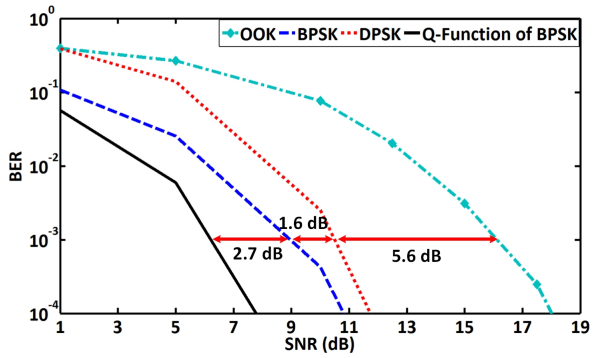

(b)

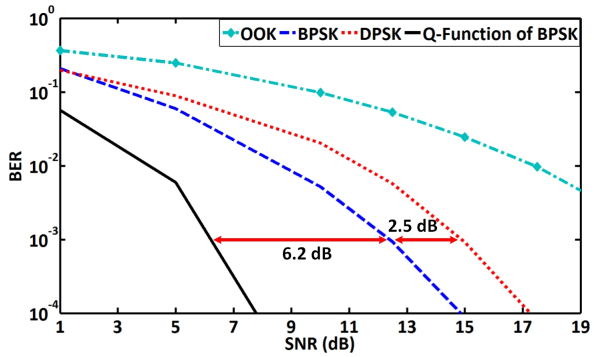

(c)

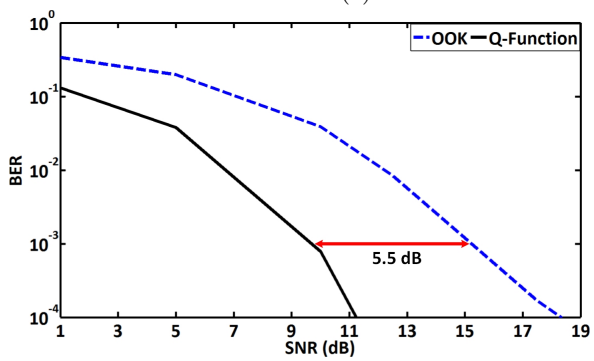

(d)

Figure 4.8: BER for downlink and uplink. Red arrows are SNR penalties at 10^{-3}. Results are for (a) 500 Mb/s uplink, (b) 1Gb/s uplink, (c) 2 Gb/s uplink, and (d) 100 Mbps downlink link. Defference from Q-function between BPSK and DPSK or BPSK and OOK are 1 dB and 3 dB, respectively.

loss.

4) Higher bit rates can be obtained by using more bandwidth than the 528 MHz used in [44].

Our architecture addressed these four points to improve bit rate, while retaining a low-power, small-form factor, and CMOS compatible solution.

The transmitted data is captured by the real-time oscilloscope for UWB and 2.4 GHz links simultaneously. The BER is calculated and the BER vs. SNR of each link is presented in Fig. 4.8. Uplink BER appears in Fig. 4.8 a-c for BPSK, OOK and DPSK modulations at 500 Mbps, 1 Gbps and 2 Gbps, respectively. The downlink BER is presented in Fig. 4.8d for OOK modulation at 100 Mbps. During measurements for each SNR step, the modulated waveforms are transmitted through the biological tissues are detected per Fig. 4.6 (manipulations in signal processing rather than hardware). Typical traces are as presented in Fig. 4.7.

The SNR penalties between modulation formats at 0.001 BER are shown in the Fig. 4.8. As expected, the best BER performance is obtained by BPSK. When the data rate is increased, the BER performance is reduced due to the ISI effect. Increasing the data rate leads to greater ISI and worse BER performance. However, equalization techniques can be used to solve this issue at rates above 500 Mbps. As this processing would occur in the external receiver, the added complexity is not burdensome. For the downlink, data rates are moderate, below 100 Mbps, and equalization should not be necessary in the implant. The maximum data rate and the BER performance are plotted for this link in Fig. 4.8d.

We use off-line process to emulate the external hardware for uplink detection, and the implanted receiver for the downlink, yielding very good sensitivity. We estimate the required transmit power to attain 0.001 BER with less ideal sensitivities, i.e., with a hardware receiver. The average of the transmitted power is calculated for different receiver sensitivities and is presented in Table 4.1. These values are calculated at 500 Mbps for the backward link and 100 Mbps for the forward link.

In section 4.2.4 we found the maximum safe transmit power was 8 dBm for the uplink and 9.5 dBm for the downlink. Therefore for the 100 Mb/s downlink we can achieve .001 BER with any of the receiver sensitivities examined. For the 500 Mb/s uplink we are more limited. For BPSK and DPSK a receiver sensitivity of -40 dBm is required. For OOK greater sensitivity would be required.

To reach our BER target for OOK with -40 dBm receiver sensitivity, we can place more power in lower frequency than 7 GHz and try to limit the spectrum of the optimized pulse (to a subband of 3.1-7 GHz) to increase the power efficiency and improve BER. Another solution is to reduce the data rate below 500 Mb/s. In other words, to keep the average power constant while the energy per bit is increased, the data rate must be reduced.

Table 4.1: Average transmitted power at .001 BER for different receiver sensitivities for 500 Mb/s uplink and 100 Mb/s downlink

Receiver Sensitivity		-67 dBm	-40 dBm	-30 dBm	-15 dBm
UWB TX-Power (dBm)	OOK	-17.3	9.7	19.7	34.7
	BPSK	-25.6	1.4	11.4	26.4
	DPSK	-21.46	5.54	15.54	30.54
Receiver Sensitivity		-47 dBm	-40 dBm	-30 dBm	-15 dBm
2.4 GHz-link TX-Power (dBm)	OOK	- 25.7	-18.7	-8.7	6.3

4.6 Conclusion

Designing a reliable wireless high speed data link in the presence of lossy biological tissues is a challenging task. We proposed a wireless communications architecture for implanted systems that simultaneously stimulate neurons and record neural responses. The proposed full-duplex dual-band transceiver configuration avoids using a circulator or a diplexer and includes only one data link which makes the implanted integrated transceiver more compact and power efficient. This architecture supports large numbers of electrodes (>500), providing 100 Mb/s for the downlink of stimulation signals, and Gb/s for the uplink neural recordings.

We presented an ex-vivo experiment using discrete components achieving Gb/s uplink rates. The BER performance of BPSK, OOK and DPSK were investigated with the 5th derivative of a Gaussian pulse as the uplink UWB waveform. The BER performance of OOK was examined for the downlink. A receiver sensitivity of -40 dBm is required for BPSK and DPSK to achieve BER of 10^{-3} at 500 Mbps for the uplink. For the OOK downlink at 100 Mbps a receiver sensitivity of 15 dBm is sufficient.

Chapter 5

A Fully Integrated Full-Duplex High Speed Transceiver for Multi-Sites Stimulating and Recording Neural Implants

Abstract

In this chapter, published in [J4], we present circuit level design of the proposed full-duplex architecture presented in the previous chapter. The transmitter (TX) and receiver (RX) share a single antenna to reduce implant size and complexity. The TX uses impulse radio ultra-wide band (IR-UWB) based on an edge combining approach, and the RX uses a novel 2.4 GHz on-off keying (OOK) receiver. Proper isolation (>20 dB) between the TX and RX path is implemented 1) by shaping the transmitted pulses to fall within the unregulated UWB spectrum (3.1-7 GHz), and 2) by space-efficient filtering (avoiding a circulator or diplexer) of the downlink OOK spectrum in the RX low-noise amplifier. The UWB 3.1-7 GHz transmitter can use either OOK or binary phase shift keying (BPSK) modulation schemes. The proposed full-duplex transceiver (FDT) provides dual band 500 Mbps TX uplink data rate and 100 Mbps RX downlink data rate, and it is fully integrated into standard TSMC 0.18 μm CMOS within a total size of 0.485 mm^2. The total measured power consumption is 10.4 mW in full duplex mode (5 mW at 100 Mbps for RX, and 5.4 mW at 500 Mbps or 10.8 pJ/bit for TX).

5.1 Introduction

In this chapter the main contribution is:

- Circuit level implementation of a power efficient UWB pulse shaper on CMOS technology.

In recent years, several neural recording and stimulating systems have been developed to provide a wireless neural interface [3, 81] to the brain. Nevertheless, these devices are difficult to commercialize in part due to lack of 1) a straightforward design to support the required functionalities, 2) sufficient miniaturization, and 3) a reliable low-power high data rate interface between implants and external devices.

A high data rate wireless interface is the key for addressing the challenges and requirements of next generation brain interfacing technology. Recently, the development of high-density neural probes ($>$ 500 sites) using standard microelectronic technology has opened up new opportunities for high-resolution mapping of brain functions [82]. High-resolution visual prosthetic systems have been designed as well for stimulating the retina from as much as 256 sites [83]. Furthermore, a new class of neuroprosthetic devices has recently been introduced to interact with neural tissues in two ways (stimulation and recording). Such bidirectional systems are significant as they establish a closed-loop connection between the brain and a prosthetic device, leading to the restoration of broken neural connections or to a significant improvement of several therapies against chronic neural diseases [84]. As we mentioned in Chapter 4, conventionally, separated data transmission links have been used for forward and backward telemetry in such implantable systems. A third and seperate link is typically used to transmit power through inductive coupling [10, 63]. Therefore, as many as three separate wireless links are often included for communicating and powering up the implanted device. Some attempts have been made to decrease the number of links for power and data transmissions. Inductive links have been utilized either for forward and backward telemetry or combining both into the same link, providing data rates on the order of a few Mbps [10]. Such strategies are prone to increased complexity and interference because of the mutual inductance with the power link. Moreover, having three separate (independent) links complicates miniaturization of the implantable devices [10, 63].

Attempts have been made to combine the forward or the backward telemetry link with the power transmission link by modulating the power carrier signal with forward/backward data [85, 86]. However, such approaches decrease the efficiency of the power transmission link and confine transmissions to low data rates. On the other hand, recent implementations of inductive power links utilize multicoil resonance-based structure enabling higher power transfer efficiency and higher power delivery across longer distances [87, 88]. Resonance-based power links inhibit frequency and phase variations of the transferred signal because of the high quality resonators located between the TX and RX coils. Therefore, frequency shift keying (FSK) and phase shift keying (PSK) modulations cannot be utilized for transferring data by the resonance-based power links. Although amplitude shift keying (ASK) modulation of the

carrier signal has been demonstrated for transferring data within a resonance-based power link, resistance against fast amplitude variation yields low data rates [89, 90]. In general, the reliability of the modulated resonance-based link is worse than conventional 2-coil inductive links, as it experiences lower power transfer efficiency and more variability of power delivery.

In this chapter, we propose an implantable full duplex RF transceiver enabling high-speed bidirectional data transmission. The chapter is organized as follows; section 5.2 presents an overview of the principle of the proposed data interference. Section 5.3 presents the full-duplex transceiver circuit design. The full-duplex transceiver experimental results obtained with the fabricated integrated circuit are presented in section 5.4. Finally, conclusions are drawn in section 5.5.

5.2 System overview

The number of stimulating and/or recording electrodes included in brain machine interface (BMI) systems is constantly increasing in order to provide high resolution, and enhancing our understanding of brain functions. This number is expected to soon reach one thousand as indicated by recent trends [91,92].The uplink data rate requirement for 1000 probes easily reaches 500 Mbps assuming a 40 ksps sampling rate $\times$ 12 bits of resolution per sample + 5% overhead = 504 Mbps. The required downlink data rate is estimated to 4 words per biphasic pulse $\times$ 25 bits/word $\times$ 1000 channels $\times$ 400 refresh/s = 40 Mbps [83,85]. Therefore, a high data rate wireless interface design is the key for implementing BMI systems. Figure 5.1 presents a block diagram of the proposed full duplex data transceiver, which enables simultaneous transmission and reception of data over a unique RF link using the same antenna (to decreases the size of the implanted device). Conventionally, passive circulators or duplexers have been utilized for implementing full-duplex transceivers [93]. Such multi-port waveguides are composed of magnetized ferrite materials that can route signals from the transmitter to the antenna, and from the antenna to the receiver, without allowing signals to pass directly from transmitter to receiver. In CMOS technology, active circulators are used instead of passive ones as CMOS is incompatible with magnetized ferrite material structures. Active circulators, typically composed of amplifiers and a power divider/combiner to form an active quasi-circulator module, attenuate the signal by at least 3 dB [69]. Moreover, such components are bulky and power hungry. A conventional strategy for implementing a full-duplex transceiver without using an active circulator is to employ two sharp band-pass filters to separate the transmit and receive frequency bands [69, 93]. These two frequency bands must be very close to be covered by the same antenna. However, having two dedicated high-order filters has drawbacks: 1) it is area consuming, 2) it attenuates the passing signal, and 3) it increases the noise figure of the receiver. Our proposed design separates the transmit and receive band by carefully shaping the transmitted signal, and filtering the received signal directly in the low-noise amplifier (LNA) using cascode transistors with passive matching filters. The block diagram of the proposed

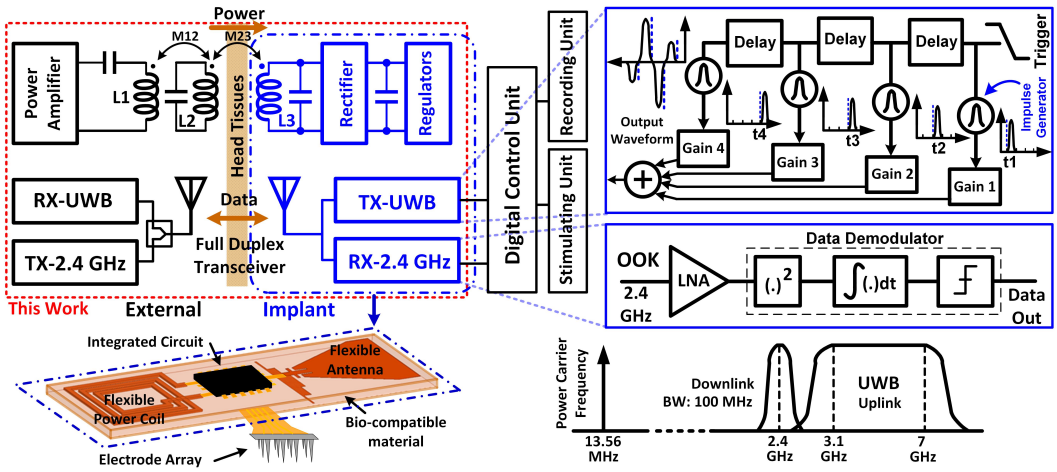

Figure 5.1: Block diagram of an implantable neural recording and stimulating device including an inductive power link and the proposed full duplex transceiver.

wireless interface is presented in Fig. 5.1. This figure shows the block diagrams of the data and power links, and all integrated building blocks of the Full-Duplex Transceiver (FDT). The proposed integrated FDT design is small and low-power, which makes it suitable for implantable applications. UWB 3.1-7 GHz and 2.4 GHz IMS bands are unlicensed bands readily available for use in low-power biomedical applications.

The proposed full duplex transceiver includes a 2.4 GHz on-chip OOK receiver and a UWB 3.1-7 GHz transmitter supporting both OOK and BPSK modulations. A circuit schematic of the FDT is shown in Fig. 5.2. The 2.4 GHz receiver is designed to support wireless downlink telemetry for neural stimulation applications, and the 3.1-7 GHz UWB transmitter is designed to support wireless uplink telemetry of high-density neural recording systems presenting very high channel counts. Since both the receiver and the transmitter use the same antenna and communicate simultaneously into different frequency bands for this application, our solution decreases design complexity, decreases the total size of the implanted device, decreases interference between the up and down links, and eases the implementation of the implanted system.

5.3 Full-Duplex Transceiver Design

The design of a fully integrated implantable full-duplex transceiver must minimize the power consumption and size of the transceiver. Implantable BMI systems, including high-density neural recording/stimulating probes, require a wireless transceiver supporting simultaneously thousands of stimulation and recording channels. The high-performance, implantable transceiver must support a high data rate uplink (body to external) and a moderate data rate downlink (external to body). Our proposed transceiver uses the UWB band (3.1-7 GHz) for the uplink,

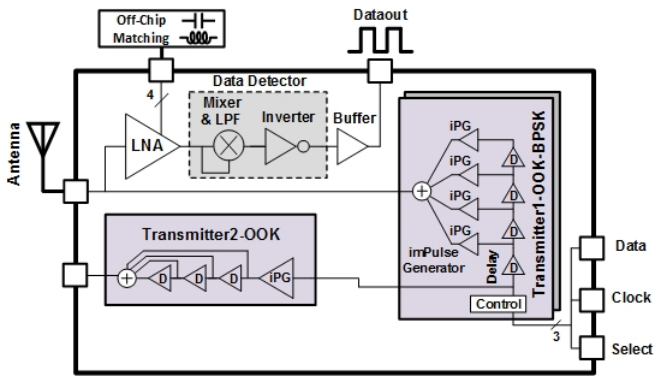

Figure 5.2: The integrated circuit building blocks of the proposed implantable wireless interface consists of a new full duplex data transceiver.

and the 2.4-2.5 GHz IMS band for the downlink. Since regulatory agencies impose a limit on the total radiated power for these unlicensed bands, the transmitter and receiver must be designed to work with reduced power levels. Our pulse shaping approach for the UWB band has four main advantages: 1) power efficient exploitation of the FCC mask, 2) isolation from the downlink that enables full-duplex operation, 3) avoidance of a circulator or a duplexer which reduces loss, power and size, and 4) concentration of power in the lower portion of the UWB band where the biological channel imposes less loss [51].

5.3.1 UWB Transmitter Design

A carrierless, edge-combining impulse UWB transmitter topology offers a simple and low-power circuit implementation [67, 94] as it avoids the need for an up conversion mixer, whose CMOS implementation is known to be power hungry [3, 14, 77]. While small in size, it can reach high data rate. Both BPSK and OOK modulation schemes can be supported with this design, offering flexibility in trading off power consumption, and desired bit error rate (BER) performance [45]. The UWB pulses are shape by adjusting the amplitude and the time duration of the 5th derivatives of a Gaussian pulse generated by a customized circuit inside the transmitter, as shown in Fig. 5.3. Such a design yields a simple transmitter, reducing the die size compared to traditional methods using a high-pass filter for shaping [3, 95]. OOK and BPSK are easily supported. The UWB transmitter circuit uses regular CMOS logic gates, such as inverters and NORs, and NMOS transistors, which sum and amplify the UWB impulses as shown in Fig. 5.3a. This design provides a high date while the size and power consumption are low. The UWB pulse is generated by summing several time-shifted glitch pulses. Four inverter-based delay lines shift the generated pulses. The four shifted impulses are output via transistors M1-M4, to form the required UWB signal data transmission. OOK modulation is produced when only the top half of the circuit is active. For BPSK modulation, the same circuit with a different output configuration (bottom half of the circuit depicted in Fig. 5.3a)

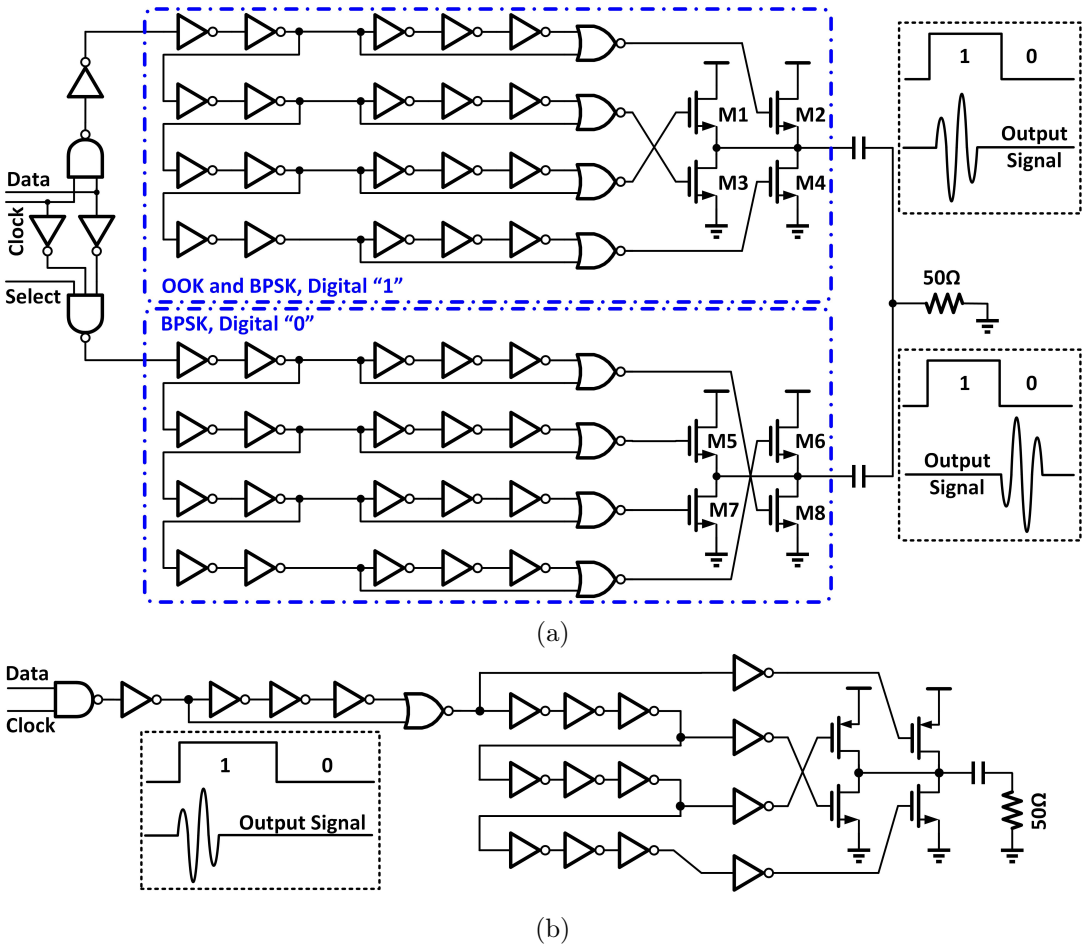

Figure 5.3: Up-link a) transmitter circuit enabling to generate UWB signal for transmitting data using OOK and BPSK modulations, and b) size and power efficient transmitter circuit enabling to produce OOK signal.

produces impulses with a 180° phase difference using the top and bottom half circuits. Digital "1" are produced by the top circuit, while digital "0", which corresponds to the 180°-phase shifted impulses, are produced by the bottom circuit. The performance obtained with both modulation schemes are compared in section 5.4. The transmitter presented in Fig. 5.3b is designed and fabricated to limit transmitter size and power consumption and supports OOK modulation only. One impulse is generated and shifted by a delay line, giving less shaping flexibility than the design of Fig. 5.3a. The shifted impulse is applied to the output transistors to produce the UWB signal.

5.3.2 2.4-GHz Receiver Design

The block diagram of the proposed 2.4 GHz OOK receiver is shown in Fig. 5.2. The input signal is amplified by the low noise amplifier (LNA), and then down-converted to baseband, similarly to the low-power system reported in [96]. The schematic of the receiver is shown

in Fig. 5.4, consisting of a common source (CS) LNA, a self-mixed down conversion mixer and an inverter. The LNA uses a cascode CS amplifier, including a CS transistor (M1) and a cascode (M2) transistor. The cascode transistor is used to increase the output impedance and the reverse isolation of the amplifier. The proposed topology uses a transistor connected

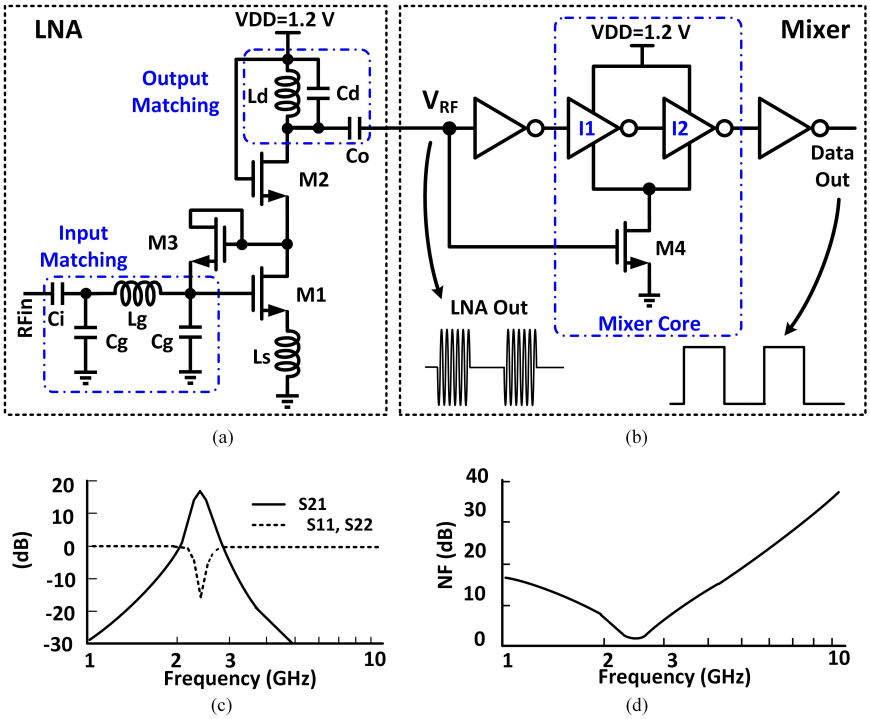

Figure 5.4: Schematic of the downlink 2.4 GHz receiver front-end which includes a low noise amplifier and a mixer based on current starving. The simulated gain (S21), input matching (S11), output matching (S22), and noise figure (NF) of the LNA are shown.

in a shunt-shunt feedback topology (M3), which separates the design of the voltage gain from the design of the input impedance [97]. Additionally, this feedback transistor provides proper bias voltage at the gate of input transistor (M1). Figure 5.4 provides simulation results for the gain, the noise figure and the input-output matching parameters of the LNA.

The mixer design schematic shown in Fig. 5.4, is based on current-starved inverters. In the mixer circuitry, inverters I1 and I2, and the NMOS transistor M4 form the core of the current-starved mixer. In contrast with conventional mixers [96, 97], this structure is resistor-less and plays the role of a lossy integrator that is used as a low-pass filter. This topology benefits from circuit design simplicity. Conventional mixer circuitries use two load branches that are periodically switched by a local oscillator (LO) with a 180° phase difference. In this design, the inverters are used both as loads and switches. Thus, the output of the first branch becomes the input of the second branch, which produces the required phase difference (180°). This circuit down-converts the signal to baseband, filters it, and subsequently boosts the signal to proper

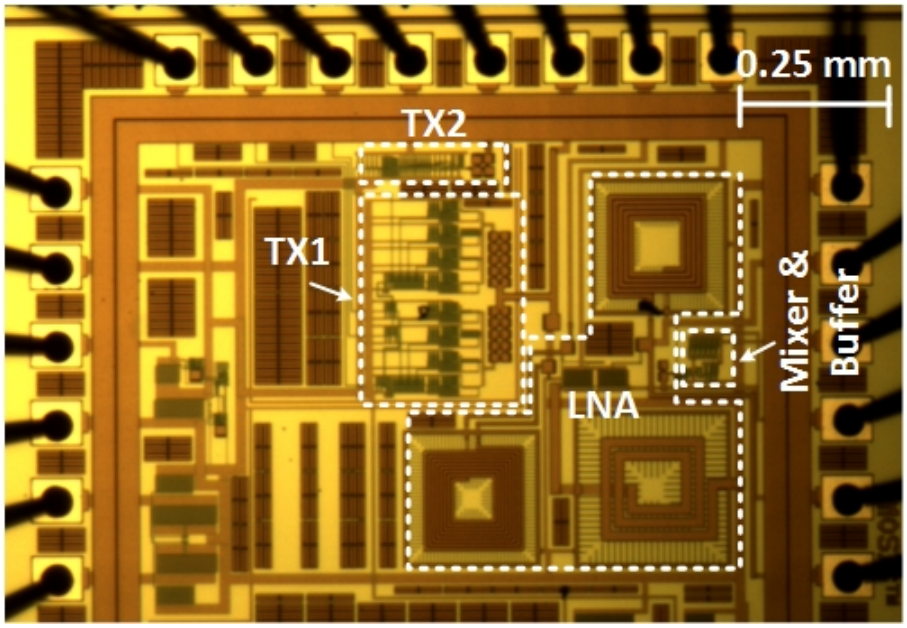

(a)

Figure 5.5: The chip micrograph of the proposed full duplex transceiver fabricated in a TSMC 0.18 μm CMOS technology, with a total die size of 1×0.8 mm^2.

digital levels using an inverter. Figure 5.4 shows the simulated frequency response of the LNA. As can be seen, input signals at frequencies above 3 GHz are filtered out by the LNA. Thus, as will be shown in section 5.4, by allocating the transmitted signal power between 5 and 6 GHz, and by filtering such signal directly at the input of the LNA, the transmitted signal is efficiently attenuated by more than 30 dB by the LNA.

5.4 Full-Duplex Transceiver Measurement Results

Figure 5.5 shows a chip micrograph of the proposed full duplex transceiver fabricated in a TSMC 0.18 μm CMOS technology including the 2.4-GHz receiver (LNA, mixer and an output buffer) and the UWB transmitters (TX1 and TX2). The receiver size is 0.375 mm^2. The transmitter sizes is 0.1 mm^2 and 0.01 mm^2 for TX1 and TX2, respectively.

To verify the functionality of the proposed full duplex transceiver, the implantable transceiver was fabricated in TSMC 0.18 μm CMOS technology and tested in full-duplex mode. Discrete components and instruments were utilized as an external system to send and retrieve data from the FDT. Figure 5.6a and 5.6b represent the measurement setup block diagram and experimental setup employed for characterizing the full-duplex data link. On the external controller side, a 3 dB power divider is utilized between two summation ports, which present an isolation of 22 dB. The UWB discrete receiver amplifies the received signal using an ultra-wideband LNA with a 27 dB flat gain and 4 dB noise figure. This signal is captured by a real-

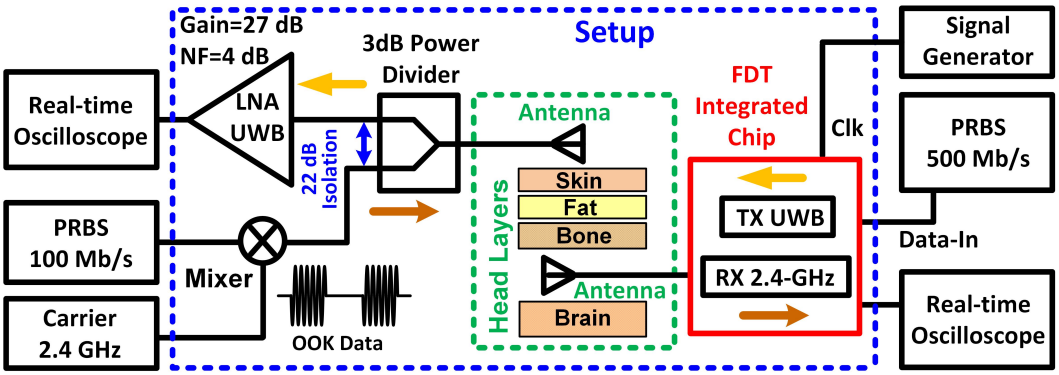

(a)

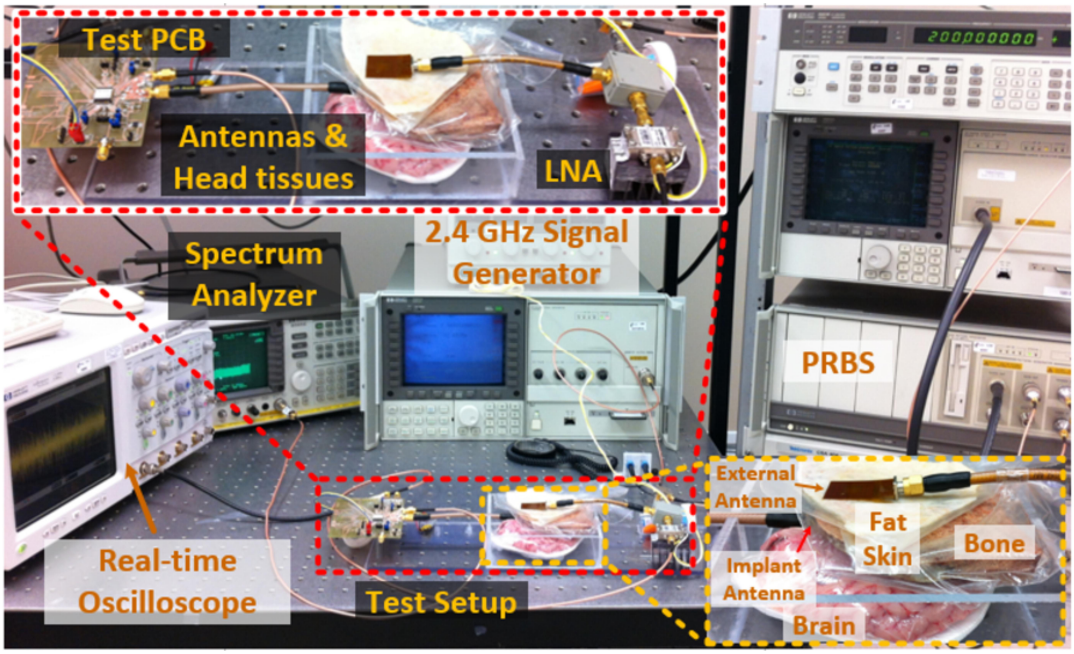

(b)

Figure 5.6: a) Experimental setup block diagram showing the required equipment, and b) the experimental measurement setup employed for characterizing the full-duplex data link.

time oscilloscope to be analyzed off-line in MATLAB. The 2.4 GHz transmitter is implemented by a mixer, which mixes the output of a pseudorandom binary sequence (PRBS) with a 2.4 GHz sinusoidal signal source to generate a random OOK signal. On the implanted side (Fig. 5.6a), the integrated transmitter circuit generates UWB pulses, according to the selected modulation type (OOK or BPSK). The transmitter pseudorandom input data sequence is generated by an external PRBS generator. The signal-to-noise ratio (SNR) of the UWB transceiver is measured on the receiver side. The 2.4 GHz integrated receiver amplifies the received OOK signal and digitizes it. The digital data is captured at the output of the receiver by a real-time oscilloscope, and analyzed offline in MATLAB to calculate the BER. The biological tissues of

the head are emulated using fresh animal tissue layers: skin (1 mm), fat (1 mm), bone (4 mm), and brain (30 mm). These tissue thicknesses are chosen to mimic typical human head tissues [21]. To emulate a complete channel, an implanted antenna and an external antenna [51] are connected to the other equipment by 50 Ω SMA connectors. Such a channel was characterized previously in [51], showing that as expected, the insertion loss of the channel increases with frequency. At low frequencies the channel experiences no distortion, while at high frequencies inter-symbol interference may occur (leading to performance deterioration). Lower loss is expected in the biological channel at lower frequency, improving BER. So, the efficiency of the link is increased by putting more power of the transmitted pulse at lower frequencies by pulse shaping. The spectrum of the transmitted UWB signal must be located in the desired frequency band of 3.1-7 GHz to avoid coupling into the LNA of the 2.4-GHz receiver. To capture the spectrum of the UWB signal, the output of the transmitter is measured using a real-time oscilloscope and Fourier transformed. The results are presented in Fig. 5.4-5.7. As shown the Fig. 5.7a and 5.7b, the spectrums of the UWB signals are between 3.1 and 7 GHz for both implemented transmitters (TX1 and TX2, respectively). As can be seen in Fig. 5.7, there is a isolation of more than 20 dB between downlink and uplink. The proposed UWB transmitter uses edge-combining (based on short pulse delays) to avoid using a mixer, an oscillator and a band pass filter, thus lowering power consumption [67, 75]. A PRBS sequence is used for testing the transmitters. At the external receiver of the uplink, the data is captured by a real-time oscilloscope to find BER at 500 Mbps. Figure 5.8a shows the measured output of the fabricated UWB transmitters TX1 and TX2. As described previously, when in OOK mode, the transmitters transmit impulses only when there are digital "1" to transmit, otherwise no power is transmitted. For BPSK mode, the transmitter produces impulses for digital "0" and "1". A digital "0" is represented by 180°-phase shifted impulse, compared to a digital "1". The measured power consumption of both fabricated UWB transmitters are 5.4 mW and 3.5 mW for TX1 and TX2, respectively for OOK at 500 Mbps. Transmitter TX1 consumes 11 mW in BPSK mode at 500 Mbps. These measurements use antennas with 50 Ω matched impedance [51]. Therefore, the input of the LNA is matched with a 50 Ω impedance at 2.4 GHz. To reach good input and output impedance matching, an off-chip matching network (capacitors and inductors) is used in the design of the 2.4 GHz receiver. On the implanted side, matching the LNA input impedance with a 50 Ω characteristic impedance, requires series inductance and capacitance. A parallel LC tank is utilized at the output stage of the LNA (Fig. 5.4) in order to obtain the desired gain, and to achieve proper impedance matching around 2.45 GHz. The three required on-chip inductors of the LNA are designed using HFSS, a finite element solver, and then imported into Cadence Virtuoso for completing the layout of the chip. The TSMC 0.18 μm CMOS layer specifications are used for simulating the inductors inside HFSS. The inductors are designed for maximizing the quality factors while achieving small size according to the methodology described in [98]. A minimum 50 μm gap is introduced between the inductors and other circuit components to decrease electromagnetic

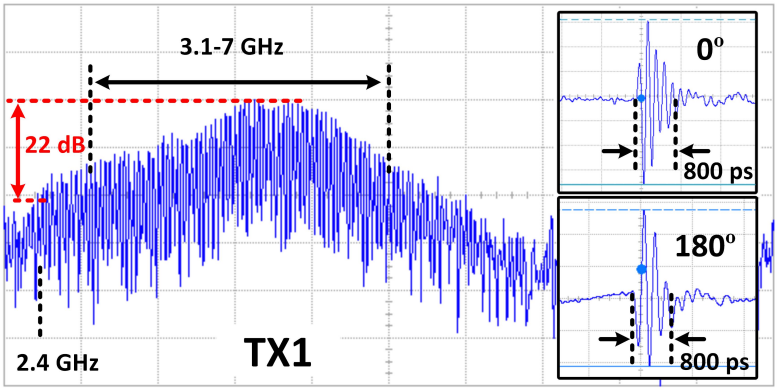

(a)

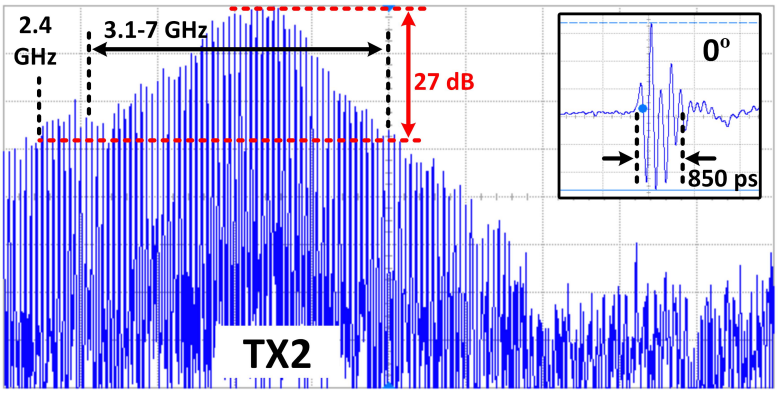

(b)

Figure 5.7: The measured spectrums of the UWB output signals for a) transmitter TX1, and b) transmitter TX2.

field interference. A top metal layer (Metal 6) is utilized to implement the inductors and a polysilicon layer with a striped configuration is put under the inductors for increasing their quality factors. Note that the polysilicon layer is connected to the ground. Conventionally, performing OOK demodulation consists of self-mixing the output signal of the LNA inside the mixer, and passing the resulting signal throughout a low-pass filter. Then, the resulting signal is compared to a reference voltage in order to detect the received data. The proposed architecture is very effective since the mixer down converts the signal to the baseband, and filters it simultaneously. Therefore, this topology avoids the need for any additional circuits, such as filters or comparators. Only a simple inverter is needed at the output to boost the signal to suitable digital levels. To measure the BER performance of the UWB uplink and the 2.4 GHz downlink, length 2^{15}-1 PRBS sequences are used to generate 100,000 bits. After acquiring the output data sequences, offline processing is utilized to calculate the BER performance [45]. For the UWB link, no errors were detected at the rate of 500 Mbps OOK and BPSK modulations, hence BER is below 0.001 (with probability of .9 [99]). Figure 5.8b

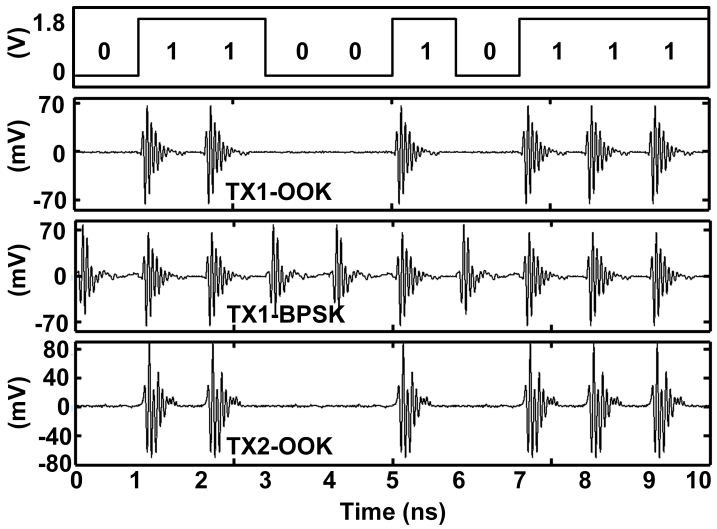

(a)

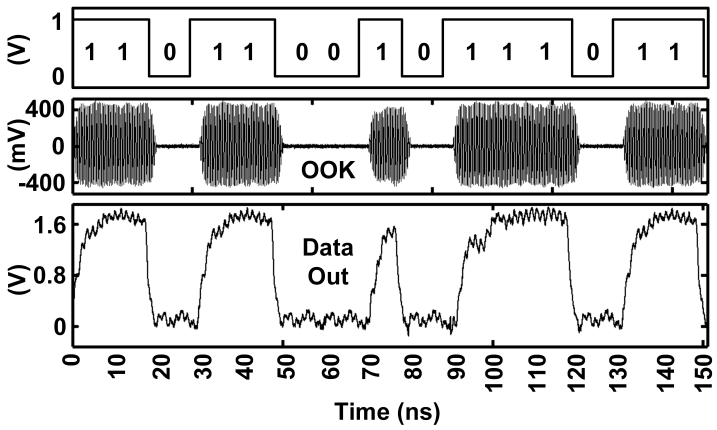

(b)

Figure 5.8: Measurement results of the full duplex transceiver including a) the transmitted UWB signals using OOK and BPSK modulation schemes (TX1 and TX2) at a rate of 500 Mbps, and b) the generated 2.4 GHz OOK signal and detected data at a rate of 100 Mbps.

shows the measurements for the 2.4-GHz link for downlink transmission. These results include the transmitted OOK signal (produced by mixing a 2.4 GHz carrier signal with a PRBS data sequence) and the digitized data at a rate of 100 Mbps in the integrated receiver. The output signals of the 2.4 GHz receiver are captured using a real-time oscilloscope. As with the UWB setup, the BER was measure. No errors were observed for the 2.4 GHz downlink using OOK modulation at a rate of 100 Mbps, hence BER is also below 0.001 (with probability of .9 [99]). The gain of the LNA was measured to be 13.7 dB using a spectrum analyzer. The measured noise figure of the LNA is 2.6 dB. The power consumption of the receiver is measured at 5 mW (4 mW for the LNA and 1 mW for the mixer). To capture the output data of the 2.4-GHz receiver off-chip with test equipment, a chain of inverters is utilized as a buffer which properly charges and discharges the output pad of the chip at the rate of 100 Mbps. The

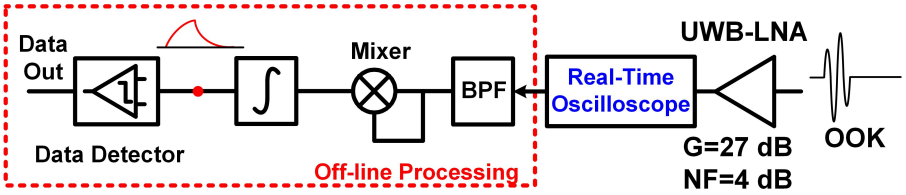

(a)

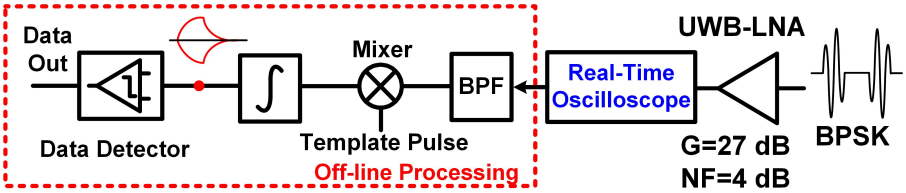

(b)

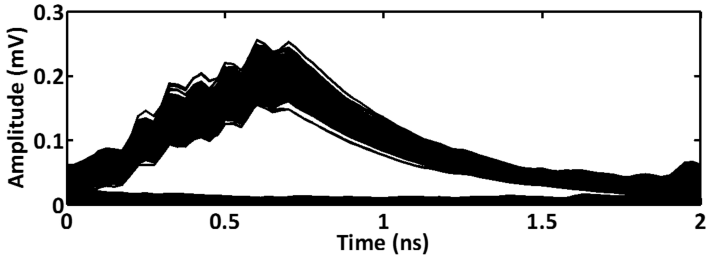

(c)

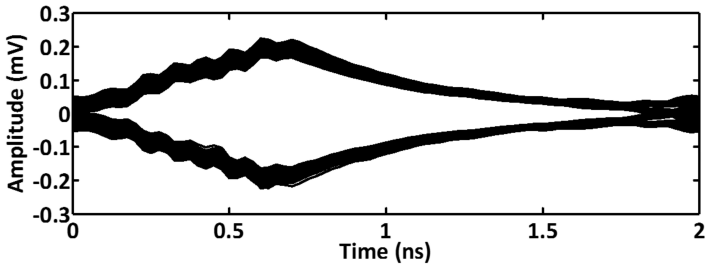

(d)

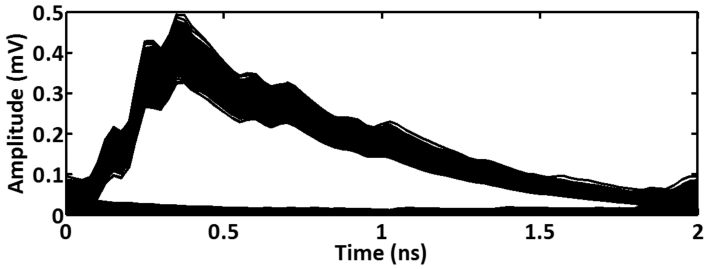

(e)

Figure 5.9: Block diagram of the UWB receivers (RX-UWB) for a) OOK, and b) BPSK modulations. The measured eye diagrams for the transmitters TX1 in c) OOK mode, d) BPSK mode, and e) TX2 in OOK mode.

power consumption of the buffer is of 40 mW at 100 Mbps. The buffer is not required when the receiver is connected to the on-chip digital control unit.

Figure 5.9a and 5.9b show the block diagram of the external receiver systems for OOK and BPSK modulations, respectively. The external received signal is amplified by a UWB-LNA and captured using a real-time oscilloscope. The mixing, integrating and detecting tasks of the captured signals are performed offline in MATLAB. Figure 5.9c to 5.9e present the eye diagrams of the measured signals for TX1-OOK, TX1-BPSK and TX2-OOK modes, respectively. As shown in these curves, the captured data are open enough to be detected by comparing it with a threshold voltage.

Figure 5.10 shows the power consumption of the transmitters for different modulation modes as a function of data rate. The digital circuit of the transmitter does not consume power when the transmitter clock is disabled. So, the power consumption of the transmitters depends on the data rate, therefore, as shown in the Fig. 5.10, there is a linear relationship between the data rate and the power consumption, which makes this design highly flexible for accommodating several applications with different data rates.

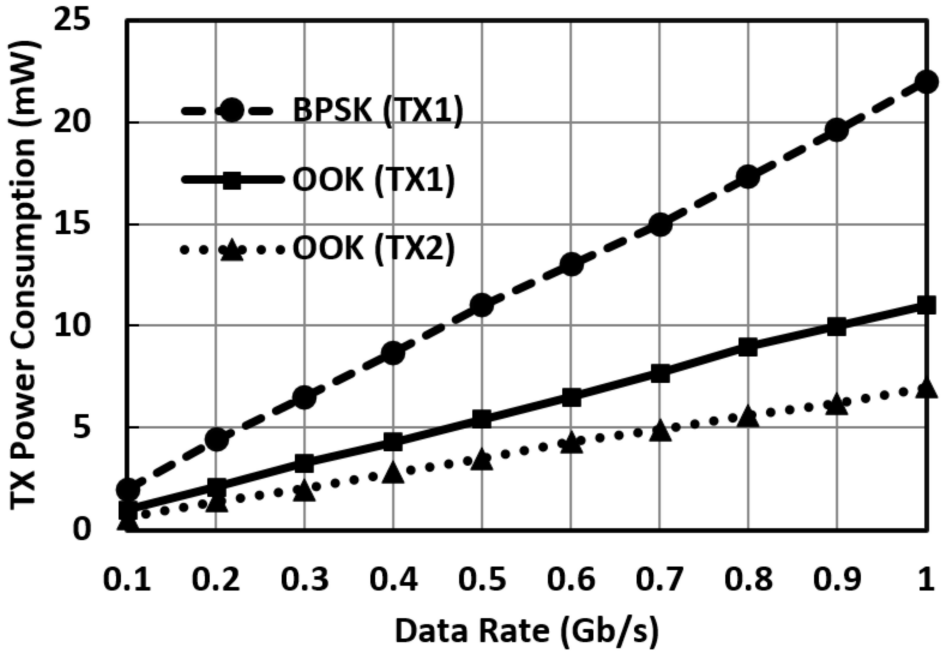

Figure 5.10: The measured power consumption of the UWB transmitters for OOK and BPSK modulations as a function of data rate.

The performances of the designed UWB transmitters TX1/TX2 and 2.4 GHz receiver are compared with previously published works which are presented in Table 5.1. The main novelty of the presented work is the full-duplex configuration, which provides bidirectional data transmission across one RF link. In addition our results show improved data rate and power

Table 5.1: Comparison of previously published data links with our approaches.

Ref., Link	Tech.	Rate(Mbps)	E.(pJ/b)	B.W.(GHz)	Modulation	Die(mm^2)	P.(mW)
[100], TX	-	48	1040	3.2/3.8	FSK	-	50
[14], TX	0.35μm	30	161.7	3-5	OOK	-	4.85
[95], TX	0.35μm	160	10	3.1-5	PPM+OOK	8.87.2	1.6
[67], TX	65nm	24	8.5	3.6-7.5	OOK	10.7	0.217
[94], TX	65nm	200	45	3.1-5	PPM	2	9
This work, TX1	0.18μm	500	10.8	3.1-7	OOK, BPSK	0.1	5.4
This work, TX2	0.18μm	500	7	3.1-7	OOK	0.01	3.5
Ref., Link	Tech.	Rate(Mbps)	f(MHz)	Modulation	Coil/Ant. size	Die(mm^2)	P.(mW)
This work, RX	0.18μm	100	2400	OOK	11 cm^2	0.375	5
[90], RX	CMOS	1	8.4	ASK	1.351.35 cm^2	-	0.1
[85], RX	1.5μm	2.5	5/10	FSK	1.30.3 cm^2	0.29	0.38
[83], RX	0.18μm	2	22	DPSK	dout=1 cm	0.520.62	5.7

consumption compared to previously published works.

5.5 Conclusion

We have presented an integrated, full-duplex transceiver to support high-density and bidirectional neural interfacing applications (high-channel count stimulating and recording). It includes a 2.4 GHz on-chip receiver with OOK modulation, and a UWB 3.1-7 GHz transmitter with selectable OOK or BPSK modulation. The implanted transceiver was fabricated in TSMC 0.18 μm CMOS technology. The uplink and downlink were characterized using biological materials emulating head tissue layers. The proposed full-duplex transceiver avoids the need for a circulator or diplexer, as in conventional systems. The full-duplex functionality is implemented by shaping the transmitted pulse. The impulse generator is based on edge-combining, to keep its spectrum inside the UWB band (3.1-7 GHz), and by matching only the 2.4 GHz input signal to the input of the LNA of the receiver. The receiver is designed for wireless downlink telemetry of neural stimulation applications at data rates up to 100 Mbps while consuming only 5 mW. The transmitter is designed for uplink telemetry of neural recording systems supporting data rate above 500 Mbps while consuming 5.4 mW.

Chapter 6

Flexible Sixteen Antenna Array for Microwave Breast Cancer Detection

Abstract

Results from this chapter were published in [J5]. Radar based microwave imaging (MI) has been widely studied for breast cancer detection in recent times. Sensing dielectric property differences of tissues over a wide frequency band has been made possible by ultra-wideband (UWB) techniques. We design single and dual-polarization antennas for wireless ultra-wideband breast cancer detection systems using an inhomogeneous multi-layer model of the human breast. Antennas made from flexible materials are more easily adapted to wearable applications. Miniaturized flexible monopole and spiral antennas on a 50 μm Kapton polyimide are designed, using a high frequency structure simulator (HFSS), to be in contact with biological breast tissues. The proposed antennas are designed to operate in a frequency range of 2–4 GHz (with reflection coefficient (S_{11}) below -10 dB). Measurements show that the flexible antennas have good impedance matching while in different positions with different curvature around the breast. Our miniaturized flexible antennas are 20 mm $\times$ 20 mm. Furthermore, two flexible conformal 4$\times$4 ultra-wideband antenna arrays (single and dual polarization), in a format similar to that of a bra, were developed for a radar-based breast cancer detection system. By using a reflector for the arrays, the penetration of the propagated EM waves from the antennas into the breast can be improved by factors of 3.3 and 2.6, respectively.

6.1 Introduction

In this chapter the main contributions are:

- Design of flexible 4$\times$4 monopole and spiral antenna arrays on a 50 μm Kapton polyimide.
- Improved the penetration of the propagated EM waves from the antennas into the breast by using a reflector.

There has been great demand for a new, non-ionizing, reliable, cost-effective, and comfortable approach for breast screening. One such possibility is using microwave imaging methods for early breast cancer screening and diagnosis, as a complementary technology to the current method of X-ray mammography [101]. Large-scale studies on ex-vivo tissues report a dielectric contrast between the normal and malignant tissues in the microwave range. This reported contrast is the basis for the hypothesis that one can form a microwave scattering map of the breast tissue, detecting the malignancy as the main scatterer [102].

There are two approaches in Microwave Imaging (MI): tomography-based and radar-based. Microwave tomography (MT) is a narrowband approach wherein the electrical profile of the breast is reconstructed by solving a nonlinear and ill-posed inverse scattering problem [103]. A microwave scattering map can be obtained from the differences in dielectric properties of the breast tissues, using radar-based imaging [104]. Employing an array (as a multi-static radar) has the advantage of avoiding the mechanical issues of a scanning antenna; thus radar-based breast cancer detection systems have been developed [105]. A multi-static system is able to provide better imaging results than a mono-static system [106] in breast cancer detection, due to the potentially higher number of signals that can be obtained for signal processing and imaging. Hence, it is necessary to build even smaller antennas, to allow more antennas to be positioned around the breast simultaneously. In this way we maintain comprehensive radiation coverage over the tissue and reduce the error associated with antenna position, and thus, improve the accuracy of the system. The image quality provided by radar-based microwave imaging techniques is affected by the number and efficiency of the receivers, the synthetic aperture of the antenna array, and the bandwidth of the probing signal. It is very important to obtain a high-performance, broad-band antenna. Typical characteristics of the antenna to be used in a radar-based imaging system are: wide impedance bandwidth, small size, repeatable and cost-effective fabrication, and ability to efficiently couple power to the breast [8].

Low frequencies provide deeper penetration (lower loss), but the higher frequencies offer better range resolution. Smaller antennas enable a higher number of antennas in the array and enhance resolution. However, there is a practical limitation in the low-frequency performance of antenna that is mainly determined by its maximum antenna dimension due to the restricted area on the breast surface [107]. The solution to this issue is of great interest for ultra-wideband (UWB) techniques [107].

Miniature antennas in contact with biological tissues have very different propagation behavior and return loss compared to those in free-space [108–111]. The characteristic impedance of biological tissues vary considerably with frequency and from tissue to tissue; thus careful antenna impedance matching is required. An antenna operating in contact with stacked layers of biological tissues in a detection system, to avoid power reflections (between tissues) caused by inhomogeneities in the breast media, should be simulated with an inhomogeneous model

to capture all phenomena during the design process. In this way, the antenna can provide as much energy as possible so that transmitted signals can be received with reasonable strengths from breast tissues.

To date, only a few small broad-band antennas for breast cancer detection have been reported [8, 106–113]. Planar printed monopole antennas have been recently considered for breast cancer imaging [106, 112, 113] due to the simple structure, broadband property, relatively small size, and ease of fabrication. However these antennas are not flexible but bulky. To date, different wearable flexible antennas have been designed for different parts of the body (except for the breast) by taking into account the effects of biological tissues for the industrial scientific and medical (ISM) and Med-Radio bands [48, 49]. In this chapter, we present a

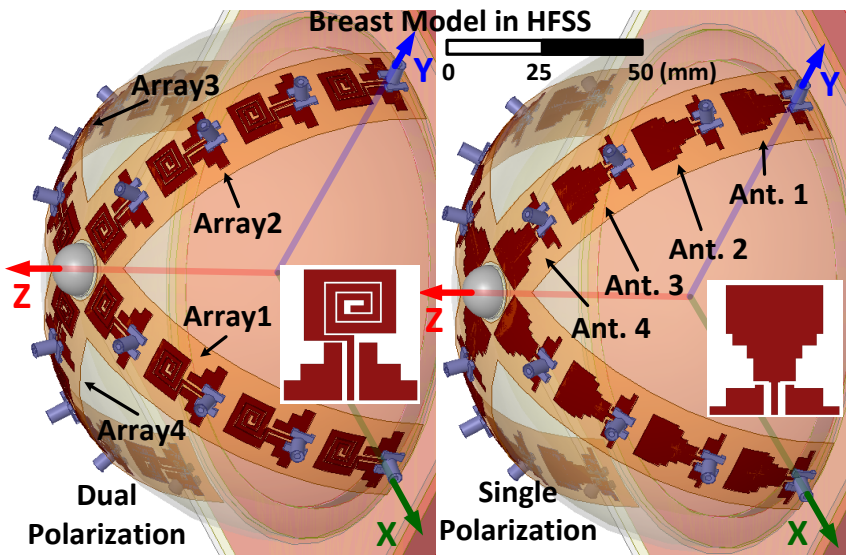

Figure 6.1: An overview of a flexible antenna array as a bra for breast cancer detection (single arm spiral and monopole antenna arrays.

flexible 4×4 monopole and single arm spiral UWB antenna array operating in the 2-4 GHz spectrum that meets bandwidth requirements of breast-cancer microwave-imaging. This work is a modified version of an existing system model [114], with the main difference of using a flexible antenna array instead of the bulky, fragile, and expensive traveling wave tapered and loaded transmission line 4×4 antenna array.

To the best of our knowledge, a flexible antenna array for breast cancer screening has not been presented in the literature to date. Use of a flexible antenna array that mimics a bra has several advantages, i.e., light weight, low cost, and ease of fabrication and installation. Sixteen UWB flexible antennas with the same structure are placed on the same substrate, to compose an antenna array that is expected to form the core of a multi-static imaging system

as shown in Fig. 6.1.

In section 6.2, we present the simulated dielectric tissues used as an inhomogeneous breast media, for 3D simulations in a high frequency structure simulator (HFSS) to capture the real behavior of the antenna propagation in proximity of the breast, and to design the flexible monopole and the single arm spiral antenna array. In section 6.3, we describe the antenna design methodology for single and dual polarization. Section 6.4 presents measurement results. Antenna array performance was measured on a phantom that is representative of real biological tissues. In section 6.5, use of a reflector is suggested to improve the penetration of the propagated EM waves into the breast. Furthermore, the maximum allowed transmitted power based on simulated Average Specific Absorption Rate (ASAR) for different positions of the antennas in the array is also discussed. Finally, conclusions are drawn in section 6.6.

6.2 Inhomogeneous Breast Modelling

The antennas must be designed taking into account the impact of the proximity to biological tissues in its near field. As we discussed in previous chapters, the breast as a communication media is modeled by a multi-layer model; that model is used to design the antenna array. The model includes skin, fat, gland, and muscle, and is shown in Fig. 6.2 [8].The simulated geometrical parameters of the breast model are presented in Table 6.1.

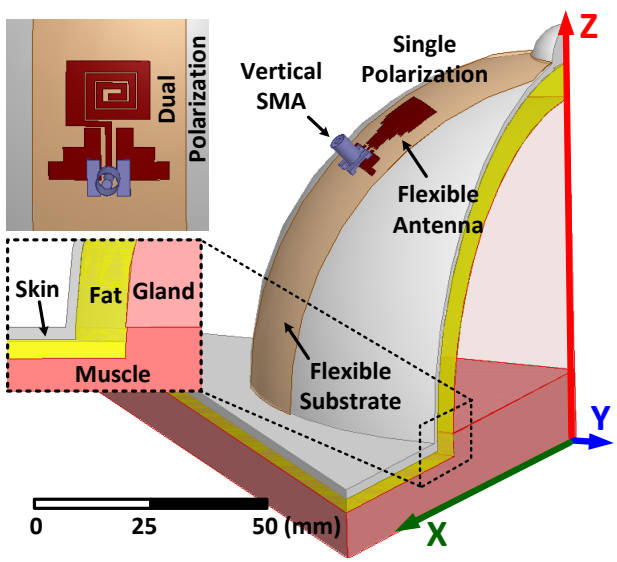

Figure 6.2: Multi-layer inhomogeneous model of the breast for designing the flexible antenna array in HFSS.

One important point, during the design of the antennas, is accommodating the variation of

Table 6.1: Characteristic of TX and RX antennas.

Tissue	Thickness(mm)	Inner radius(mm)	Outer radius(mm)	Mass Density (kg/m3)
Skin	2	68	70	1010
Fat	8	60	68	928
Gland	120	0	60	1035
Muscle	8	0	0	1040

breast tissues from person to person. After designing the antenna for the specific thicknesses and the defined electrical properties of the tissues, it should be checked while varying the thicknesses (different size of breasts) and electrical properties (∼20%) to be sure that S_{11} is still kept below -10 dB. Details of design are given in the next section.

6.3 Flexible Antenna Array

Planar monopole (single-polarization) and spiral (dual-polarization) antennas on a flexible substrate have the potential to meet the constraints of this application: 1) small footprint, 2) biocompatibility, 3) high bandwidth, and 4) light weight to be placed on the breast comfortably.

Our single-polarization and dual-polarization antennas are realized as monopole microstrip and single-arm spiral antennas respectively and are covered with a biocompatible material (Kapton polyimide). For all antennas, the feed circuit is a coplanar waveguide (CPW) transmission line having 50-Ω impedance over the 2-4 GHz frequency range.

We use 0.05 mm Kapton polyimide as the biocompatible substrate for the flexible antennas. The relative permittivity of Kapton polyimide is 3.5. For both antennas, a superstrate layer identical to their substrate layers covers the metal antenna traces. This superstrate layer completely isolated the antenna from the biological tissues making the antennas fully biocompatible.

6.3.1 Single- and Dual-Polarization Antennas

There are several UWB single polarization monopole antennas designed for breast cancer existing in the literature [106, 112, 113]. These antennas were designed on inflexible substrates that are ill adapted to the curvature of the breast. Microwave substrates to be as wearable on the breast should be biocompatible and as flexible and as soft as possible. In [56], the type of Kapton polyimide substrate used has been reported that has the two aforementioned properties. Due to the polarization selectivity of breast tissues, we are interested in a design that covers both X and Y polarizations. Although such a design is more complex, it may add information to the collected signal by enabling recording of backscattered signal of two

polarizations. We revisit the design of single and dual polarization antenna using the same methodology presented in Chapter 3. We use breast tissues by incorporating a flexible substrate to achieve a suitable antenna array for breast cancer detection. Figure 6.3 and 6.4 show the induced antenna current. In the single polarization antenna, current induced on the antenna follows a single axis of propagation. We observe that for the dual polarization antenna the current is distributed almost equally in X and Y directions.

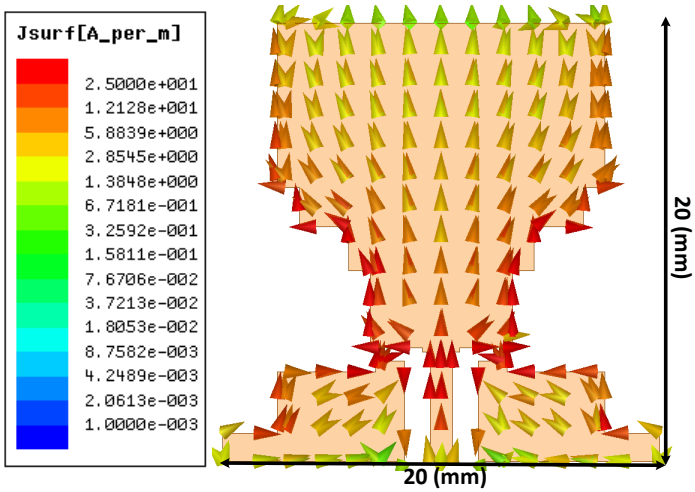

Figure 6.3: The induced current on the flexible single polarization antenna.

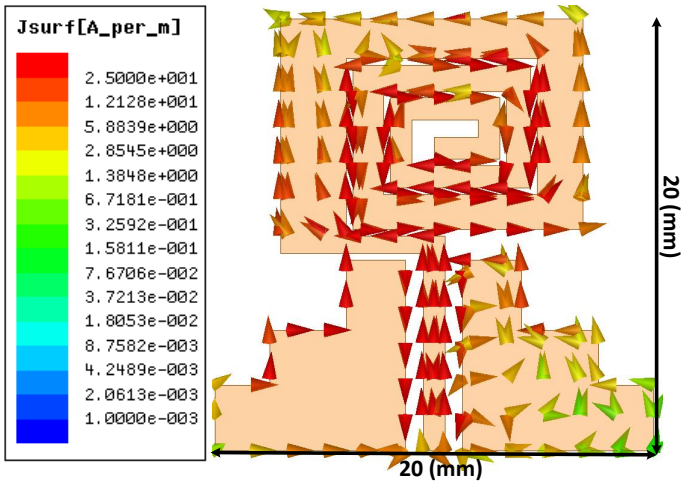

Figure 6.4: The induced current on the flexible dual polarization antenna.

6.4 Measurement Results

6.4.1 Measurement Setup

In order to verify our simulation results, we fabricated the arrays on the flexible substrate. Figure 6.5 shows the fabricated arrays which were measured on a phantom. The S_{11} of different antenna positions are measured with antenna positions on the array (1-4) shown in Fig. 6.1. The transmission coefficient, S_{21}, of the antenna pairs between antenna 3 in array 1 and antenna 1-4 in array 2 and 3 shown in Fig. 6.1, are also measured. Measurements are made using an Agilent PNA-L Network Analyzer N5232A, 300kHz - 20GHz for both single and dual polarization antennas.

6.4.2 S-parameter Results

Figure 6.6a shows the measured S_{11} of the single-polarization and Fig. 6.6b shows the measured S_{11} of the dual-polarization antennas for different positions of the antennas in the array as shown in Fig. 6.1. S_{11} results show good impedance matching (S_{11} below -10 dB) across the 2-4 GHz frequency range for each position. The results demonstrate that the flexible antenna is insensitive to bending, and thus is a good candidate for use in the array configuration.

The measured amplitude and phase of S_{21} (transfer function) between antenna 3 of array 1 and antennas 1 to 4 of array 2 and 3 for monopole antenna array (array layouts and antenna numbering shown in Fig. 6.1) are shown in Fig. 6.7a and 6.7b. The measured S_{21} results between antenna 3 of array 1 and antennas 1 to 4 of array 2 and 3 for single arm spiral antenna array are plotted in Fig. 6.7c and 6.7d. From the S_{21} results, we conclude that antennas that are further apart communicate with higher insertion loss. Additionally, because the biological tissues have higher loss in higher frequencies, the S_{21} results follow this behavior (less insertion loss in lower frequency). From the amplitude and phase behavior of each pair, we observe that the transmitted pulse at one antenna, received by another antenna undergoes a different distortion for each TX/RX antenna pair.

6.5 Improving Penetration of Propagated EM Waves Inside Breast and Maximum Allowed Transmitted Power

In this section, we show that by using a reflector for the antenna arrays, it is possible to improve penetration of propagated EM waves into the breast from the wearable antennas, which causes an improvement in power efficiency of the links between the antennas, and thus better image resolution. We also calculate the maximum power that is allowed to be sent by antennas in different positions in the array shown in Fig. 6.1, with and without use of a reflector.

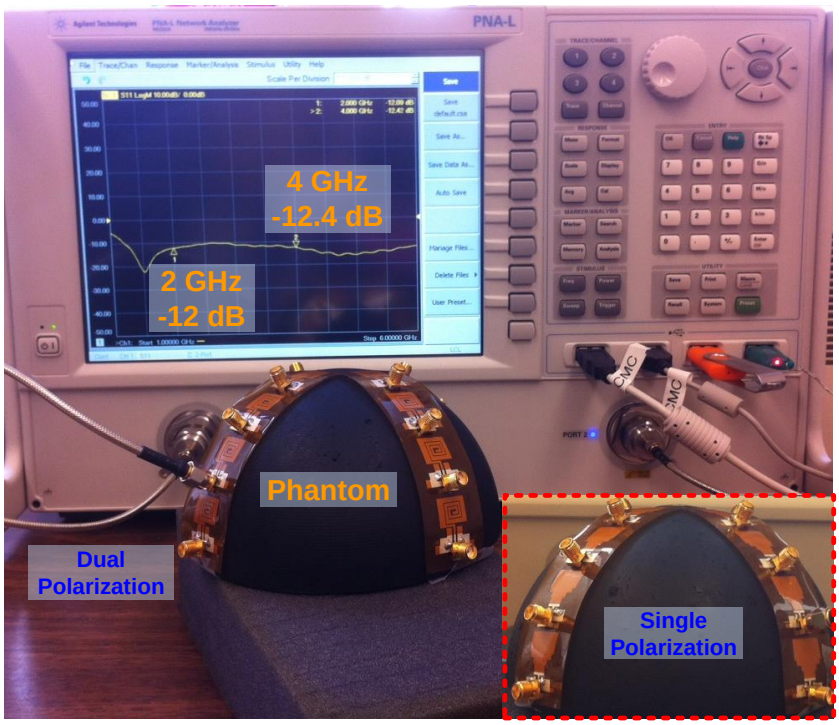

(a)

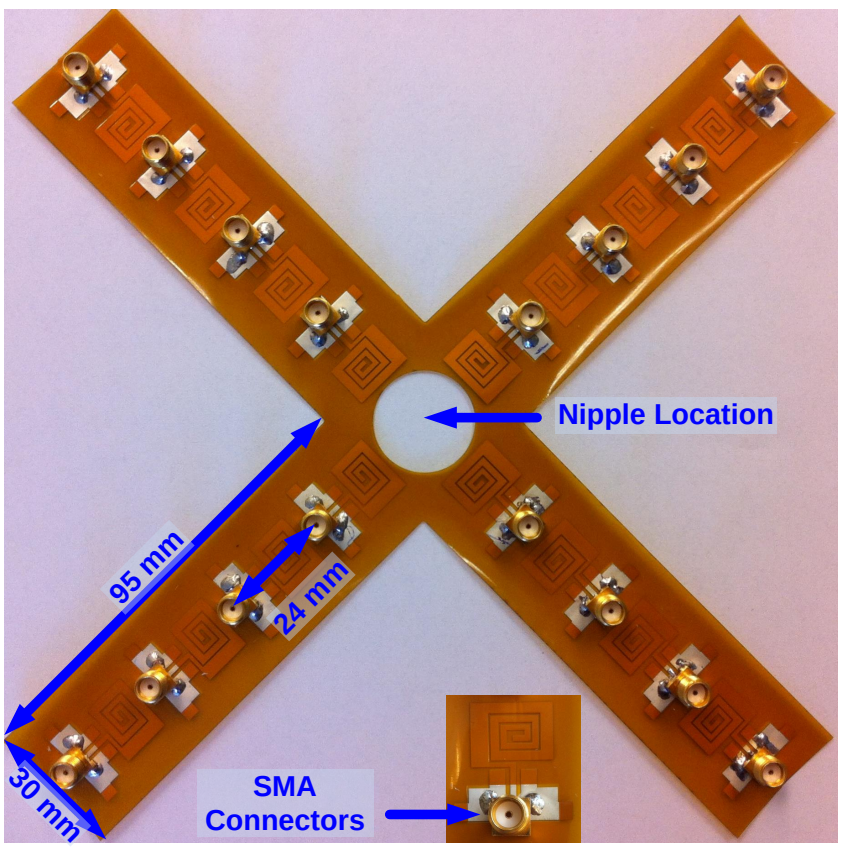

(b)

Figure 6.5: The S-parameter measurement set up a) Antenna array placed on the dielectric tissue-mimicking phantom, and b) Top view of the array, identifying the nipple location.

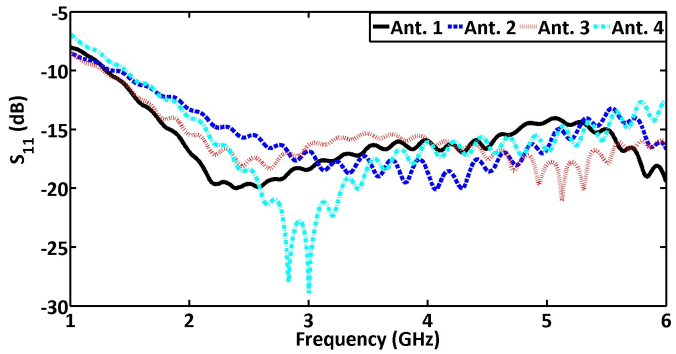

(a)

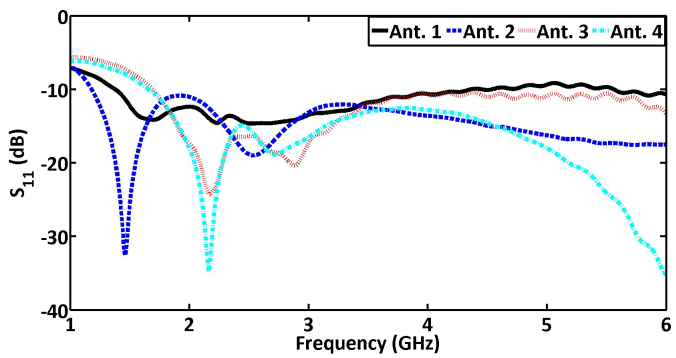

(b)

Figure 6.6: The measured S_{11} for different positions of the antennas in the array (a) monopole antenna, and (b) single arm spiral antenna.

6.5.1 Improving Penetration of Propagated EM Waves

Electromagnetic waves are used to transport information through a wireless medium or a guiding structure, from one point to the other. The quantity used to describe the power associated with an electromagnetic wave is the time average Poynting vector (average power density) [7]:

$$W_{av}(x, y, z) = 1/2 \times [E \times H^*] \tag{6.1}$$

where E and H are the peak values of instantaneous electric-field intensity (V/m) and instantaneous magnetic-field intensity (A/m), respectively.

The real part of (6.1) is averaged over the propagated power density, and the imaginary part represents the reactive (stored) power density associated with the electromagnetic fields. The real part is responsible for delivering power from one antenna to another antenna. Figure 6.8 shows the real part of the Poynting vector when antenna 4 is propagating in the Z-X plane for monopole and spiral antenna arrays. This figure shows that by using a reflector behind the antenna arrays, it is possible to improve the penetration of the propagated EM inside the breast.

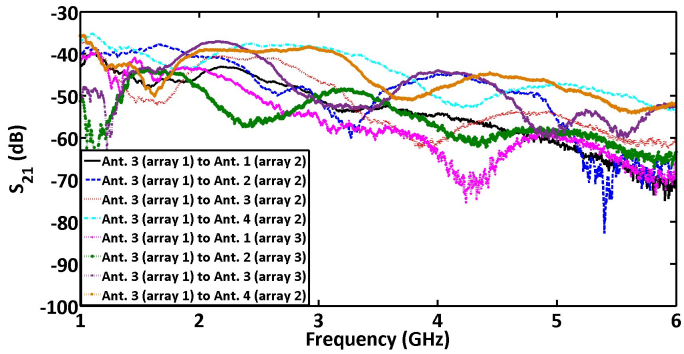

(a)

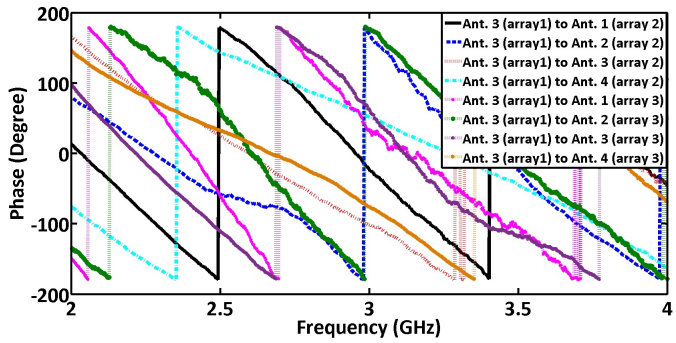

(b)

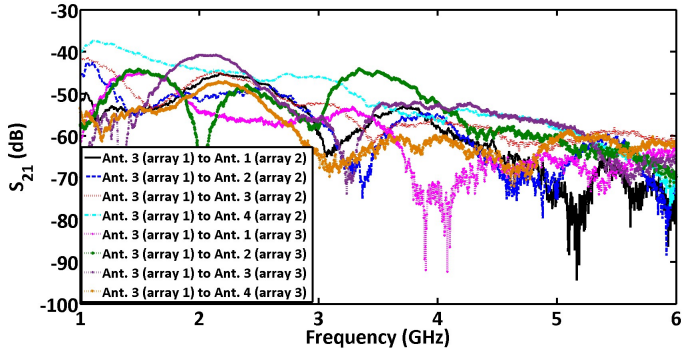

(c)

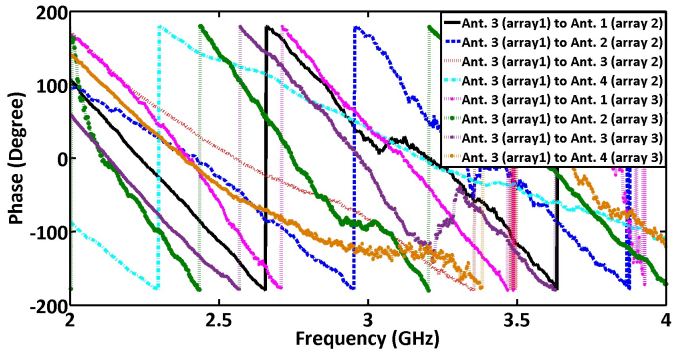

(d)

Figure 6.7: The measured S_{21} between antenna 3 of array 1 and antennas 1 to 4 of array 2 and 3 (a) amplitude for monopole antenna array, (c) phase for monopole antenna array (c) amplitude for spiral antenna array, and (d) phase for spiral antenna array.

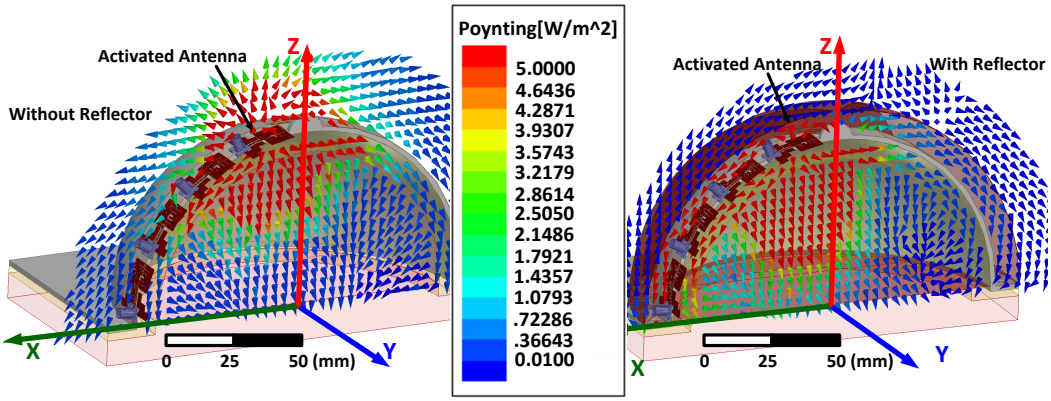

(a)

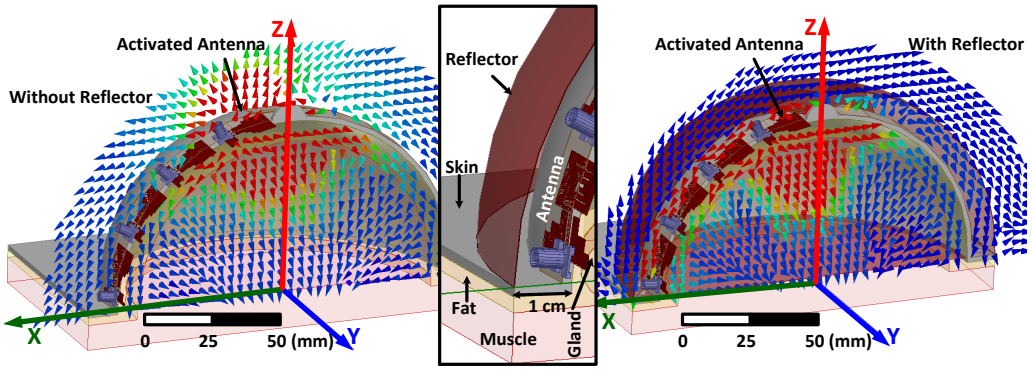

(b)

Figure 6.8: The real part of the Poynting vector propagating in the Z-X plane for antenna 4: without reflector (left side) and with reflector (right side) for a) monopole and b) spiral antenna arrays; color map applies to all cases.

The reflector should be placed far enough that it does not affect the S_{11} of the antennas. By placing the reflector further than 1 cm from the antennas, S_{11} remains unchanged. HFSS results show that for the spiral antenna using the reflector, the real part of the Poynting vector in the position of (x = 0, y = 0, and z = 0) improves by a factor of 3.3, and similarly, by a factor of 2.6 for the monopole. This significant penetration of EM waves inside the breast improves the power efficiency of the link and the ability to detect the presence of a tumor.

6.5.2 Maximum Allowed Transmitted Power by the Antennas

Average Specific Absorption Rate (ASAR) describes the electromagnetic energy that is absorbed in biological tissues and is a critical parameter for assessing the tissue-safety of wireless communications in bio applications. The peak 1-g ASAR spatial distribution versus frequency is simulated in HFSS for all four positions of the antennas inside the array for the monopole and spiral antennas, with and without use of a reflector. The ANSI limitations specify a maximum peak 1-g ASAR of 1.6 W/kg [80].

Based on the maximum simulated ASAR of tissues in HFSS, the maximum allowed transmitted power from each position of the antennas in the array is calculated. The results are presented in Table 6.2. Sending more power can damage the biological tissues. The HFSS results show that most radiated power is absorbed by the skin which is in contact with the antenna arrays. From Table 6.2, the maximum averaged transmitted power for the monopole and the spiral antenna array are around 4 mW and 3.1 mW, respectively. We observe that the reflector does not significantly change this power, and neither does changing the antenna position.

Table 6.2: Maximum averaged transmitted power for monopole and spiral antennas in various array positions.

Antenna	Monopole(mW)	Monopole with reflector (mW)	Spiral(mW)	Spiral with reflector (mW)
Ant. 1	4.1	4	3.2	3.1
Ant. 2	4.1	4.1	3.2	3.1
Ant. 3	4.0	4.0	3.2	3.1
Ant. 4	3.9	4	3.1	3.1

6.6 Conclusion

We presented a methodology for designing wearable single- and dual-polarization antennas on a flexible substrate for breast cancer detection operating over 2-4 GHz frequency bands. The new array improves on previous microwave radar imaging systems in that it is highly flexible, cost-effective to fabricate, and light-weight. Simulations were carried out with HFSS, exploiting a layered (inhomogeneous) model with different dielectric constants and loss tangents to capture the effect of surrounding tissues. To verify the validity of our model and the antenna design procedure, the fabricated arrays were measured on a phantom that is representative of actual biological tissues.

Measurements confirmed that the proposed antenna achieved our design goals, validating our antenna design methodology and our biological tissue modeling. Finally, it has been shown that by using a reflector for the arrays, penetration of the propagated EM waves can be improved significantly. For both arrays we determined the maximum power allowed to be transmitted from the wearable antenna, by taking into account the limitation imposed by the ANSI. For our future work, we will investigate the performance of our wearable arrays (single and dual polarizations) on patients, and determine which antenna is the most practical for our application. We will then integrate the wearable arrays into a bra-like prototype for improved microwave breast imaging.

Chapter 7

Conclusions and Future Work

The major subject of this thesis was to design a power efficient ultra wideband high speed wireless link for implant-to-air data communications. We investigated step by step of designing the wireless link from system level design to circuit level design. We have covered biological tissues modeling in EM software, designing different types of implantable and wearable antennas for human head and breast, a new system level design of an implantable transceiver, and circuit level design of the new transceiver architecture.

In chapter 2, we utilized a realistic model of the biological channel to inform the design of antennas for the implanted transmitter and the external receiver to determine the maximum allowable power to 1) respect ANSI guidelines for avoiding tissue damage and 2) respect FCC guidelines on unlicensed transmissions. Antennas placement is examined under two scenarios having contrasting power constraints. Performance of the system within the biological tissues is examined via simulation and experiment.

In chapter 3, we focused on designing single and dual-polarization antennas on rigid or flexible substrate for wireless ultra-wideband brain machine interface. We investigated both flexible and rigid materials and examined performance trade-offs. The proposed antennas were designed to operate in a frequency range of 2–11 GHz covering both the 2.45 GHz (ISM) band and the 3.1–10.6 GHz UWB band. Several advantages were confirmed for dual polarization antennas: 1) smaller size, 2) lower sensitivity to angular misalignment, and 3) higher fidelity.

In chapter 4, we proposed a new wireless transceiver architecture for implanted systems that simultaneously stimulate neurons and record neural responses. This architecture supports large numbers of electrodes (> 500), providing 100 Mb/s for the downlink of stimulation signals, and Gbps for the uplink neural recordings. The proposed transceiver architecture is a shared ultra-wideband antenna which support both ISM band (down-link) and UWB band(up-link).

In chapter 5,we presented a circuit level design of the proposed transceiver which was presented

in chapter 4. Proper isolation ($>$ 20 dB) between the TX and RX path is implemented 1) by shaping the transmitted pulses to fall within the unregulated UWB spectrum (3.1-7 GHz), and 2) by space-efficient filtering (avoiding a circulator or diplexer) of the downlink OOK spectrum in the RX low-noise amplifier. The UWB 3.1-7 GHz transmitter can use either OOK or binary phase shift keying (BPSK) modulation schemes. The proposed FDT provides dual band 500 Mbps TX uplink data rate and 100 Mbps RX downlink data rate, and it is fully integrated into standard TSMC 0.18 um CMOS within a total size of 0.8 mm^2. The total measured power consumption is 10.4 mW in full duplex mode (5 mW at 100 Mbps for RX, and 5.4 mW at 500 Mbps or 10.8 pJ/bit for TX).

Finally in chapter 6, we designed single and dual-polarization antennas for wireless ultra-wideband breast cancer detection systems using an inhomogeneous multi-layer model of the human breast. The proposed antennas are designed to operate in a frequency range of 2–4 GHz. Furthermore, two flexible conformal 4×4 ultra-wideband antenna arrays (single and dual polarization) were developed for a radar-based breast cancer detection system. By using a reflector for the arrays, the penetration of the propagated EM waves from the antennas into the breast can be improved.

Several possible research projects could exploit material presented in this thesis. The presented methodology of designing a wireless data communication link in the presence of biological tissues can be applied for other sections of the body or low power miniaturized wearable wireless sensors. A big effort is still needed to work on an external transceiver to communicate in real-time with the implanted transceiver. The data rate of the designed interface system in this thesis can be increased by using equalization, or potentially using antenna arrays with multiple-input and multiple-output (MIMO) technique and faster technology like 65nm TSMC. Also, on chip antennas can be used. Dissipated power is the most important issue because it increases the temperature of the cortex. For this reason, power consumption of the designed circuit needs to be further reduced.

Publication List

Journal

J1. H. Bahrami, S.A. Mirbozorgi, L.A. Rusch, and B. Gosselin, “Biological Channel Modeling and Implantable UWB Antenna Design for Neural Recording Systems,” IEEE Transactions on Biomedical Engineering, vol.62, no.1, pp.88-98, Jan. 2015.

J2. H. Bahrami, S.A. Mirbozorgi, R. Ameli, L.A. Rusch, and B. Gosselin, “Flexible UWB Antennas with Polarization-Diverse Implantable for Neural Recording Systems,” IEEE Transactions on Biomedical Circuits and Systems, (Accepted, 2015).

J3. H. Bahrami, S.A. Mirbozorgi, T.A. Nguyen, B. Gosselin, and L.A. Rusch, “System Level Design of High-Speed Full-Duplex Transceiver for Neural Recording and Stimulating Systems,” IEEE Transactions on Microwave Theory and Techniques, (Under review, 2015).

J4. S.A. Mirbozorgi, H. Bahrami, M. Sawan, L.A. Rusch, and B. Gosselin, “Fully Integrated Circulator-less Full Duplex Transceiver Circuit Design for Bio-Implant Applications,” IEEE Transactions on Biomedical Circuits and Systems (Under review, 2015).

J5. H. Bahrami, E. Porter, A. Santorelli, B. Gosselin, M. Popovic, and L.A. Rusch, “Flexible Sixteen Antenna Array for Microwave Breast Cancer Detection ,” IEEE Transactions on Biomedical Engineering, (Under review, 2014).

Conference

C1. H. Bahrami, B. Gosselin, and L.A. Rusch, "Design of a miniaturized UWB antenna optimized for implantable neural recording systems," New Circuits and Systems Conference (NEWCAS), IEEE 10th International, 2012.

C2. H. Bahrami, B. Gosselin, and L.A. Rusch, "Realistic modeling of the biological channel for the design of implantable wireless UWB communication systems," Engineering in Medicine and Biology Society (EMBC), Annual International Conference of the IEEE, 2012.

C3. S.A. Mirbozorgi, H. Bahrami, L.A. Rusch, and B. Gosselin, “A Low-Power 2.4-GHz Receiver for Wireless Implantable Neural Stimulators,” IEEE International Symposium on Circuits and Systems, ISCAS, Melbourne, Australia, June 2014.

C4. H. Bahrami, S.A. Mirbozorgi, L.A. Rusch, and B. Gosselin, “BER Performance of Implant-to-Air High-Speed UWB Data Communications for Neural Recording Systems,” 36th annual Conf. of EMBC, Chicago, USA, August 2014.

C5. M.E. Khaled, H. Bahrami, P. Fortier, B. Gosselin, and L.A. Rusch, "Capacity of UWB wireless channel for neural recording systems," Engineering in Medicine and Biology Society (EMBC), 36th Annual International Conference of the IEEE, 2014.

C6. H. Bahrami, E. Porter, A. Santorelli, B. Gosselin, M. Popovic, and L.A. Rusch, "Flexible sixteen monopole antenna array for microwave breast cancer detection," Engineering in Medicine and Biology Society (EMBC), 36th Annual International Conference of the IEEE, 2014.

Book Chapter

1. H. Bahrami, L.A. Rusch and B. Gosselin, Biological channel modeling and implantable UWB antenna design; Handbook of Bioelectronics, Cambridge University Press, (In progress, 2015).

Bibliography

[1] S. Gabriel and C. Gabriel. The dielectric properties of biological tissues: Iii. parametric models for the dielectric spectrum of tissues. *Physics in Medicine and Biology*, vol.41, no.11, pp.22-71, 1996.

[2] D. Zhou and E. Greenbaum. *Implantable Neural Prostheses 2: Techniques and Engineering Approaches*. Biological and Medical Physics, Biomedical Engineering. Springer, 2010.

[3] M. Chae, Z. Yang, M.R. Yuce, H. Linh, and W. Liu. A 128-channel 6 mw wireless neural recording ic with spike feature extraction and uwb transmitter. *Neural Systems and Rehabilitation Engineering, IEEE Transactions on*, vol.17, no.4, pp.312-321, 2009.

[4] K.Y. Yazdandoost. A 2.4 ghz antenna for medical implanted communications. pp.1775-1778, 2009.

[5] T.F. Chien, H.C. Yang, C.M. Cheng, and C.H. Luo. Develop cpw-fed monopole broadband implantable antennas on the high dielectric constant ceramic substrates. *Microwave and Optical Technology Letters*, vol.52, no.9, pp.2136-2139, 2010.

[6] J. Kim and Y. Rahmat-Samii. Implanted antennas inside a human body: simulations, designs, and characterizations. *Microwave Theory and Techniques, IEEE Transactions on*, vol.52, no.8, pp.1934-1943, 2004.

[7] C.A. Balanis. *Advanced Engineering Electromagnetics*. Course Smart Series. Wiley, 2012.

[8] P. Ghanbari and M. Hajj. Finite element analysis of tissue electropermeability through the application of electric pulses. *J Bioengineer and Biomedical Sci*, vol.3, pp.2318-2326, 2013.

[9] D. Valderas. *Ultrawideband Antennas: Design and Applications*. Imperial College Press, 2011.

[10] U.M. Jow and M. Ghovanloo. Optimization of data coils in a multiband wireless link for neuroprosthetic implantable devices. *Biomedical Circuits and Systems, IEEE Transactions on*, vol.4, no.5, pp.301-310, 2010.

[11] B. Sklar. *Digital communications: fundamentals and applications.* Prentice Hall Communications Engineering and Emerging Technologies Series. Prentice-Hall PTR, 2001.

[12] M. Ojaroudi, C. Ghobadi, and J. Nourinia. Small square monopole antenna with inverted t-shaped notch in the ground plane for uwb application. *Antennas and Wireless Propagation Letters, IEEE*, vol.8, pp.728-731, 2009.

[13] Reza Zaker and A. Abdipour. A very compact ultrawideband printed omnidirectional monopole antenna. *Antennas and Wireless Propagation Letters, IEEE*, vol.9, pp.471-473, 2010.

[14] H. Zamani and P. Mohseni. A high-speed circuit architecture for ir-uwb transmission of fast-scan cyclic voltammetry in 0.35 um cmos. pp.1561-1564, 2010.

[15] M. Mark, T. Bjorninen, Y.D. Chen, S. Venkatraman, L. Ukkonen, L. Sydanheimo, J.M. Carmena, and J.M. Rabaey. Wireless channel characterization for mm-size neural implants. *Engineering in Medicine and Biology Society (EMBC), 2010 Annual International Conference of the IEEE*, pp.1565-1568, 2010.

[16] E. Pancera and W. Wiesbeck. Fidelity based optimization of uwb antenna-radiation for medical applications. *Antennas and Propagation (APSURSI), 2011 IEEE International Symposium on*, pp.2411-2414, 2011.

[17] M. Leib, M. Frei, D. Sailer, and W. Menzel. Design and characterization of a uwb slot antenna optimized for radiation in human tissue. *Ultra-Wideband, 2009. ICUWB 2009. IEEE International Conference on*, pp.159-163, 2009.

[18] T. Dissanayake, M.R. Yuce, and Chee Ho. Design and evaluation of a compact antenna for implant-to-air uwb communication. *Antennas and Wireless Propagation Letters, IEEE*, vol.8, pp.153-156, 2009.

[19] Qiong Wang, K. Wolf, and D. Plettemeier. An uwb capsule endoscope antenna design for biomedical communications. pp.1-6, 2010.

[20] J.C. Wang, E.G. Lim, Z. Wang, Y. Huang, T. Tillo, M. Zhang, and R. Alrawashdeh. Uwb planar antennas for wireless capsule endoscopy. pp.340-343, 2013.

[21] A. Drossos, V. Santomaa, and N. Kuster. The dependence of electromagnetic energy absorption upon human head tissue composition in the frequency range of 300-3000 mhz. *Microwave Theory and Techniques, IEEE Transactions on*, vol.48, no.11, pp.1988-1995, 2000.

[22] C.A. Balanis. *ANTENNA THEORY: ANALYSIS AND DESIGN, 2ND ED.* Wiley India Pvt. Limited, 2007.

[23] Y.S. Chen, S.Y. Chen, and H.J. Li. Analysis of antenna coupling in near-field communication systems. *Antennas and Propagation, IEEE Transactions on*, vol.58, no.10, pp.3327-3335, 2010.

[24] F. Merli, B. Fuchs, J.R. Mosig, and A.K. Skrivervik. The effect of insulating layers on the performance of implanted antennas. *Antennas and Propagation, IEEE Transactions on*, vol.59, no.1, pp.21-31, 2011.

[25] H. Bahrami, B. Gosselin, and L.A. Rusch. Design of a miniaturized uwb antenna optimized for implantable neural recording systems. pp.309-312, 2012.

[26] H. Bahrami, B. Gosselin, and L.A. Rusch. Realistic modeling of the biological channel for the design of implantable wireless uwb communication systems. pp.6015-6018, 2012.

[27] G. Chaudhary, Yongchae Jeong, and Jongsik Lim. Microstrip line negative group delay filters for microwave circuits. *Microwave Theory and Techniques, IEEE Transactions on*, vol.62, no.2, pp.234-243, 2014.

[28] A.R. Eskandari, L. Mohammady, and B. Eliasi. A novel method for analyzing and predicting of group delay variations in wideband transmission lines. pp.298-301, 2007.

[29] Ian Oppermann. The role of uwb in 4g. *Wirel. Pers. Commun.*, vol.29, no.2, pp.121-133, 2004.

[30] Ieee standard for safety levels with respect to human exposure to radio frequency electromagnetic fields, 3 khz to 300 ghz. *IEEE Std C95.1-2005 (Revision of IEEE Std C95.1-1991)*, pp.230-238, 2006.

[31] A. Peyman, C. Gabriel, E.H. Grant, G. Vermeeren, and L. Martens. Variation of the dielectric properties of tissues with age: the effect on the values of sar in children when exposed to walkie–talkie devices. *Physics in Medicine and Biology*, vol.55, no.17, pp.5240-5249, 2010.

[32] A. Peyman, S.J. Holden, S. Watts, R. Perrott, and C. Gabriel. Dielectric properties of porcine cerebrospinal tissues at microwave frequencies: in vivo , in vitro and systematic variation with age. *Physics in Medicine and Biology*, vol.52, no.8, pp.22-29, 2007.

[33] M.A. Stuchly, A. Kraszewski, S.S. Stuchly, and A.M. Smith. Dielectric properties of animal tissues in vivo at radio and microwave frequencies: comparison between species. *Physics in Medicine and Biology*, vol.27, no.7, pp.920-927, 1982.

[34] A. Peyman, A.A. Rezazadeh, and C. Gabriel. Changes in the dielectric properties of rat tissue as a function of age at microwave frequencies. *Physics in Medicine and Biology*, vol.46, no.6, pp.16-17, 2001.

[35] C. Gabriel and A. Peyman. Dielectric measurement: error analysis and assessment of uncertainty. *Physics in Medicine and Biology*, vol.51, no.23, pp.6025-6033, 2006.

[36] M.R. Yuce and T. Dissanayake. Easy-to-swallow wireless telemetry. *Microwave Magazine, IEEE*, vol.13, no.6, pp.90-101, 2012.

[37] M.R. Yuce, T. Dissanayake, and H.C. Keong. Wireless telemetry for electronic pill technology. pp.1433-1438, 2009.

[38] Y. Chen, J. Teo, J.C.Y. Lai, E. Gunawan, K.S. Low, C.B. Soh, and P.B. Rapajic. Cooperative communications in ultra-wideband wireless body area networks: Channel modeling and system diversity analysis. *Selected Areas in Communications, IEEE Journal on*, vol.27, no.1, pp.5-16, 2009.

[39] Jingjing Shi and Jianqing Wang. Channel characterization and diversity feasibility for in-body to on-body communication using low-band uwb signals. pp.1-4, 2010.

[40] K. Sayrafian-Pour, Wen-Bin Yang, J. Hagedorn, J. Terrill, and K.Y. Yazdandoost. A statistical path loss model for medical implant communication channels. pp.2995-2999, 2009.

[41] A. Khaleghi, R. Cha´vez-Santiago, and I. Balasingham. Ultra-wideband statistical propagation channel model for implant sensors in the human chest. *Microwaves, Antennas Propagation, IET*, vol.5, no.15, pp.1805-1812, 2011.

[42] R. Chavez-Santiago, K. Sayrafian-Pour, A. Khaleghi, K. Takizawa, J. Wang, I. Balasingham, and H.B. Li. Propagation models for ieee 802.15.6 standardization of implant communication in body area networks. *Communications Magazine, IEEE*, vol.51, no.8, pp.80-87, 2004.

[43] D. Anzai, K. Katsu, R. Chavez-Santiago, Q. Wang, D. Plettemeier, J. Wang, and I. Balasingham. Experimental evaluation of implant uwb-ir transmission with living animal for body area networks. *Microwave Theory and Techniques, IEEE Transactions on*, vol.62, no.1, pp.183-192, 2014.

[44] R. Chavez-Santiago, I. Balasingham, J. Bergsland, W. Zahid, K. Takizawa, R. Miura, and H.B. Li. Experimental implant communication of high data rate video using an ultra wideband radio link. pp.5175-5178, 2013.

[45] H. Bahrami, S.A. Mirbozorgi, L.A. Rusch, and B. Gosselin. Ber performance of implant-to-air high-speed uwb data communications for neural recording systems. vol.29, no.2, pp.3961-3964, 2014.

[46] M. El Khaled, H. Bahrami, P. Fortier, B. Gosselin, and L.A. Rusch. Capacity of uwb wireless channel for neural recording systems. pp.3965-3968, 2014.

[47] M.L. Scarpello, D. Kurup, H. Rogier, D. Vande Ginste, F. Axisa, J. Vanfleteren, W. Joseph, L. Martens, and G. Vermeeren. Design of an implantable slot dipole conformal flexible antenna for biomedical applications. *Antennas and Propagation, IEEE Transactions on*, vol.59, no.10, pp.3556-3564, 2011.

[48] R. Alrawashdeh, Y. Huang, and P. Cao. Flexible meandered loop antenna for implants in medradio and ism bands. *Electronics Letters*, vol.49, no.24, pp.1515-1517, 2013.

[49] Z. Wang, L. Zhang, D. Psychoudakis, and J.L. Volakis. Flexible textile antennas for body-worn communication. pp.205-208, 2012.

[50] C. Kim, J. K. Kim, K.T. Kim, and Y.K. Yoon. Micromachined wearable/foldable super wideband (swa) monopole antenna based on a flexible liquid crystal polymer (lcp) substrate toward imaging/sensing/health monitoring systems. pp.1926-1932, 2013.

[51] H. Bahrami, S.A. Mirbozorgi, L.A. Rusch, and B. Gosselin. Biological channel modeling and implantable uwb antenna design for neural recording systems. *Biomedical Engineering, IEEE Transactions on*, vol.62, no.1, pp.88-98, 2015.

[52] H.K. Yoon, J.A. Park A, Y.J. Yoon, and C.H. Lee. A cpw-fed polarization diversity antenna for uwb systems. pp.1-4, 2008.

[53] H.K. Yoon, Y.J. Yoon, H. Kim, and C.H. Lee. Flexible ultra-wideband polarisation diversity antenna with band-notch function. *Microwaves, Antennas Propagation, IET*, vol.5, no.12, pp.1463-1470, 2011.

[54] L. Vallozzi, P. Van Torre, C. Hertleer, H. Rogier, M. Moeneclaey, and J. Verhaevert. Wireless communication for firefighters using dual-polarized textile antennas integrated in their garment. *Antennas and Propagation, IEEE Transactions on*, vol.58, no.4, pp.1357-1368, 2010.

[55] H.R. Khaleel, H.M. Al-Rizzo, and D.G. Rucker. Compact polyimide-based antennas for flexible displays. *Display Technology, Journal of*, vol.8, no.2, pp.91-97, 2012.

[56] H.R. Khaleel, H.M. Al-Rizzo, D.G. Rucker, and S. Mohan. A compact polyimide-based uwb antenna for flexible electronics. *Antennas and Wireless Propagation Letters, IEEE*, vol.11, pp.564-567, 2012.

[57] W. El Hajj, C. Person, and J. Wiart. A miniaturized rectangular-spiral bi-band coplanar antenna for off-body communications. pp.3262-3265, 2013.

[58] S.H. Lee, J. Lee, J.Y. Young, S. Park, C. Cheon, K. Kim, and S. Nam. A wideband spiral antenna for ingestible capsule endoscope systems: Experimental results in a human phantom and a pig. *Biomedical Engineering, IEEE Transactions on*, vol.58, no.6, pp.1734-1741, 2011.

[59] T.S.P. See and Z.N. Chen. Experimental characterization of uwb antennas for on-body communications. *Antennas and Propagation, IEEE Transactions on*, vol.57, no.4, pp.866-874, 2009.

[60] K. Rambabu, A.E.C. Tan, K.K.M. Chan, and M.Y.W. Chia. Estimation of antenna effect on ultra-wideband pulse shape in transmission and reception. *Electromagnetic Compatibility, IEEE Transactions on*, vol.51, no.3, pp.604-610, 2009.

[61] A.H. Mohammadian, A. Rajkotia, and S.S. Soliman. Characterization of uwb transmit-receive antenna system. pp.157-161, 2003.

[62] G. Simard, M. Sawan, and D. Massicotte. Novel coils topology intended for biomedical implants with multiple carrier inductive link. pp.537-540, 2009.

[63] G. Simard, M. Sawan, and D. Massicotte. High-speed oqpsk and efficient power transfer through inductive link for biomedical implants. *Biomedical Circuits and Systems, IEEE Transactions on*, vol.4, no.3, pp.192-200, 2010.

[64] S.A. Mirbozorgi, H. Bahrami, L.A. Rusch, and B. Gosselin. A low-power 2.4-ghz receiver for wireless implantable neural stimulators. pp.1082-1085, 2014.

[65] B. Gosselin, A.E. Ayoub, J.F. Roy, M. Sawan, F. Lepore, A. Chaudhuri, and D. Guitton. A mixed-signal multichip neural recording interface with bandwidth reduction. *Biomedical Circuits and Systems, IEEE Transactions on*, vol.3, no.3, pp.129-141, 2009.

[66] Y. Gao, Y. Zheng, S. Diao, W.D. Toh, C.W. Ang, M. Je, and C.H. Heng. Low-power ultrawideband wireless telemetry transceiver for medical sensor applications. *Biomedical Engineering, IEEE Transactions on*, vol.58, no.3, pp.768-772, 2011.

[67] H. Miranda and T.H. Meng. A programmable pulse uwb transmitter with 34multichannel neuro-recording systems. pp.1-4, 2010.

[68] S.C. Shin, J.Y. Huang, K.Y. Lin, and H. Wang. A 1.5-9.6 ghz monolithic active quasi-circulator in 0.18 um cmos technology. *Microwave and Wireless Components Letters, IEEE*, vol.18, no.12, pp.797-799, 2008.

[69] Z. El-Khatib, L. MacEachern, and S.A. Mahmoud. A fully-integrated linearized cmos bidirectional distributed amplifier as uwb active circulator. pp.106-109, 2008.

[70] S. He, N. Akel, and C.E. Saavedra. Active quasi-circulator with high port-to-port isolation and small area. *Electronics Letters*, vol.48, no.14, pp.848-850, 2012.

[71] H. Morkner, M. Karakucuk, G. Carr, and S. Espino. A full duplex front end module for wifi 802.11.n applications. pp.162-165, 2008.

[72] T.Y. Yun, C. Wang, P. Zepeda, C.T. Rodenbeck, M.R. Coutant, M. Li, and K. Chang. A 10- to 21-ghz, low-cost, multifrequency, and full-duplex phased-array antenna system. *Antennas and Propagation, IEEE Transactions on*, vol.50, no.5, pp.641-650, 2002.

[73] K. Oh, S. Sankaran, H.T. Wu, J.J. Lin, M. Hwang, and K.O. Kenneth. Full-duplex crystalless cmos transceiver with an on-chip antenna for wireless communication in a hybrid engine controller board. *Solid-State Circuits, IEEE Journal of*, vol.48, no.6, pp.1327-1342, 2013.

[74] X. Zhang, M. Elgamel, and M.A. Bayoumi. Gaussian pulse approximation using standard cmos and its application for sub-ghz uwb impulse radio. *International Journal of Circuit Theory and Applications*, vol.38, no.4, pp.383-407, 2010.

[75] D.D. Wentzloff and A.P. Chandrakasan. Gaussian pulse generators for subbanded ultra-wideband transmitters. *Microwave Theory and Techniques, IEEE Transactions on*, vol.54, no.4, pp.1647-1655, 2006.

[76] M. Demirkan and R.R. Spencer. A pulse-based ultra-wideband transmitter in 90-nm cmos for wpans. *Solid-State Circuits, IEEE Journal of*, vol.43, no.12, pp.2820-2828, 2008.

[77] Y. Zhu, J.D. Zuegel, J.R. Marciante, and H. Wu. Distributed waveform generator: A new circuit technique for ultra-wideband pulse generation, shaping and modulation. *Solid-State Circuits, IEEE Journal of*, vol.44, no.3, pp.808-823, 2009.

[78] L. Zhou, Z. Chen, C.C. Wang, F. Tzeng, V. Jain, and P. Heydari. A 2-gb/s 130-nm cmos rf-correlation-based ir-uwb transceiver front-end. *Microwave Theory and Techniques, IEEE Transactions on*, vol.59, no.4, pp.1117-1130, 2011.

[79] H. Kim and Y. Joo. Fifth-derivative gaussian pulse generator for uwb system. pp.671-674, 2005.

[80] Ieee standard for safety levels with respect to human exposure to radio frequency electromagnetic fields, 3 khz to 300 ghz. *IEEE Standard for Safety Levels with Respect to Human Exposure to Radio Frequency Electromagnetic Fields, 3 kHz to 300 GHz.*

[81] R.R. Harrison, R.J. Kier, C.A. Chestek, V. Gilja, P. Nuyujukian, S. Ryu, B. Greger, F. Solzbacher, and K.V. Shenoy. Wireless neural recording with single low-power integrated circuit. *Neural Systems and Rehabilitation Engineering, IEEE Transactions on*, vol.17, no.4, pp.322-329, 2009.

[82] A. Berenyi, Z. Somogyvari, A.J. Nagy, L. Roux, J.D. Long, S. Fujisawa, E. Stark, A. Leonardo, T.D. Harris, and G. Buzsaki. Large-scale, high-density (up to 512 channels) recording of local circuits in behaving animals. *Journal of Neurophysiology*, pp.1522-1598, 2013.

[83] K. Chen, Z. Yang, L. Hoang, J. Weiland, M. Humayun, and W. Liu. An integrated 256-channel epiretinal prosthesis. *Solid-State Circuits, IEEE Journal of*, vol.45, no.9, pp.1946-1956, 2010.

[84] A.G. Rouse, S.R. Stanslaski, P. Cong, R.M. Jensen, P. Afshar, D. Ullestad, R. Gupta, G.F. Molnar, D.W. Moran, and T.J. Denison. A chronic generalized bi-directional brain–machine interface. *Journal of Neural Engineering*, vol.8, no.3, pp.3556-3564, 2011, 2011.

[85] M. Ghovanloo and K. Najafi. A wireless implantable multichannel microstimulating system-on-a-chip with modular architecture. *Neural Systems and Rehabilitation Engineering, IEEE Transactions on*, vol.15, no.3, pp.449-457, 2007.

[86] D. Daoud, M. Ghorbel, A. Ben Hamida, and J. Tomas. A wireless data and power recovery for biomedical microsystems implants. pp.1-5, 2011.

[87] N.P. Cook, L. Sieber, and H. Widmer. High efficiency and power transfer in wireless power magnetic resonators. 2010.

[88] M. Kiani, U.M. Jow, and M. Ghovanloo. Design and optimization of a 3-coil inductive link for efficient wireless power transmission. *Biomedical Circuits and Systems, IEEE Transactions on*, vol.5, no.6, pp.579-591, 2011.

[89] A.K. RamRakhyani and G. Lazzi. On the design of efficient multi-coil telemetry system for biomedical implants. *Biomedical Circuits and Systems, IEEE Transactions on*, vol.7, no.1, pp.11-23, 2013.

[90] G. Yilmaz, O. Atasoy, and C. Dehollain. Wireless energy and data transfer for in-vivo epileptic focus localization. *Sensors Journal, IEEE*, vol.13, no.11, pp.4172-4179, 2013.

[91] F. Yazicioglu, C.M. Lopez, S. Mitra, B. Raducanu, S. Musa, and F. Kloosterman. Ultra-high-density in-vivo neural probes. pp.2032-2035, 2014.

[92] A. Berenyi, Z. Somogyvari, A.J. Nagy, L. Roux, J.D. Long, S. Fujisawa, E. Stark, A. Leonardo, T.D. Harris, and G. Buzsaki. Large-scale, high-density (up to 512 channels)

recording of local circuits in behaving animals. *Journal of Neurophysiology*, pp.1522-1598, 2013.

[93] T. Wada, R. Nakajima, H. Obiya, T. Ogami, M. Koshino, M. Kawashima, and N. Nakajima. A miniaturized broadband lumped element circulator for reconfigurable front-end system. pp.1-3, 2014.

[94] O. Novak, W. Wu, and C. Charles. Wireless ultra-wide-band data link for biomedical implants. pp.352-355, 2009.

[95] M. Chae, W. Liu, Z. Yang, T. Chen, J. Kim, M. Sivaprakasam, and M. Yuce. A 128-channel 6mw wireless neural recording ic with on-the-fly spike sorting and uwb tansmitter. pp.146-603, 2008.

[96] W. Wu, O. Novak, C.T. Charles, and X. Fan. A low-power 3.1-5ghz ultra-wideband low noise amplifier utilizing miller effect. pp.255-259, 2009.

[97] M.T. Reiha and J.R. Long. A 1.2 v reactive-feedback 3.1 ndash;10.6 ghz low-noise amplifier in 0.13 um cmos. *Solid-State Circuits, IEEE Journal of*, vol.42, no.5, pp.1023-1033, 2007.

[98] H.H. Hsieh, J.H. Wang, and L.H. Lu. Gain-enhancement techniques for cmos folded cascode lnas at low-voltage operations. *Microwave Theory and Techniques, IEEE Transactions on*, vol.56, no.8, pp.1807-1816, 2008.

[99] D.A. Guimaraes. *Digital Transmission: A Simulation-Aided Introduction with VisSim/Comm*. Signals and Communication Technology. Springer Berlin Heidelberg, 2010.

[100] M. Yin, D.A. Borton, J. Aceros, W.R. Patterson, and A.V. Nurmikko. A 100-channel hermetically sealed implantable device for chronic wireless neurosensing applications. *Biomedical Circuits and Systems, IEEE Transactions on*, vol.7, no.2, pp.115-128, 2013.

[101] E.C. Fear, S.C. Hagness, P.M. Meaney, M. Okoniewski, and M.A. Stuchly. Enhancing breast tumor detection with near-field imaging. *Microwave Magazine, IEEE*, vol.3, no.1, pp.48-56, 2002.

[102] S.K. Davis, B.D. Van Veen, S.C. Hagness, and F. Kelcz. Breast tumor characterization based on ultrawideband microwave backscatter. *Biomedical Engineering, IEEE Transactions on*, vol.55, no.1, pp.237-246, 2008.

[103] S.P. Poplack, T.D. Tosteson, W.A. Wells, B.W. Pogue, P.M. Meaney, A. Hartov, C.A. Kogel, S.K. Soho, J.J. Gibson, and K.D. Paulsen. Electromagnetic breast imaging: Results of a pilot study in women with abnormal mammograms. *Radiology*, vol.243, no.2, pp.350-359, 2007.

[104] D. Gibbins, M. Klemm, I.J. Craddock, J.A. Leendertz, A. Preece, and R. Benjamin. A comparison of a wide-slot and a stacked patch antenna for the purpose of breast cancer detection. *Antennas and Propagation, IEEE Transactions on*, vol.58, no.3, pp.665-674, 2010.

[105] M. Klemm, J.A. Leendertz, D. Gibbins, I.J. Craddock, A. Preece, and R. Benjamin. Microwave radar-based differential breast cancer imaging: Imaging in homogeneous breast phantoms and low contrast scenarios. *Antennas and Propagation, IEEE Transactions on*, vol.58, no.7, pp.2337-2344, 2010.

[106] T. Sugitani, S. Kubota, A. Toya, X. Xiao, and T. Kikkawa. A compact 4×4 planar uwb antenna array for 3-d breast cancer detection. *Antennas and Wireless Propagation Letters, IEEE*, vol.12, pp.733-736, 2013.

[107] A.M.A. Shaheen and K.M. Quboa. Modeling and optimizing ultra wideband antennas for microwave breast cancer detection. pp.1-6, 2012.

[108] X. Li, S.C. Hagness, M.K. Choi, and D.W. Van Der Weide. Numerical and experimental investigation of an ultrawideband ridged pyramidal horn antenna with curved launching plane for pulse radiation. *Antennas and Wireless Propagation Letters, IEEE*, vol.2, no.1, pp.259-262, 2003.

[109] Y. Wang, A.E. Fathy, and M.R. Mahfouz. Novel compact tapered microstrip slot antenna for microwave breast imaging. pp.2119-2122, 2011.

[110] L. Wang and B. Huang. Design of ultra-wideband mimo antenna for breast tumor detection. pp.2119-2122, 2012.

[111] A. Eesuola, Y. Chen, and G.Y. Tian. Novel ultra-wideband directional antennas for microwave breast cancer detection. pp.90-93, 2011.

[112] G. Chavka and M. Garbaruk. Design of planar monopole pulse antenna for ultra-wideband radiocommunication systems. pp.129-132, 2007.

[113] S. Latif, D. Flores-Tapia, S. Pistorius, and L. Shafai. A planar ultrawideband elliptical monopole antenna with reflector for breast microwave imaging. *Microwave and Optical Technology Letters*, vol.56, no.4, pp.808-813, 2014.

[114] E. Porter, E. Kirshin, A. Santorelli, M. Coates, and M. Popovic. Time-domain multistatic radar system for microwave breast screening. *Antennas and Wireless Propagation Letters, IEEE*, vol.12, pp.229-232, 2013.